Mixed quantum-classical dynamics of energy transport in open quantum systems

by

Pablo Carpio Martinez

A thesis submitted in partial fulfillment of the requirements for the degree of

Doctor of Philosophy

Department of Chemistry

University of Alberta

Abstract

The study of energy transport through molecules has gathered much attention in recent years due to its crucial role in the operation of a host of nano-devices. Understanding the details of such processes can aid in the development of novel molecular electronics and nanophononic devices. Over the years, various approaches have been used to simulate energy transport dynamics in both simple and complex models in order to gain insight into how system and environmental properties affect the transport rates/mechanisms. In the present thesis, we studied (i) nonequilibrium heat transport and (ii) vibrational energy transfer in a variety of model molecular systems using mixed quantum-classical dynamics. For direction (i), we assessed the ability of a recently developed mixed quantum-classical dynamics method, known as Deterministic Evolution of Coordinates with Initial Decoupled Equations (DECIDE), for calculating steady-state heat currents in the nonequilibrium spin-boson (NESB) model – a model molecular junction consisting of a two-level system coupled to two harmonic oscillator baths at different temperatures. Furthermore, we investigated the importance of quantizing the initial thermal bath distributions in calculating the time-dependent heats and heat currents across a wide range of bath parameter regimes, viz., temperatures, temperature gaps, reorganization energies, and cutoff frequencies. Our results show that DECIDE performs quite well and captures the expected trends in the steady-state heat current. In addition, our findings underscore the importance of performing quantum sampling of the bath coordinates across a wide range of bath parameter regimes. For direction (ii), using adiabatic mixed quantum-classical dynamics, we studied the influence of lattice vibrations on the transfer of vibrational excitation energy in a modified Su-Schrieffer-Heeger (SSH) dimer chain model. We found that the incorporation of lattice vibrations greatly enhances the rate of long-range population transfer compared to the static chain. Finally, we investigated the effects of coupling the end sites of the SSH chain to thermal baths at different temperatures on the vibrational excitation energy transfer. Regardless of the temperature gap, we found that the long-range population transfer is enhanced in the static chain compared to the chain without the baths. However, in the case of the non-static chain, the presence of the temperature baths does not significantly alter the transfer, pointing to the robustness of the process. Together, these studies shed light on the microscopic mechanisms of quantum energy transport in molecular junctions and polymer chains, how to control the rates/mechanisms of the energy transport, and the validity of using mixed quantum-classical dynamics for simulating quantum energy transport. Ultimately, our methodology and findings may guide the experimental design of novel nanophononic devices.

Preface

Chapter 3 of this thesis is based on the following published article: Carpio-Martinez, P., & Hanna, G. Nonequilibrium heat transport in a molecular junction: A mixed quantum-classical approach. *J. Chem. Phys.* 151(7), 074112 (2019). My contributions to this work included: helping in the development, debugging, and testing of the code, running all simulations, collecting and analyzing data, preparing the first draft of the manuscript, and refining it until published, under the guidance of Prof. Hanna. Dr. Junjie Liu and Prof. Hanna contributed to the development of the theory and were responsible for the initial development of the code.

Chapter 4 of this thesis is based on the following published article: Carpio-Martinez, P., & Hanna, G. Quantum bath effects on nonequilibrium heat transport in model molecular junctions. *J. Chem. Phys.* 154, 094108 (2021). My contributions to this work included: modifying, debugging, and testing of the code, running all simulations, collecting and analyzing data, preparing the first draft of the manuscript, and refining it until published, under the guidance of Prof. Hanna.

Chapter 5 of this thesis is based on the following published article: Hsieh, C. Y., Carpio-Martinez, P., & Hanna, G. Achieving ultrafast topologically-protected vibrational energy transfer in a dimer chain. *Chem. Phys.* 515, 315-322 (2018). My contributions to this work included: modifying, debugging, and testing of the code, running simulations, collecting and analyzing data, revising the manuscript, and refining it until published, under the guidance of Prof. Hanna. Dr. Chang-Yu Hsieh and Prof. Hanna were responsible for the original idea and contributed to the development of the theory and first version of the code.

The contents of Chapter 6 will likely form a part of a future publication. My contributions to this work included: modifying the Hamiltonian of the system, modifying, debugging, and testing of the code, running simulations, and collecting and analyzing data. Prof. Hanna was responsible for the original idea and contributed to the development of the theory.

To my beloved parents,

Concepción J. Martínez Vázquez and Rogelio S. Carpio García.

Acknowledgements

I would like to express my sincere gratitude to my supervisor Prof. Gabriel Hanna for all his support, judicious guidance, and patience throughout my Ph.D. studies. I would also like to thank the members of my examination committee: Prof. Roman Krems, Prof. Arthur Mar, Prof. Lingzi Sang and Prof. Wolfgang Jäger for taking the time to read my thesis and providing invaluable comments. I am also grateful to CONACyT for providing financial support over the last three years of my PhD studies (scholarship no. 709746). Finally, I wish to thank my amazing parents, Yeyo and Mamá Conchita, for all their support throughout these years and for fighting this battle with me in spite of the distance. You made this dream possible and I am deeply indebted to you.

Contents

List of Figures

List of Symbols

$T_{L/R}$	temperature of the left/right bath
$\hat{H}_W$	Weyl-ordered and partially Wigner-transformed Hamiltonian
Δ	tunnelling frequency
$\hat{\sigma}_{x/z}$	Pauli matrices
$R_{j,v}$	mass-weighted position of the jth harmonic oscillator in the vth bath
$P_{j,v}$	mass-weighted momentum of the jth harmonic oscillator in the vth bath
$\omega_{j,v}$	frequency of the jth harmonic oscillator in the vth bath
$C_{j,v}$	spin-bath coupling coefficient jth harmonic oscillator in the vth bath
N_v	number of oscillators in the vth bath
$I_v(\omega)$	spectral density of the vth bath
$\omega_{c,v}$	cutoff frequency of the vth bath
$\omega_{m,v}$	maximum frequency of the vth bath
ξ_v	Kondo parameter
E_r	reorganization energy of the vth bath
$\|0\rangle$	ground state of the SSH chain
$\|\phi_m\rangle$	m^{th} singly excited state of the SSH chain
$\|\chi_{m0}\rangle$	ground state of the m^{th} oscillator in the SSH chain
$\|\chi_{m1}\rangle$	first excited state of the m^{th} oscillator in the SSH chain
H_0	ground state matrix element in the SSH Hamiltonian
H_s	singly-excited state matrix element in the SSH Hamiltonian
$\mathbf{J}$	tridiagonal symmetric coupling matrix
J and J'	strength of the transition dipole moment coupling between neighbouring oscillators
E_{m1}	ground state energy of the m^{th} oscillator in the SSH chain
E_{m0}	first excited state energy of the m^{th} oscillator in the SSH chain
N	number of sites in the SSH chain
H	J'/J ratio
$\|e^{\pm}\rangle$	boundary modes of the SSH chain

$\hat{\rho}(t)$	time-dependent density matrix of a composite system
$\hat{H}$	Hamiltonian of a composite system
$\hat{H}_s$	Hamiltonian of a quantum subsystem
$\hat{H}_b$	Hamiltonian of a bath
$\hat{V}_c$	potential energy operator (which includes coupling between quantum and classical subsystems)
$\hat{H}_B^v$	Hamiltonian of the vth heat bath
X	set of positions and momenta of the bath DOF
$E_\alpha(R)$	energy of adiabatic state α
$\omega_{\alpha\alpha'}$	transition frequency between adiabatic states α and α'
L	classical Liouville operator
F_W^α	Hellmann-Feynman force
$\mathcal{J}_{\alpha\alpha',\beta\beta'}$	nonadiabatic transition matrix element
$d_{\alpha\beta}$	nonadiabatic coupling matrix element
$\hat{A}_W$	partial Wigner transform of an operator $\hat{A}$
$\langle A(t)\rangle$	time-dependent expectation value of an observable $\hat{A}$
$\langle Q_v(t)\rangle$	time-dependent heat transferred from the vth heat bath to the subsystem
$\langle J_v(t)\rangle$	time-dependent heat current of the vth bath
J	steady-state heat current
$\rho_{B,W}^v(0)$	partially Wigner-transformed canonical distribution of the vth bath
$\hat{\boldsymbol{x}}$	generalized set of subsystem coordinates
$\rho_{B,cl}^v(0)$	classical Boltzmann distribution
$g(X)$	quantum dispersion function
$P_t(Q(t))$	probability distribution of the net heat transfer $Q(t)$ from the hot bath to the cold bath at time t
W	force constant of classical oscillator in the SSH chain
χ	coupling strength between classical acoustic phonons and high-frequency oscillators in SSH chain

Abbreviations

BR	Bloch-Redfield
BTE	Boltzmann transport equation
DFT	density functional theory
DECIDE	deterministic evolution of coordinates with initial decoupled equations
DOF	degrees of freedom
FODEs	first-order differential equations
HQME	hierarchical quantum master equation
LRPT	long-range population transfer
MD	molecular dynamics
MFT	mean-field theory
ML-MCTDH	multilayer multiconfiguration time-dependent Hartree
MOF	metal-organic framework
NEGF	nonequilibrium Green's function
NESB	nonequilibrium spin-boson
NIBA	noninteracting blip approximation
PES	potential energy surface
QCLE	quantum-classical Liouville equation
QUAPI	quasi-adiabatic propagator path integral
SSFT	steady-state fluctuation theorem
SSH	Su-Schrieffer-Heeger

Chapter 1

Introduction

1.1 Energy transport in open quantum systems

Energy transfer plays a fundamental role in many chemical and biological processes in natural and synthetic systems. Over the last several decades, many studies have been dedicated to a molecular-level understanding of the rates and mechanisms of such processes [1–4]. Many of these studies have been motivated by the need to develop artificial systems that mimic the energy transfer efficiencies observed in natural biological systems. For example, in the Fenna-Matthews-Olson complex (found in green sulfur bacteria), the excitation energy from solar photons is channelled to the photosynthetic reaction center with a near-unity efficiency [5]. Thus, gaining a detailed understanding of nature's light-harvesting mechanisms can aid in the design of materials/devices with unprecedented efficiencies.

Molecular junctions − single molecules whose ends are bound to metal or semiconductor leads − are architectures of particular interest due to their enhanced transport properties that surpass their bulk (generally silicon-based) counterparts [6, 7]. For example, when a junction molecule is placed in contact with leads at different temperatures, its multiple degrees of freedom could channel heat in a way that is not attainable by bulk junctions. [8].

Numerous studies of nanoscale heat transfer have been performed, triggered mainly by the growing demand for reducing thermal resistances (or increasing thermal conductivities) in today's increasingly small electronic devices [9, 10]. Because the thermal properties of materials/devices change in going from the micrometer to the nanometer scale, understanding the rates and mechanisms of heat transport at the molecular level is of key importance. At this scale, vibrational energy transport is involved and a host of phenomena have been observed, including ballistic and hopping transport, phonon transport and interference, rectification and localization, among others [11]. In particular, graphene sheets, carbon chain-based single-molecule junctions, and polymer chains have been shown to possess interesting thermal transport properties [12–14]. For example, when polymer chains are aligned in their crystalline form, structural factors (i.e., presence of random orientation, entanglement, weak intermolecular interactions) that impede the heat transfer are minimized, resulting in higher thermal conductivities in the chains (up to 50 $\mathrm{Wm^{-1}K^{-1}}$) in contrast with the low thermal conductivities (0.1-1 $\mathrm{Wm^{-1}K^{-1}}$) of bulk amorphous polymers[15]. In molecular junctions composed of saturated hydrocarbons, excited phonon modes exchange energy with molecular vibrations in the leads, allowing for thermal energy to be carried away [16, 17]. These and a few other applications are depicted in Fig. 1.1.

From a theoretical standpoint, the study of nanoscale energy/heat transport is a very challenging task as one has to model the dynamics of open quantum systems. For example, one can think of a molecular junction as an open quantum system in which the junction molecule (i.e., quantum system) interacts with the electrodes/baths (i.e., environments) to which they are attached. Fully quantum mechanical treatments of open quantum systems are computationally very demanding, or even intractable, due to the many degrees of freedom present in the system and environment(s). Thus, over the years, a number of

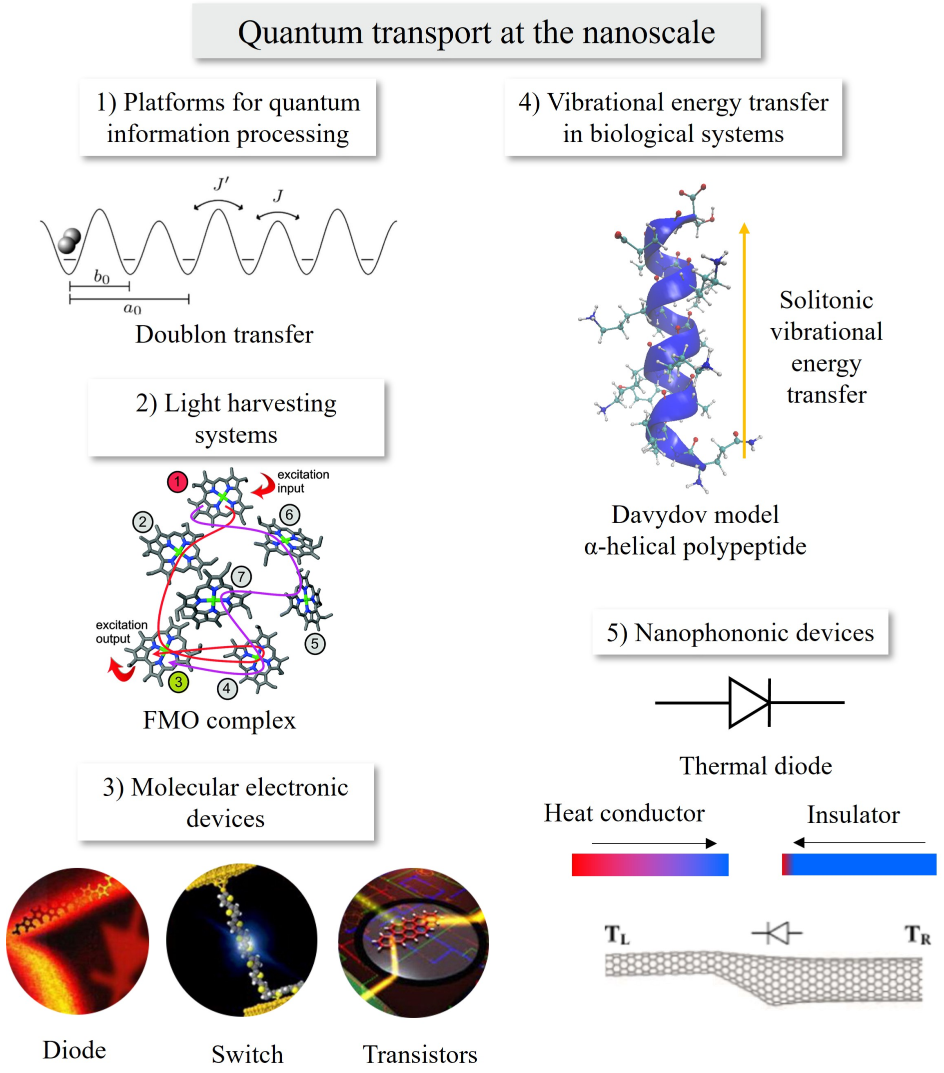

Figure 1.1: Applications of quantum transport at the nanoscale: 1) doublon transfer in polymeric chains [18], 2) bio-inspired light-harvesting systems [19], 3) molecular electronics [7], 4) energy transfer in biological systems [20], and 5) nanophononics [21].

approximate methods have been developed and applied to the study of nanoscale heat transfer, several of which we will briefly describe in the next subsection.

1.2 Overview of theoretical methods for simulating energy transport

In general, the modelling of nanoscale energy transport processes is challenging because it requires computational methods that are capable of describing both the electronic structure and nonequilibrium dynamics of molecules in condensed phase environments and, in some cases, strong electron-electron and/or electron-phonon coupling [6]. This subsection will briefly describe several of the commonly used theoretical approaches for simulating energy transport at the nanoscale.

Classical molecular dynamics (MD) has been extensively used for calculating thermal properties of nanoscale systems. In classical MD, the Newtonian equations of motion for all the particles in a system are solved numerically subject to a given force field. It has been used, for example, to calculate steady-state heat flux between two nanoparticles [22] and in silicon/germanium nanostructures [23], and to calculate thermal conductivity in DNA/water mixtures [24] and quasi-one-dimensional silicon nanowires [25]. Classical MD simulations have facilitated the study of structural effects on thermal transport. For example, it has been demonstrated that the presence of holes/defects in graphene significantly reduce its thermal conductivity [26]; similarly, doping silicene lattices with silicon isotopes largely reduces the conduction of heat across a sheet [27]. Other structural effects that have been considered include strain [28, 29], dislocation [30, 31], and folding [32]. Within classical MD, there are two commonly used approaches to calculate thermal transport properties, viz., equilibrium MD and nonequilibrium MD. In equilibrium MD, the thermal conductivity can be calculated from the heat current auto-correlation function according to the following Green-Kubo relation

$$\kappa_{\alpha\beta} = \frac{1}{k_B T^2 V} \int_0^{\infty} \langle J_\alpha(0) J_\beta(t) \rangle \, dt, \tag{1.1}$$

where k_B is the Boltzmann constant, T is the temperature of the system, V is the volume of the system, and J_α is the heat current in the α direction [25]. In nonequilibrium MD, the thermal conductivity of a finite-sized system is calculated according to Fourier's law

$$\kappa = -\frac{J}{\nabla T}, \tag{1.2}$$

where J is the heat flux and ∇T is the temperature gradient along the transport direction in the nonequilibrium steady state. This method requires a temperature gradient along the transport direction which can be obtained in two different ways. In the first way, one imposes a local temperature by using thermostats, whereas in the second way, one imposes a heat flux by simultaneously extracting/adding kinetic energy from/to a heat bath [33].

Ab initio methods have been proposed based on approximate solutions of the Boltzmann transport equation (BTE). This equation governs the transport and scattering of energy carriers in solids and is widely used to simulate mesoscopic conduction processes. Particularly, when the heat carriers are phonons the BTE takes the form

$$\frac{\partial n}{\partial t} + \mathbf{v} \cdot \nabla n = \left(\frac{\partial n}{\partial t}\right)_s \tag{1.3}$$

where $n = n(\mathbf{x}, \mathbf{p}, t)$ denotes the phonon distribution function describing the fraction of phonons that have position $\mathbf{x}$ and momentum $\mathbf{p}$ at time t, $\mathbf{v}$ is the group velocity or travelling speed of the phonons, and $\left(\frac{\partial n}{\partial t}\right)_s$ is the scattering rate of the relevant scattering processes. For phonons in non-metallic solids, the dominating scattering processes are phonon-phonon scattering, phonon-impurity scattering, and phonon-boundary scattering [34]. To solve the BTE, the group velocity and scattering rates are entered as parameters and they involve the use of interatomic force constants from density functional theory (DFT) calculations. Once the distribution function is obtained by solving the BTE, the temperature distribution and heat flux can then be extracted. Although the computational cost of the ab initio BTE method is very high, the results obtained are quite accurate when compared to the experimental data.

The nonequilibrium Green's function (NEGF) approach is another powerful tool to study phonon transport in nanostructures. In the NEGF method, one models lattice vibrations as waves and takes atomic details into account. A typical simulation system consists of three regions: a device (scattering) region and two contacts (thermal reservoirs). The temperatures of the two contacts are kept at $T + \Delta T/2$ and $T - \Delta T/2$, where ΔT is a small temperature difference. Then, the number of phonons passing the device region from one contact to the other is obtained. Next, that information is used to calculate the heat flux across the device region according to the well-known Landauer formalism [35]. The NEGF is an ideal approach to study heat transport in the ballistic regime in systems where elastic scatterings are dominant. In addition, this method can predict thermal boundary resistance between heterogeneous materials with full consideration of the interfacial atomic structures [36].

There are also methods which treat the device as an open quantum system (i.e., system-bath setup). Along these lines, several numerically exact approaches have been used to calculate energy transport properties. In the hierarchical quantum master equation (HQME) approach, the influence of the environment on the reduced density matrix is described in terms of a hierarchical set of equations [37, 38]. This method allows one to treat strong system-bath couplings, quantum coherence, and quantum entanglement, and it has been applied to model the dynamics of a quantum heat-engine and quantum ratchet, where the system is strongly coupled to two heat baths at different temperatures [39]. The multilayer multiconfiguration time-dependent Hartree (ML-MCTDH) method has been used to study nonequilibrium heat transport in molecular junctions [40, 41]. ML-MCTDH is a variational basis-set method, which relies on a multiconfiguration expansion of the wave function in terms of time-dependent basis functions and a hierarchical multilayer representation [6]. The equations of motion for the time-dependent coefficients and basis functions are obtained from the variational principle of the time-dependent Schrödinger equation. This method converges to the exact solution by using a sufficiently large basis set. Since ML-MCTDH is a wave-function based method, it treats the device and baths as a closed quantum system. Another numerically exact methodology is the quasi-adiabatic propagator path integral (QUAPI) approach, which propagates the reduced density matrix and was originally used to simulate the spin dynamics of the spin-boson model [42, 43]. This method has also been used to model heat transfer dynamics in the nonequilibrium spin-boson (NESB) model and allows one to treat strong system-bath couplings and to include non-Markovian effects [44]. Several approximate approaches have also been used. The Bloch-Redfield equation [45], which is obtained from the Nakajima-Zwanzig quantum master equation [46, 47] after applying perturbation theory and the Markovian approximation, has been used to study dissipative dynamics and heat transfer in the NESB model; its regime of validity is restricted to very weak system-bath couplings [44]. Another approach is the noninteracting blip approximation (NIBA), which is based on the path integral influence functional formalism, has been used to simulate thermal conductances in model molecular junctions in the high temperature limit [48]. Monte Carlo has also proven to be useful in the numerical implementation of path integral-based methods [49, 50] and has been successfully applied to the calculation of thermal conductances in a model molecular junction [48].

Various mixed-quantum classical methods have been applied to the study of quantum transport in open quantum systems [51–58]. These methods stem from the quantum-classical Liouville equation, which provides an exact description of a quantum subsystem that is bilinearly coupled to a harmonic environment. Several of these methods will be explained in detail in the following chapter.

1.3 Nonequilibrium spin-boson model

Chapters 3 and 4 of this thesis will focus on the study of heat transport in the nonequilibrium spin-boson (NESB) model. This model is widely used to study quantum heat transport in molecular junctions due to its generality and simplicity [44]. The NESB model consists of a two-level spin (with states $|+\rangle$ and $|-\rangle$) coupled to two harmonic oscillator baths at temperatures T_L and T_R (see Fig. 1.2 for a pictorial representation of the model). In preparation for a mixed quantum-classical treatment of this model, its Weyl-ordered and partially Wigner-transformed [59] (with respect to the bath coordinates) Hamiltonian reads

$$\hat{H}_W = \frac{\Delta}{2}\hat{\sigma}_x + \frac{1}{2}\sum_{v=L,R}\sum_{j=1}^{N_v}\left(P_{j,v}^2 + \omega_{j,v}^2 R_{j,v}^2 + C_{j,v}R_{j,v}\hat{\sigma}_z + C_{j,v}\hat{\sigma}_z R_{j,v}\right), \tag{1.4}$$

where Δ is the tunnelling frequency between the states $|+\rangle$ and $|-\rangle$ (N.B.: The spin-boson model results from an orthogonal transformation of a double-well system, with a barrier Δ between the $|+\rangle$ and $|-\rangle$, to a two-state system. A detailed description of this transformation may be found in Ref. [60].), $\hat{\sigma}_{x/z}$ are the Pauli matrices, $R_{j,v}$ and $P_{j,v}$ are the mass-weighted position and momentum, respectively, of the jth harmonic oscillator in the vth bath, $C_{j,v}$ is the spin-bath coupling coefficient, and N_v is the number of oscillators in the vth bath. In the partial Wigner representation, the spin and bath degrees of freedom are represented in Hilbert space and phase space, respectively.

In this thesis, the bilinear coupling between the spin and baths is characterized by an Ohmic spectral density $I_v(\omega) = \frac{\xi_v}{2}\pi\omega e^{-\omega/\omega_{c,v}}$, where ξ_v is a dimensionless parameter that governs the coupling strength between the spin and the vth bath and $\omega_{c,v}$ is the cutoff frequency of the vth bath. The reorganization energy of the vth Ohmic bath is given by

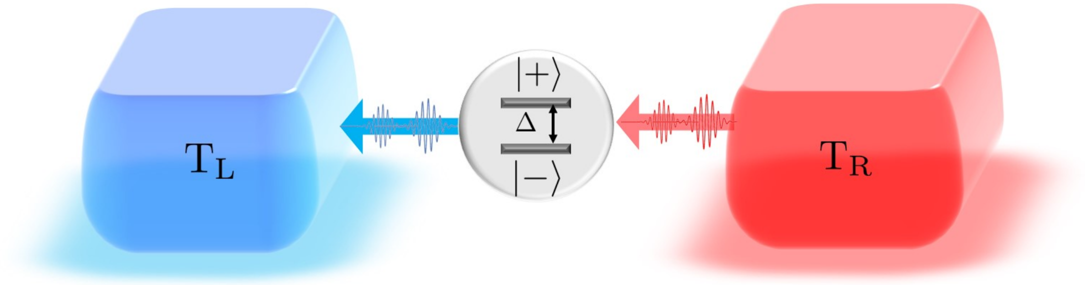

Figure 1.2: Pictorial representation of the NESB model. The two-level spin subsystem is coupled to two thermal baths at different temperatures ($T_L < T_R$). Because of the nonequilibrium condition, heat flows from right to left bath through the two-level spin subsystem.

$E_{r,v} = \xi_v \omega_{c,v}/2$. Since $I_v(\omega)$ is a continuous function, it may be implemented numerically using the following discretization scheme [61, 62]

$$C_{j,v} = \sqrt{\xi_v \hbar \omega_{0,v}} \omega_{j,v}, \quad \omega_{j,v} = -\omega_{c,v} \ln \left(1 - j \frac{\omega_{0,v}}{\omega_{c,v}}\right), \tag{1.5}$$

where $\omega_{0,v} = \omega_{c,v}(1 - e^{-\omega_{m,v}/\omega_{c,v}})/N_v$, $\omega_{m,v}$ is the maximum frequency of the vth bath, and j runs from 1 to N_v. In the present thesis, we focus on the symmetric case where $\omega_{m,L} = \omega_{m,R} = \omega_m$, $\omega_{c,L} = \omega_{c,R} = \omega_c$, and $\xi_L = \xi_R = \xi$ (or $E_{r,L} = E_{r,R} = E_r$).

The NESB model has been used widely in different applications. For example, the NESB model has been used to describe phononic energy transfer in anharmonic molecular junctions [21, 63], nontrivial spin Seebeck effects for thermal-driven spin devices [64], exciton transfer in photosynthetic complexes [65], electromagnetic transport through superconducting circuits [66], and nonequilibrium phase transitions in many body physics[65].

1.4 Su-Schrieffer-Heeger model

In Chapters 5 and 6, we study vibrational exciton transfer dynamics in a modified version of the Su-Schrieffer-Heeger model – a tight-binding model for noninteracting, spinless electrons confined in a dimer chain [67] which has been extensively used to study the topological properties of polyacetelene [68]. Here, we introduce the *static* version of the model in which the chain sites (viz., high-frequency vibrational modes) are fixed in space with respect to each other. Later, in Chapter 5, we present the *non-static* version of the model, in which the chain sites are allowed to oscillate with respect to each other (by coupling them to acoustic phonons). Finally, in Chapter 6, we present a version in which the end sites of the chain are coupled to thermal baths at different temperatures.

The Hamiltonian of the static dimerized chain containing N high-frequency quantum oscillators, is given by

$$\begin{aligned} H_q &= H_0|0\rangle\langle 0| + \sum_{m,n=1}^{N} H^0_{mn}|\phi_m\rangle\langle\phi_n| \\ &\equiv H_0|0\rangle\langle 0| + H_s, \end{aligned} \tag{1.6}$$

where $|\phi_m\rangle = |\chi_{m1}\rangle \prod_{n\neq m}|\chi_{n0}\rangle$ is the m^{th} singly excited state and $|0\rangle = \prod_m |\chi_{m0}\rangle$ is the ground state of the chain. (N.B.: $|\chi_{m0}\rangle$ and $|\chi_{m1}\rangle$ denote the ground and first excited states, respectively, of the m^{th} oscillator.) The ground state matrix element, H_0, is a constant for the static chain, but will take on a particular functional form once the couplings to the acoustic phonons are introduced (see Chapter 5). The matrix elements of the Hamiltonian for the singly-excited manifold, H_s, are given by

$$\begin{aligned} H^0_{mn} &= \delta_{m,n}\left[H_0 + E_{m1} - E_{m0}\right] \\ &\quad - J_{mn}\left[\delta_{m-1,n}\langle\phi_m|q_m q_{m-1}|\phi_{m-1}\rangle + \delta_{m,n-1}\langle\phi_n|q_n q_{n-1}|\phi_{n-1}\rangle\right], \end{aligned} \tag{1.7}$$

where the coupling matrix $\mathbf{J}$ is a tridiagonal symmetric matrix with the super-diagonal given by alternating parameters J and J',

$$J_{n-1,n} = \begin{cases} J & \text{if } n \text{ is even} \\ J' & \text{if } n \text{ is odd.} \end{cases} \tag{1.8}$$

The diagonal matrix elements of $\mathbf{J}$ are taken to be zeros as they are not used. In the above, J and J' are the parameters that govern the strength of the transition dipole moment coupling between neighbouring oscillators, $E_{m1} - E_{m0}$ is the energy gap between the ground and first excited states of the m^{th} oscillator, and q_m is the position of the m^{th} oscillator. As in previous studies of a similar model[69, 70], the diagonal matrix elements H^0_{nn} are assumed to be identical across the chain. Because of the alternating nearest neighbour coupling strengths, J and J', the chain structure is considered dimerized (with J and J' being the intra-dimer and inter-dimer coupling parameters, respectively). Since the Hamiltonian H_s is restricted to the single-excitation manifold, it is identical to a single-particle dimerized Hückel chain[71, 72] for electrons, sometimes referred to as the Su-Schrieffer-Heeger (SSH) model[73] by the condensed matter physics community (see Fig. 1.3 for a schematic representation).

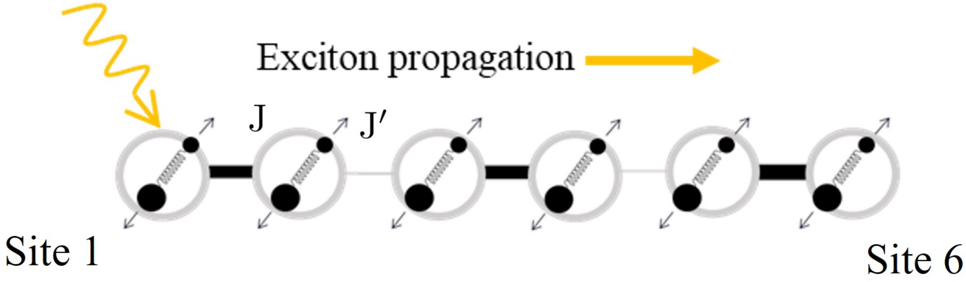

Figure 1.3: Schematic representation of the excitation energy transfer in the dimerized SSH chain (with $N = 6$) when in its topologically nontrivial phase (i.e., $J' \gg J$). After a photo-excitation of the first site in the chain, the exciton propagates across the chain.

The spectral properties[71–74] of this dimerized quantum chain model are well-established. The model features two bands of energy levels separated by a band gap. In fact, the energy spectrum can be classified according to three different conditions: (1) N is odd, (2) N is even with $J'/J = H < H_c$, and (3) N is even with $J'/J = H > H_c$, where $H_c = (1 - 1/(N+1))^{-1/2}$. One can identify which topological class a particular model belongs to by analyzing the eigenstates of the Hamiltonian closest to the zero energy reference point, which lies exactly in the middle of the band gap. When N is odd (i.e., the chain cannot be fully dimerized), there exists a unique zero-energy state, which is predominantly localized on either the left or the right edge site of the chain and decays exponentially into the bulk of the chain (i.e., all sites except for the two boundary sites). This highly localized quantum state looks rather classical and cannot support long-range population transfer. When N is even and $H < H_c$, the pair of eigenstates closest to the zero energy reference point are delocalized across the entire chain and, therefore, cannot be considered as edge states. Under these conditions, the chain is in its so-called topologically trivial phase. However, as H is varied to the point that $H \geq H_c$, these two eigenstates exhibit completely different spatial profiles. The structure of the wave functions goes from being highly delocalized to bimodal with peaks localized on both ends of the chain, i.e., the two "edge states" become $|e^{\pm}\rangle \approx \frac{1}{\sqrt{2}}(|1\rangle \pm |N\rangle)$. As H is further increased, these edge states become more localized. Under these conditions, the chain is in its so-called topologically non-trivial phase. In the topologically non-trivial phase, the two edge states are energetically well separated from the other states by the band gap and are the only states that are predominately peaked at the two boundary sites. The decoupling of the two states from the remainder of the Hilbert space becomes more pronounced as H increases or the chain length increases. In such a situation, the population transfer via the topologically protected edge states can be explained in terms of the quantum dynamics of an effective two-level model consisting of the $|e^{\pm}\rangle \approx \frac{1}{\sqrt{2}}(|1\rangle \pm |N\rangle)$ boundary modes. In the basis $\{|1\rangle, |N\rangle\}$, the Hamiltonian matrix for this model is

$$H_{2L} = \begin{bmatrix} 0 & \Delta \\ \Delta & 0 \end{bmatrix}, \tag{1.9}$$

where the tunneling parameter is given by $\Delta \approx JH^{1-N/2}$. This effective Hamiltonian can be derived from time-independent perturbation theory by first partitioning H_s into an unperturbed Hamiltonian containing only the inter-dimer transition dipole moments proportional to J' and a perturbing Hamiltonian containing only the intra-dimer transition dipole moments proportional to J, i.e., $H^{[0]} = H_s(J = 0)$ and $H^{[1]} = H_s(J' = 0)$, respectively. Then, one expands the pair of exact zero-energy eigenfunctions $|e^{\pm}\rangle$ for H_s in terms of the unperturbed eigenfunctions $\frac{1}{\sqrt{2}}(|1\rangle \pm |N\rangle)$ for $H^{[0]}$, including up to second-order corrections. Finally, calculating the matrix elements $\langle e^{\pm}| H_s |e^{\pm}\rangle$, rotating the matrix back to the site basis, and retaining only matrix elements corresponding to the two ends, yields the effective Hamiltonian H_{2L}. From the expression for Δ, we see that as the chain length increases the two edge states converge into a doubly degenerate zero-energy manifold. Therefore, for long-range population transfer problems, Δ will typically be an extremely small number given the facts that $H \gg 1$ in the topologically non-trivial phase and N is a large number. If the chain is excited at one end at time $t = 0$ with $|\psi(0)\rangle = |1\rangle \approx \frac{1}{\sqrt{2}}(|e^{+}\rangle + |e^{-}\rangle)$, then the wavepacket propagates as follows: $|\psi(t)\rangle \approx \cos(\omega t/2)|1\rangle - i\sin(\omega t/2)|N\rangle$ with $\omega = (E^{+} - E^{-})/2 = 2\Delta$. From this straightforward analysis, one learns two things: (1) the population is largely confined and oscillates between the two end sites $|1\rangle$ and $|N\rangle$, and (2) the oscillation frequency of $\omega \ll 1$ implies an extremely slow long-range population transfer.

In addition to describing quantum transport dynamics in polyacetylene, the SSH chain has been used to model vibrational exciton transport in α-helical polypetides [57], topological plasmon polaritons in dimerized doped silicon nanoparticle chains [75], topological optical waveguides in silicon arrays [76], and multilayer graphene systems [77].

1.5 Objectives and outline of thesis

The main objectives of the present thesis are

- to test the validity of using mixed quantum-classical dynamics for simulating nonequilibrium heat transport in model molecular junctions.
- to assess the importance of quantum sampling of the initial bath coordinates in mixed quantum-classical / classical dynamics simulations of quantum heat transport.
- to evaluate the influence of intramolecular vibrations on vibrational exciton transfer in dimerized chain molecules.
- to gauge the influence of thermal gradients on topologically protected vibrational exciton transfer in dimerized chain molecules.

Below is an outline of the topics covered in each chapter:

1. In Chapter 2, we introduce the quantum-classical Liouville equation (QCLE) and discuss two approximate solutions of the equation, namely the adiabatic and DECIDE solutions, which can be used to simulate the mixed quantum-classical dynamics of a system.
2. In Chapter 3, we study to what extent the DECIDE method is capable of capturing the turnovers observed in the steady-state heat current as a function of both the tunnelling frequency and bath reorganization energy in the NESB model. A discussion of the role of nonadiabatic effects in the calculation of heat currents is also presented.

3. In Chapter 4, we study the effects of sampling the initial bath degrees of freedom from quantum and classical probability distributions on the time-dependent heats and steady-state heat currents in the NESB model. We discussion the differences between both treatments and assess the importance of quantizing the initial thermal bath distributions.

4. In Chapter 5, we investigate long-range population transfer in the SSH model. We contrast the long-range population transfer is the static-chain version of the model with that in the non-static version, where the chain is coupled to a set of acoustic phonons. We then analyze to what extent the robustness of the long-range population is compromised by varying the parameters in the model.

5. In Chapter 6, we study the effects of coupling the ends of the static and non-static SSH chains to thermal baths at different temperatures. We analyze how the long-range population transfer is affected by a thermal gradient.

6. In Chapter 7, we present our concluding remarks and future plans.

Chapter 2

Mixed Quantum-Classical Dynamics

In many situations, one is interested in studying a quantum transport process occurring in a complex system containing a large number of degrees of freedom (DOF). For such systems, a full quantum mechanical treatment of the dynamics is computationally very expensive or sometimes even impossible. One practical way to circumvent this limitation is to use mixed quantum-classical dynamics methodologies, in which the subsystem of interest is treated quantum mechanically while its environment (referred to as a *bath* in what follows) is treated in a classical-like way. Such methodologies may be derived from the quantum-classical Liouville equation, which we will discuss in the following section [78, 79].

2.1 Quantum-classical Liouville equation

The fully quantum dynamics of a composite system, comprising a subsystem and bath, is prescribed by the quantum Liouville equation

$$i\hbar\frac{\partial\hat{\rho}(t)}{\partial t} = -\left[\hat{H}, \hat{\rho}(t)\right], \tag{2.1}$$

where $\hat{\rho}(t)$ is the time-dependent density matrix of the composite system and $\hat{H}$ is the Hamiltonian of the composite system, given by

$$\hat{H} = \hat{H}_s + \hat{H}_b + \hat{V}_c, \tag{2.2}$$

where $\hat{H}_s$ and $\hat{H}_b$ are the Hamiltonians of the subsystem and bath, respectively, and $\hat{V}_c$ the potential energy operator corresponding to the coupling between them.

The quantum-classical Liouville equation (QCLE) may be derived from the quantum Liouville equation in the limit that the subsystem DOF are much lighter than the bath DOF. Here, I will outline the main steps of the derivation (for the full derivation, please see Ref. [80]). One starts by performing a partial Wigner transform [81] over the bath DOF of the quantum Liouville equation, which for the density matrix is given by

$$\hat{\rho}_W(R,P) = \frac{1}{(2\pi\hbar)^N}\int dZ e^{iP\cdot Z/\hbar}\left\langle R - \frac{Z}{2}\left|\hat{\rho}\right| R + \frac{Z}{2}\right\rangle, \tag{2.3}$$

and for an operator $\hat{A}$

$$\hat{A}_W(R,P) = \int dZ e^{iP\cdot Z/\hbar}\left\langle R - \frac{Z}{2}\left|\hat{A}\right| R + \frac{Z}{2}\right\rangle. \tag{2.4}$$

In the above equations, R and P represent the positions and momenta of the N bath DOF, and the integrations are carried out over the variables Z. After the transform, the quantum Liouville equation takes the form

$$\frac{\partial}{\partial t}\hat{\rho}_W(X,t) = -\frac{i}{\hbar}\left(\hat{H}_W e^{\hbar\Lambda/2i}\hat{\rho}_W(t) - \hat{\rho}_W(t)e^{\hbar\Lambda/2i}\hat{H}_W\right) \tag{2.5}$$

where $X = (R, P)$ denotes the set of positions and momenta of the bath DOF and $\Lambda = \overleftarrow{\nabla}_P \cdot \overrightarrow{\nabla}_R - \overleftarrow{\nabla}_R \cdot \overrightarrow{\nabla}_P$ (here, the arrows indicate the directions in which the derivatives act). To arrive at this equation, the following relation for the Wigner transform of a product of two operators was used [82], viz.,

$$(\hat{A}\hat{B})_W(X) = \hat{A}_W(X)e^{\hbar\Lambda/2i}\hat{B}_W(X). \tag{2.6}$$

Expanding the exponential operators in Eq. 2.5 and truncating the result at $\mathcal{O}(\hbar)$, one obtains the QCLE, which reads

$$\begin{aligned}\frac{\partial}{\partial t}\hat{\rho}_W(X,t) \quad &= \quad \frac{i}{\hbar}\left[\hat{H}_W\left(X\right), \hat{\rho}_W\left(X,t\right)\right] \\ &\quad -\frac{1}{2}\left(\left\{\hat{H}_W\left(X\right), \hat{\rho}_W\left(X,t\right)\right\} - \left\{\hat{\rho}_W\left(X,t\right), \hat{H}_W\left(X\right)\right\}\right),\end{aligned} \tag{2.7}$$

where the square and curly brackets denote a commutator and Poisson bracket, respectively. The partially Wigner-transformed Hamiltonian, $\hat{H}_W$, is given by

$$\hat{H}_W\left(X\right) = \hat{K}_q + \hat{V}_q + K_b(P) + V_b(R) + \hat{V}_c(R), \tag{2.8}$$

where $\hat{K}_q$ and $\hat{V}_q$ are the kinetic and potential energy operators of the subsystem, respectively; K_b and V_b are the kinetic and potential energies of the bath, respectively; and $\hat{V}_c$ is the subsystem-bath coupling potential energy operator. As illustrated in Ref. [83], the truncation of the series expansion after first order in $\hbar$ is justified for systems in which the masses of the subsystem DOF are much smaller compared to those of the bath DOF.

2.2 Adiabatic dynamics

In the present thesis, we used adiabatic mixed quantum-classical dynamics to model heat and vibrational energy transfer in the NESB and SSH models, respectively. Adiabatic dynamics neglects nonadiabatic effects, which may be pronounced or non-negligible in many cases. Nevertheless, adiabatic dynamics is simple and efficient and can sometimes be used to gain qualitative and possibly even quantitative insight into a process. We now show how adiabatic dynamics can be derived from the QCLE.

We start by writing down the QCLE in the Heisenberg picture for an observable $\hat{A}_W(X,t)$ (although one could equivalently start from the QLCE in the Schrödinger picture for the density matrix),

$$\begin{aligned} \frac{\partial}{\partial t}\hat{A}_W(X,t) &= \frac{i}{\hbar}\left[\hat{H}_W\left(X\right), \hat{A}_W\left(X,t\right)\right] \\ &-\frac{1}{2}\left(\left\{\hat{H}_W\left(X\right), \hat{A}_W\left(X,t\right)\right\} - \left\{\hat{A}_W\left(X,t\right), \hat{H}_W\left(X\right)\right\}\right). \end{aligned} \tag{2.9}$$

We then represent the QCLE in the so-called adiabatic basis of eigenstates $\{|\alpha;R\rangle\}$ defined by the eigenvalue problem $\hat{H}_W|\alpha;R\rangle = E_\alpha(R)|\alpha;R\rangle$, with $E_\alpha(R)$ the energy of state α. This leads to the following equation[83]

$$\frac{\partial}{\partial t}A_W^{\alpha\alpha'}(X,t) = \sum_{\beta\beta'}\left[(i\omega_{\alpha\alpha'} + iL_{\alpha\alpha'})\delta_{\alpha\beta}\delta_{\alpha'\beta'} - \mathcal{J}_{\alpha\alpha',\beta\beta'}\right]A_W^{\beta\beta'}(X,t), \tag{2.10}$$

where $\omega_{\alpha\alpha'} = (E_\alpha - E_{\alpha'})/\hbar$ is the transition frequency between states α and α'; L is the classical Liouville operator given by

$$iL_{\alpha\alpha'} = \frac{P}{M} \cdot \frac{\partial}{\partial R} + \frac{1}{2}\left(F_W^{\alpha} + F_W^{\alpha'}\right) \cdot \frac{\partial}{\partial P}, \tag{2.11}$$

with the Hellmann-Feynman forces $F_W^{\alpha} = -\langle \alpha; R|\nabla_R \hat{V}_c(R)|\alpha; R\rangle$ which propagate the bath DOF (characterized by masses M) on the potential energy surface (PES) $E_\alpha(R)$ when $\alpha = \alpha'$, or on the mean PES $[E_\alpha(R) + E_{\alpha'}(R)]/2$ when $\alpha \neq \alpha'$; and $\mathcal{J}_{\alpha\alpha',\beta\beta'}$ is the term responsible for nonadiabatic transitions given by

$$\mathcal{J}_{\alpha\alpha',\beta\beta'} = -\frac{P}{M} \cdot d_{\alpha\beta}\left(1 + \frac{1}{2}S_{\alpha\beta} \cdot \frac{\partial}{\partial P}\right)\delta_{\alpha'\beta'} - \frac{P}{M} \cdot d^*_{\alpha'\beta'}\left(1 + \frac{1}{2}S^*_{\alpha'\beta'} \cdot \frac{\partial}{\partial P}\right)\delta_{\alpha\beta}, \tag{2.12}$$

where $d_{\alpha\beta} = \langle \alpha; R|\frac{\partial}{\partial R}|\beta; R\rangle$ is the nonadiabatic coupling matrix element, and $S_{\alpha\beta} = (E_\alpha - E_\beta)d_{\alpha\beta}(\frac{P}{M} \cdot d_{\alpha\beta})^{-1}$. After representing the QCLE in this basis, its solution may be given by [84]

$$A_W^{\alpha\alpha'}(X,t) = \sum_{(\alpha_1\alpha'_1)\ldots(\alpha_{N_t}\alpha'_{N_t})} \Big[\prod_{j=1}^{N_t} (e^{i\hat{\mathcal{L}}\Delta t_j})_{\alpha_{j-1}\alpha'_{j-1},\alpha_j\alpha'_j}\Big] A_W^{\alpha_{N_t}\alpha'_{N_t}}(X), \tag{2.13}$$

where, in the limit that $\Delta t_j = t_j - t_{j-1}$ is sufficiently small, the propagator for time segment j may be approximated by

$$\begin{aligned}(e^{i\hat{\mathcal{L}}\Delta t_j})_{\alpha_{j-1}\alpha'_{j-1},\alpha_j\alpha'_j} \;\approx\;& \mathcal{W}_{\alpha_{j-1}\alpha'_{j-1}}(t_{j-1},t_j)e^{iL_{\alpha_{j-1}\alpha'_{j-1}}\Delta t_j} \\ & \times\left(\delta_{\alpha_{j-1}\alpha_j}\delta_{\alpha'_{j-1}\alpha'_j} + \Delta t\mathcal{J}_{\alpha_{j-1}\alpha'_{j-1},\alpha_j\alpha'_j}\right). \end{aligned} \tag{2.14}$$

In the above equations, N_t is the number of time segments and $\mathcal{W}_{\alpha_{j-1}\alpha'_{j-1}}(t_{j-1},t_j) = e^{i\omega_{\alpha_{j-1}\alpha'_{j-1}}\Delta t_j}$ is the phase factor associated with a given time segment. Finally, to arrive at an adiabatic approximation to the dynamics, one sets $\mathcal{J}_{\alpha_{j-1}\alpha'_{j-1},\alpha_j\alpha'_j} = 0$. Consequently, the evolution of the bath DOF is restricted to a single PES (or an average of two PESs) within a given trajectory, i.e., there are no nonadiabatic transitions.

To determine the expectation value of $\hat{A}_W(X,t)$, one averages over an ensemble of trajectories according to the following equation:

$$\begin{aligned} \langle A(t)\rangle &= \sum_{\alpha\alpha'} \int dX A_W^{\alpha\alpha'}(X,t)\rho_W^{\alpha'\alpha}(X) \\ &= \sum_{(\alpha_0\alpha'_0)\ldots(\alpha_{N_t}\alpha'_{N_t})} \int dX \Big[\prod_{j=1}^{N_t} (e^{i\hat{\mathcal{L}}\Delta t_j})_{\alpha_{j-1}\alpha'_{j-1},\alpha_j\alpha'_j}\Big] A_W^{\alpha_{N_t}\alpha'_{N_t}}(X)\rho_W^{\alpha'_0\alpha_0}(X), \end{aligned} \tag{2.15}$$

with the initial conditions for each trajectory sampled from the density matrix elements $\rho_W^{\alpha'_0\alpha_0}(X)$.

2.3 Deterministic Evolution of Coordinates with Initial Decoupled Equations (DECIDE)

The "Deterministic Evolution of Coordinates with Initial Decoupled Equations" (DECIDE) method allows one to simulate the time evolution of mixed quantum-classical systems with high accuracy, high stability, and relatively low computational cost [85]. In contrast to the surface-hopping solutions of the QCLE, [86–88] DECIDE represents both the subsystem and bath DOF in terms of continuous variables and does not involve stochastic hops between PESs.

The Weyl-ordered, partially-Wigner transformed (with respect to the initial bath coordinates) Hamiltonian that governs the dynamics of the composite system is

$$\hat{H} = \hat{H}_s(\hat{\boldsymbol{x}}) + \hat{H}_b(\boldsymbol{X}) + \hat{V}_c(\hat{\boldsymbol{x}}, \boldsymbol{X}), \tag{2.16}$$

where $\hat{\boldsymbol{x}} = (\hat{x}_1, \hat{x}_2, \cdots, \hat{x}_{L^2-1})$ denotes a set of generalized coordinates that completely describe the state of the subsystem of dimensionality L (the L^2-1 coordinates come from the number of independent elements in the reduced density matrix $\hat{\rho}$), $\hat{\boldsymbol{X}} = (\boldsymbol{R}, \boldsymbol{P})$ with $\boldsymbol{R} = (R_1, R_2, ..., R_N)$ and $\boldsymbol{P} = (P_1, P_2, ..., P_N)$, and $\hat{V}_c$ the subsystem-bath coupling potential. The DECIDE equations of motion may be derived by starting from the partially Wigner-transformed quantum Heisenberg equations for $\hat{\boldsymbol{x}}(t)$ and $\hat{\boldsymbol{X}}(t)$ and then truncating them by approximating an arbitrary time-dependent operator $(\hat{B}(\hat{\boldsymbol{x}}(t), \hat{\boldsymbol{X}}(t)))_W \equiv (e^{i\hat{\mathcal{K}}t}\hat{B}(\hat{\boldsymbol{x}}, \hat{\boldsymbol{X}}))_W$ as follows:

$$\begin{aligned} (\hat{B}(\hat{\boldsymbol{x}}(t), \hat{\boldsymbol{X}}(t)))_W &= (e^{i\hat{\mathcal{K}}t})_W e^{\hbar\Lambda/2i}\hat{B}_W(\hat{\boldsymbol{x}}, \boldsymbol{X}) \\ &\approx e^{i\hat{\mathcal{L}}t}\hat{B}_W(\hat{\boldsymbol{x}}, \boldsymbol{X}) \\ &\equiv (\hat{B}_W(\hat{\boldsymbol{x}}, \boldsymbol{X}))(t), \end{aligned} \tag{2.17}$$

where $\hat{\mathcal{K}}$ is the quantum Liouville operator and Λ is the Poisson bracket operator. From the second line of this equation, we see that the approximation involves replacing $\hat{\mathcal{K}}$ with the quantum-classical Liouville operator, $\hat{\mathcal{L}}$ [80] (which is exact for subsystems that are bilinearly coupled to harmonic environments), and retaining only zeroth-order terms in $\hbar$ in the Moyal product expansion. The higher order terms account for the full back-action of the bath(s) onto the subsystem. These approximations lead to the DECIDE equations of motion for the subsystem and bath coordinates:

$$\begin{aligned} \dot{\hat{\mathbf{x}}}(t) &= \frac{i}{\hbar}\left(\left[\hat{H}_W, \hat{\mathbf{x}}\right]\right)(t) \\ \dot{\mathbf{X}}(t) &= -\left(\left\{\hat{H}_W, \mathbf{X}\right\}_a\right)(t), \end{aligned} \tag{2.18}$$

where the time arguments are placed outside of their respective brackets to indicate that one should first evaluate the commutator and Poisson brackets with respect to the initial bath coordinates and then apply the time dependence to the coordinates in the resulting expressions. (For the detailed derivation of the DECIDE equations of motion, please see Ref. [85].) Given the aforementioned approximations, one sees that the DECIDE method may yield inaccurate results in parameter regimes where the subsystem dynamics is highly non-Markovian, e.g., in cases involving very strong subsystem-bath coupling, very slow heat baths, and very low temperatures. That being said, in regimes with weaker non-Markovian effects, the DECIDE method is expected to perform very well (as demonstrated in Refs. [85] and [54] and in Chapter 3 of this thesis).

To integrate the equations of motion in Eq. 2.18, one must cast them in a basis $\{|\alpha\rangle\}$ that spans the Hilbert space of the L-dimensional subsystem. For example, for a subsystem that is bilinearly coupled to a harmonic bath, the $L^2(L^2-1+2N)$ equations of motion for the matrix elements of $\hat{\mathbf{x}}(t)$ and $\mathbf{X}(t)$ take the following general form

$$\begin{aligned} \dot{\mathbf{x}}^{\alpha\alpha'}(t) &= F(\{\dot{\mathbf{x}}(t)^{\alpha\alpha'}\},\{(\hat{\mathbf{x}}(t)\mathbf{X}(t)+\mathbf{X}(t)\hat{\mathbf{x}}(t))^{\alpha\alpha'}\}) \\ \dot{\mathbf{X}}(t)^{\alpha\alpha'} &= G(\{\dot{\mathbf{x}}^{\alpha\alpha'}(t)\},\{\dot{\mathbf{X}}^{\alpha\alpha'}(t)\}), \end{aligned} \tag{2.19}$$

where $G \equiv -\left\langle \alpha|(\{\hat{H}_W,\mathbf{X}\}_a)(t)|\alpha'\right\rangle$ is a functional of the matrix elements $\dot{\mathbf{x}}^{\alpha\alpha'}(t)$ and $\dot{\mathbf{X}}^{\alpha\alpha'}(t)$, and $F \equiv \frac{i}{\hbar}\left\langle \alpha|([\hat{H}_W,\hat{\mathbf{x}}])(t)|\alpha'\right\rangle$ is a functional of the matrix elements $\dot{\mathbf{x}}(t)^{\alpha\alpha'}$ and $(\hat{\mathbf{x}}(t)\mathbf{X}(t)+\mathbf{X}(t)\hat{\mathbf{x}}(t))^{\alpha\alpha'}$ (i.e., matrix elements of the Weyl-ordered bilinear interaction term, which may be evaluated according to $(\hat{x}_l X_k)^{\alpha\alpha'} = \sum_\beta x_l^{\alpha\beta} X_k^{\beta\alpha'}$). The explicit forms of F and G must be worked out for the model under study. Thus, Eq. 2.19 represents a set of coupled first-order differential equations (FODEs), which can be numerically integrated to propagate $\mathbf{x}^{\alpha\alpha'}(t)$ and $\mathbf{X}(t)^{\alpha\alpha'}$.

After numerically integrating the coupled set of FODEs in Eq. 2.19 up to time t, one can construct the time-dependent expectation value of an observable $\hat{A}$ in terms of $\{\mathbf{x}^{\alpha\alpha'}(t)\}$

and $\{\mathbf{X}^{\alpha\alpha'}(t)\}$ as follows:

$$\langle A(t)\rangle = \sum_{\alpha\alpha'} \int d\boldsymbol{X}(0) A_W^{\alpha\alpha'}(\hat{\mathbf{x}}(t), \mathbf{X}(t)) \rho_W^{\alpha'\alpha}(\hat{\mathbf{x}}(0), \mathbf{X}(0)). \tag{2.20}$$

To evaluate the expectation value, we assume a factorized initial state of the form $\rho_W^{\alpha'\alpha}(\hat{\mathbf{x}}(0), \mathbf{X}(0)) = \rho_{B,W}(\mathbf{X}(0))\rho_S^{\alpha'\alpha}(\hat{\mathbf{x}}(0))$. We then specify the initial values of the matrix elements $\mathbf{x}^{\{\alpha\alpha'\}}(0)$ and $\mathbf{X}^{\{\alpha\alpha'\}}(0) = \mathbf{X}(0)\delta_{\{\alpha\alpha'\}}$, viz., $\mathbf{x}^{\{\alpha\alpha'\}}(0)$ is calculated after specifying the basis and $\mathbf{X}(0)$ is sampled from the bath distribution $\rho_{B,W}(\mathbf{X}(0))$. Starting from these initial conditions, one integrates Eq. 2.19 up to time t to obtain $(\mathbf{x}^{\{\alpha'\alpha\}}(t), \mathbf{X}^{\{\alpha'\alpha\}}(t))$ and evaluates the required terms in the integrand of Eq. 2.20. Finally, one averages over an ensemble of trajectories to compute the expectation value $\langle A(t)\rangle$.

The DECIDE methodology has several advantages over mixed quantum-classical surface-hopping approaches: (i) The time evolution prescribed by the equations of motion is deterministic, which results in numerically stable results out to long times; (ii) The scaling of this method is polynomial in L and N, as it only requires the integration of at most $L^2(L^2 - 1 + 2N)$ coupled equations; (iii) There is no need to diagonalize the Hamiltonian matrix on-the-fly; (iv) No momentum jump approximation is made; (v) The time evolution is not mean-field in nature.

Chapter 3

Quantum-classical Dynamics of Nonequilibrium Heat Transport in a Model Molecular Junction

3.1 Introduction

The study of nonequilibrium heat transport in nanoscale systems has gathered much attention over the years due to its crucial role in the operation of molecular electronic devices [89–96]. Gaining control of the heat transport dynamics has led to the design of novel phononic devices with unique functionalities. Some examples of devices include thermal rectifiers (which allow heat flow in one direction and impede it in the opposite direction) [21, 97–106], thermal transistors (which switch between insulating and conducting states, and amplify heat flow) [21, 107–109], and thermal logic gates (which perform basic logic operations) [110]. The nonequilibrium spin-boson (NESB) model [44, 60, 111–113] has served as a simple prototype for exploring and understanding heat transport through molecular junctions, such as those found in phononic devices. This model consists of a two-level spin (representing the junction molecule) in contact with two independent harmonic oscillator baths at different temperatures (representing the thermal reservoirs). Owing to its simplicity, the NESB model has also been used to test a variety of approximate quantum dynamical methods for calculating both time-dependent and steady-state heat currents across a wide range of parameter regimes [41, 44, 63, 95, 97, 110, 114, 115].

A number of numerically exact and approximate quantum dynamical methods have been used to calculate heat currents in the NESB model. Redfield theory has proven to be reliable in the very weak system-bath coupling regime [44], while the noninteracting-blip approximation works best in the strong system-bath coupling regime and at high temperatures [112, 116]. The nonequilibrium polaron-transformed Redfield equation has been used to derive a unified heat current expression for the NESB model, which reduces to the Redfield and the noninteracting-blip approximation ones in the weak and strong coupling limits, respectively [63]. Perturbative methods based on the nonequilibrium Green's function [117, 118] approach perform reasonably well up to intermediate system-bath couplings, while the polaron-transformed version of this method [119] extends its validity into the strong system-bath coupling regime. Numerically exact methodologies such as the quasi-adiabatic propagator path integral [42–44], influence functional path integral [120], Monte Carlo [48], and multilayer multiconfiguration time-dependent Hartree (ML-MCTDH) [41] methods are capable of producing accurate results across a wide range of system-bath coupling strengths and nonadiabaticities, but at high computational costs [44, 121].

When dealing with larger and more complex systems, mixed quantum-classical methods, which treat the junction molecule quantum mechanically and the thermal reservoirs in a classical-like way, can more efficiently simulate the composite system (i.e., system plus bath) dynamics. Recently, a mixed quantum-classical framework for calculating heat transport properties in molecular junctions was developed [54]. This framework was built on the full counting statistics approach [122] and formally relies on the quantum-classical Liouville equation (QCLE) [80, 123–125] for prescribing the composite system dynamics. In practice, however, any mixed quantum-classical method that can be derived from an approximate solution of the QCLE, could be used to simulate the dynamics of the composite system. To date, Ehrenfest dynamics and the "Deterministic Evolution of Coordinates with Initial Decoupled Equations" (DECIDE) method [85], which can both be derived from the QCLE, have been used to calculate time-dependent heats and heat currents for the NESB model in a variety of parameter regimes. The Ehrenfest method is capable of qualitatively capturing the expected trends in the steady-state heat current as a function of the tunnelling frequency of the two-level system and the system-bath coupling strength; however, it gives substantial quantitative deviations from the numerically exact results at lower temperatures and intermediate to strong coupling strengths due to its mean-field nature [58]. In Ref. [54], the DECIDE method was simply used to demonstrate the proposed framework for calculating time-dependent heats and heat currents on a small number of parameter sets.

In this Chapter, we investigate the ability of the DECIDE method to qualitatively and quantitatively capture the exact turnover behaviours observed in ML-MCTDH plots [41] of the steady-state heat current as a function of the tunnelling frequency of the two-level system and the system-bath coupling strength, respectively, at different bath temperatures. Generation of these turnovers provides a strong indication that the approximate method is capable of correctly capturing the physics of the heat transport across a wide range of parameter regimes. We also compare our DECIDE results to those obtained using Ehrenfest dynamics [58] and mixed quantum-classical adiabatic dynamics. Any differences observed between the DECIDE (an inherently nonadiabatic method) and adiabatic dynamics results would shed light on the importance of nonadiabatic effects in the heat transport dynamics; while any differences observed between the DECIDE and Ehrenfest dynamics results would be indicative of breakdowns in a mean-field-type description of the heat transport dynamics.

This Chapter is organized as follows. In Sec. 3.2, we provide the heat and heat current expressions. In Sec. 3.3 we present the simulation details, in Sec. 3.4, we present and discuss our simulation results within the context of the numerically exact and other mixed quantum-classical results. Finally, we summarize our findings in Sec. 3.5.

3.2 Heat and heat current expressions

To evaluate the heats and heat currents in the NESB model (fully described in Sec. 1.3) using mixed quantum-classical dynamics, we must specify their expressions in the partial Wigner representation. In this representation, the expression for the average heat transferred from the vth heat bath to the subsystem is given by [54]

$$\begin{aligned}\langle Q_v(t)\rangle &= \langle \hat{H}_B^v(t) - \hat{H}_B^v(0)\rangle \\ &= \sum_{\alpha\alpha'} \int d\boldsymbol{X}(0)\rho_{B,W}(\boldsymbol{X}(0))\rho_S^{\alpha'\alpha}(0)\left[\hat{H}_B^v(t) - \hat{H}_B^v(0)\right]^{\alpha\alpha'}, \end{aligned} \tag{3.1}$$

where $\hat{H}_B^v = \sum_{j=1}^{N_v}\left(P_{j,v}^2 + \omega_{j,v}^2 R_{j,v}^2\right)$ is the Hamiltonian of the vth heat bath, $\{|\alpha\rangle\}$ denotes a complete set of basis states that span the Hilbert space of the quantum subsystem. By extension, the time-dependent heat current $\langle J_v(t)\rangle$ of the vth bath is defined as the time derivative of $\langle Q_v(t)\rangle$:

$$\langle J_v(t)\rangle = \frac{d}{dt}\langle Q_v(t)\rangle. \tag{3.2}$$

In our simulations, $\langle J_v(t)\rangle$ is obtained by simply calculating the derivative of $\langle Q_v(t)\rangle$ at each time step. In general, the short-time behaviour of $\langle J_L(t)\rangle$ is different from that of

$\langle J_R(t)\rangle$. However, in the long-time limit, $\langle J_L(t)\rangle$ and $\langle J_R(t)\rangle$ will reach their steady state values and $J = |\langle J_L(\infty)\rangle| = |\langle J_R(\infty)\rangle|$ is the steady-state heat current. Alternatively, the steady-state heat current can be calculated from

$$J = \lim_{t\to\infty} J(t) = \lim_{t\to\infty} \frac{1}{2}\left[\langle J_L(t)\rangle - \langle J_R(t)\rangle\right]. \tag{3.3}$$

3.3 Simulation details

The initial state of the system is chosen to be the product state $\hat{\rho}_W(0) = \hat{\rho}_S(0)\rho_{B,W}(0)$, where $\hat{\rho}_S(0) = |+\rangle\langle+|$ (where $|+\rangle$ is the spin-up state of $\hat{\sigma}_z$) and $\rho_{B,W}(0) = \prod_v \rho^v_{B,W}(0)$ with

$$\begin{aligned}\rho^v_{B,W}(0) &= \prod_{j=1}^{N_v} \frac{\tanh(\hbar\beta_v\omega_{j,v}/2)}{\pi} \exp\left[-\frac{2\tanh(\hbar\beta_v\omega_{j,v}/2)}{\hbar\omega_{j,v}}\right.\\ &\qquad \left.\times\left(\frac{P^2_{j,v}}{2} + \frac{\omega^2_{j,v}R^2_{j,v}}{2}\right)\right],\end{aligned} \tag{3.4}$$

the partially Wigner-transformed canonical distribution of the vth bath.

In our DECIDE simulations of the NESB model, we take the coordinates of the spin subsystem to be the Pauli matrices, i.e., $\hat{\boldsymbol{x}} = (\hat{\sigma}_x, \hat{\sigma}_y, \hat{\sigma}_z)$. Casting the equations of motion in Eq. (2.18) in an arbitrary basis $\{|\alpha\rangle\}$ (spanning the 2×2 Hilbert space of the spin) and working out the expressions on the right-hand side of Eq. (2.18) using the NESB Hamiltonian in Eq. (1.4), leads to the following set of coupled first-order differential equations:

$$\begin{aligned}
\dot{\sigma}_x^{\alpha\alpha'}(t) &= -\frac{1}{\hbar}\sum_v \sum_{j=1}^{N_v} C_{j,v}[R_{j,v}(t)\hat{\sigma}_y(t) + \hat{\sigma}_y(t)R_{j,v}(t)]^{\alpha\alpha'}, \\
\dot{\sigma}_y^{\alpha\alpha'}(t) &= -2\Delta\sigma_z^{\alpha\alpha'}(t) + \frac{1}{\hbar}\sum_v \sum_{j=1}^{N_v} C_{j,v}[R_{j,v}(t)\hat{\sigma}_x(t) \\
&\quad +\hat{\sigma}_x(t)R_{j,v}(t)]^{\alpha\alpha'}, \\
\dot{\sigma}_z^{\alpha\alpha'}(t) &= 2\Delta\sigma_y^{\alpha\alpha'}(t), \\
\dot{R}_{j,v}^{\alpha\alpha'}(t) &= P_{j,v}^{\alpha\alpha'}(t), \\
\dot{P}_{j,v}^{\alpha\alpha'}(t) &= -\omega_{j,v}^2 R_{j,v}^{\alpha\alpha'}(t) - C_{j,v}\sigma_z^{\alpha\alpha'}(t), \qquad (3.5)
\end{aligned}$$

where the dot denotes a time derivative. In Eq. (3.5), there are $4\times(3+2N)$ (with $N = N_L + N_R$) first order differential equations for the matrix elements $(\sigma_x^{\{\alpha\alpha'\}}, \sigma_y^{\{\alpha\alpha'\}}, \sigma_z^{\{\alpha\alpha'\}}, \boldsymbol{X}^{\{\alpha\alpha'\}})$, where $\{\alpha\alpha'\}$ implies that all the combinations of basis indices are considered.

To evaluate the matrix elements in Eq. (3.5), we use the subsystem basis, which consists of the eigenstates of $\hat{\sigma}_z$, i.e., $\{|\alpha\rangle\} = \{|+\rangle, |-\rangle\}$. Using this basis, the initial values of the matrix elements of the spin coordinates are evaluated as $\sigma_x^{+-}(0) = \sigma_x^{-+}(0) = 1$, $\sigma_x^{++}(0) = \sigma_x^{--}(0) = 0$, $\sigma_y^{++}(0) = \sigma_y^{--}(0) = 0$, $\sigma_y^{-+} = i, \sigma_y^{+-} = -i$, $\sigma_z^{+-}(0) = \sigma_z^{-+}(0) = 0$, $\sigma_z^{++}(0) = 1, \sigma_z^{--}(0) = -1$; the initial values of the matrix elements of the bath coordinates are evaluated as $\boldsymbol{X}^{\alpha\alpha'}(0) = \boldsymbol{X}(0)\delta_{\alpha\alpha'}$ (since the spin and bath are initially decoupled), with $\boldsymbol{X}(0)$ sampled from Eq. (3.4); and the expression for the average transferred heat in Eq. (3.1) becomes

$$\begin{aligned}
\langle Q_v(t)\rangle &= \int d\boldsymbol{X}(0)\rho_{B,W}^v(\boldsymbol{X}(0))\sum_{j=1}^{N_v}\left[\frac{(P_{j,v}^2(t))^{++} - P_{j,v}^2(0)}{2}\right. \\
&\quad \left. +\omega_{j,v}^2\frac{(R_{j,v}^2(t))^{++} - R_{j,v}^2(0)}{2}\right], \qquad (3.6)
\end{aligned}$$

where we have used the fact that $\rho_S^{++}(0) = 1$.

The fourth-order Runge-Kutta scheme [126] is used to integrate the set of first order differential equations in Eq. (3.5), which yields the values of the matrix elements of the time-dependent spin and bath coordinates. Finally, noting that, for example, $\left(P_{j,v}^2(t)\right)^{\alpha\alpha'} = \sum_\beta P_{j,v}^{\alpha\beta}(t) P_{j,v}^{\beta\alpha'}(t)$ (where $P_{j,v}^{\alpha\alpha'}(t) \neq P_{j,v}(t)\delta_{\alpha\alpha'}$, since its value depends on the subsystem's operators at time t due to the subsystem-bath coupling), the time-dependent average heat and heat current can then be generated in terms of the matrix elements of the time-dependent bath coordinates by averaging over an ensemble of trajectories according to Eqs. (3.6) and (3.2), respectively. To obtain converged results, ensembles of 10^7 trajectories and a time step of $\Delta t = 0.2654$ fs are used.

In the adiabatic dynamics simulations, the average heat transferred from the vth bath to the subsystem is calculated according to

$$\begin{aligned} \langle Q_v(t) \rangle &= \sum_{\alpha\alpha'} \int d\boldsymbol{X}(0) \left[H_B^v(\boldsymbol{X}(0), t) - H_B^v(\boldsymbol{X}(0)) \right]^{\alpha\alpha'} \rho_{B,W}^v(\boldsymbol{X}(0)) \rho_S^{\alpha'\alpha}(0) \\ &= \sum_{\alpha} \int d\boldsymbol{X} \left[(H_B^v(\boldsymbol{X}(0), t))^{\alpha\alpha} - H_B^v(\boldsymbol{X}(0)) \right] \rho_{B,W}^v(\boldsymbol{X}(0)) \rho_S^{\alpha\alpha}(0) \end{aligned} \qquad (3.7)$$

where $\{|\alpha\rangle\}$ now denotes the adiabatic basis defined previously and the matrix element $(H_B^v(\boldsymbol{X}, t))^{\alpha\alpha}$ is evolved in time according to Eq. (2.13). To arrive at the second line of the above equation, we have used the facts that the heat current only depends on the bath coordinates and that the state of the subsystem, α, does not change over the course of the dynamics. The initial values of the left and right bath coordinates, $\boldsymbol{X}(0)$, are sampled from Eq. (3.4). Finally, the time-dependent average heat and heat current are generated by averaging over an ensemble of trajectories according to Eqs. (3.7) and (3.2), respectively. To obtain converged results, ensembles of 10^7 trajectories and a time step of $\Delta t = 0.2654$ fs are used.

To extract the steady-state heat current, J, from the time-dependent heat current, $J(t)$, we average all the values of $J(t)$ for $t > t^*$, where t^* denotes a time after which $J(t)$ remains essentially constant. (Based on our simulation results, we took $t^* = 200$ fs.) Next, to compute the error bar in the steady state heat current, we bin the time-dependent heat current values for $t > t^*$ into time-ordered sets of width 20 fs, then calculate the average heat current for each bin, and finally calculate the standard deviation of the bin averages.

3.4 Results and discussion

We now present the results of the time-dependent average heat and heat current and the steady-state heat current for the NESB model for a variety of (left and right) bath temperatures, bath reorganization energies, and tunneling frequencies computed using the DECIDE method and adiabatic dynamics. Our results are compared and contrasted with those of the numerically exact multi-layer multi-configurational time-dependent Hartree (ML-MCTDH) method (from Ref. [41]), Bloch-Redfield theory (BR) (from Ref. [41]), and Ehrenfest mean-field theory (MFT) (from Ref. [58]). In all of our simulations, $N_L = N_R = 100$, $\omega_c = 400\ \mathrm{cm}^{-1}$, and $\omega_m = 2000\ \mathrm{cm}^{-1}$.

Figure 3.1a shows the time-dependent heats of the left (cold) and right (hot) baths calculated using the DECIDE method for the case of $T_L = 60$ K, $T_R = 120$ K, $E_r = 100\ \mathrm{cm}^{-1}$, and $\Delta = 300\ \mathrm{cm}^{-1}$. After the sudden switch-on of the subsystem-bath coupling at $t = 0$, both the heats of the left and right baths exhibit large increases in the first $\sim$150 fs. This behaviour has been previously observed in a nanoscale thermal switch model [127] and is due to energy added in the form of the switched coupling potential. After this transient time, there is a linear increase in the left-bath heat and a linear decrease in the right-bath heat, as expected. As can be seen, the DECIDE results are in excellent agreement with the ML-MCTDH ones at short times, but exhibit slight deviations at later times, with differences ranging from ~ 2 cm^{-1} to ~ 6 cm^{-1}. Figure 3.1b depicts the corresponding time-dependent heat currents of the left and right baths. It should be noted that the ML-MCTDH time-dependent heat currents were calculated by taking the time derivative of the sum of the bath and subsystem-bath coupling energies [41], in contrast to our definition in Eq. (3.2). Thus, differences between the two sets of results are expected at short times, but both definitions should give the same long-time limit. Initially, the heat currents of the left and right baths rise rapidly (due to the sudden switch-on of the system-bath coupling) to their maximum values, and then decrease slowly to their steady-state values. As can be seen, the DECIDE results are in very good agreement with the ML-MCTDH ones at long times. In the inset of Figure 3.1b, we present a comparison between the time-dependent heat currents $J(t)$ (obtained using DECIDE) and $J'(t)$ (obtained using ML-MCTDH). From this plot, one can see that, despite some noise in $J(t)$, the long-time limits of $J(t)$ and $J'(t)$ are in very good agreement with each other. For this particular parameter set, the difference between the exact result and that obtained by DECIDE is $\sim$0.004 cm^{-1}fs^{-1}. These results demonstrate the ability of DECIDE for accurately predicting the time-dependent heats and heat currents in the limit that $\omega_c > \Delta$ and $k_B T < \Delta$.

In Fig. 3.2, we plot the steady-state heat currents obtained using the various approaches for the case of $T_L = 60$ K, $T_R = 120$ K, and $\Delta = 300$ cm^{-1} as a function of the reorganization energy, E_r. At low reorganization energies, the DECIDE, MFT, and BR results are seen to be in good agreement with the ML-MCTDH result, with the BR result agreeing exactly with the ML-MCTDH one. Particularly, the differences between the exact and DECIDE results are $\sim$0.0001 cm^{-1}fs^{-1} and $\sim$0.004 cm^{-1}fs^{-1} for $E_r = 50$ cm^{-1} and $E_r = 100$ cm^{-1}, respectively. These results strongly suggest that these methods can yield reliable results in weak subsystem-bath coupling situations. As the reorganization energy is increased, the DECIDE and MFT results exhibit the expected turnover [128, 129], while the BR result

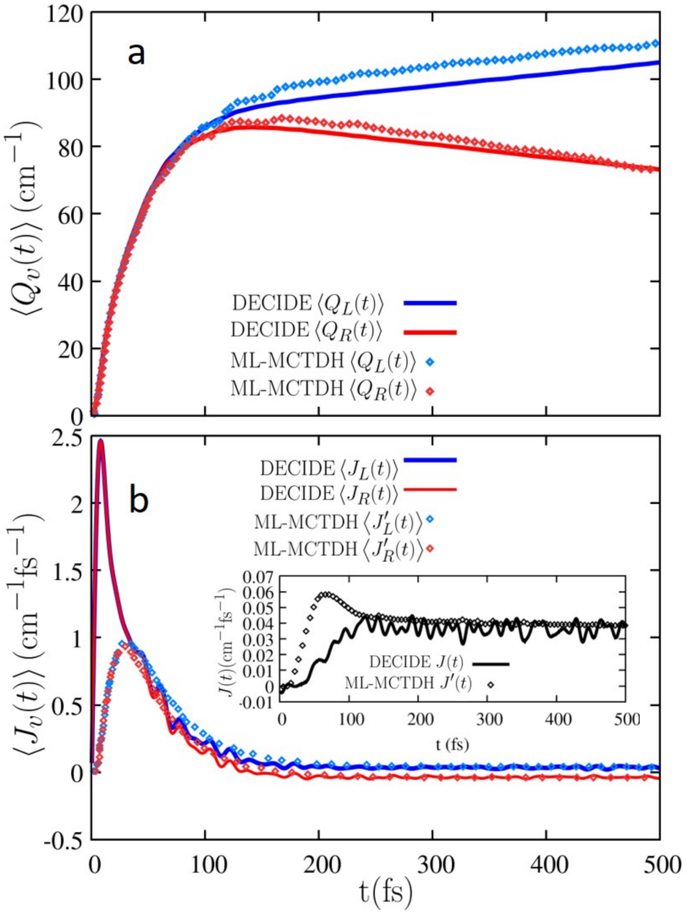

Figure 3.1: Time-dependent heats, $\langle Q_v(t)\rangle$, (top panel) and heat currents, $\langle J_v(t)\rangle$, (bottom panel) of the left and right baths obtained using the DECIDE method with 10^7 trajectories. The simulation parameters used are T_L = 60 K, T_R = 120 K, ω_c = 400 cm^{-1}, E_r = 100 cm^{-1}, $N_L = N_R = 100$, and Δ = 300 cm^{-1}. For comparison, the numerically exact ML-MCTDH results for $\langle J'_L(t)\rangle$, $\langle J'_R(t)\rangle$, and $J'(t)$ are shown [41]. The inset shows a comparison between the time-dependent heat currents $J(t)$ and $J'(t)$ obtained with DECIDE and ML-MCTDH, respectively.

continues to grow linearly. The turnover can be explained in the following way. In the weak system-bath coupling regime, the system-bath coupling strength directly determines the effectiveness of the heat transfer between the system and the baths; therefore, a larger coupling strength leads to a larger heat current. However, as the system-bath coupling strength further increases (to a point in the intermediate coupling regime), the bath friction begins to limit the heat transfer (due to slow diffusion processes in the baths which dissipate the heat away from the system) and the heat current begins to decrease. Beyond $\sim$100 cm^{-1}, we see that all of the mixed quantum-classical methods underestimate the steady-state heat current, with DECIDE exhibiting markedly closer agreement with the exact result than MFT for the largest reorganization energies. For this case, the differences observed between the exact and approximate results range from 0.01 to 0.04 cm^{-1}fs^{-1} and 0.02 to 0.3 cm^{-1}fs^{-1} for MFT and DECIDE, respectively. Moreover, we see that DECIDE predicts the correct value of E_r at which the turnover takes place, viz., $E_r = 300$ cm^{-1}. Thus, at the stronger coupling strengths, DECIDE captures nonadiabatic effects that are neglected by a mean-field treatment of the heat transport dynamics. As for adiabatic dynamics, we see that it does not perform well for most reorganization energies (except for $E_r = 400$ cm^{-1}) and does not capture the expected turnover behaviour. These observations indicate that nonadiabatic effects are important in the heat transport dynamics across a wide range of subsystem-bath coupling strengths.

Figure 3.3 displays the dependence of the steady-state heat current on the reorganization energy for the higher bath temperatures of $T_L = 100$ K and $T_R = 150$ K (with $\Delta = 300$ cm^{-1}). We see that the trends and relative agreements between the approximate results and the exact result are the same as for the lower bath temperature case. However, at higher bath temperatures, we observe a substantial improvement in the quantitative agreement between the DECIDE/MFT results and the exact ones, with DECIDE performing markedly better than MFT over a wider range of reorganization energies than at the lower bath temperatures. Given the nature of the underlying approximations in the DECIDE method, this improvement in performance is expected. This likely explains why the DECIDE results are in very good agreement with the exact ones in the range of $E_r = 300$ cm^{-1} to $E_r = 500$

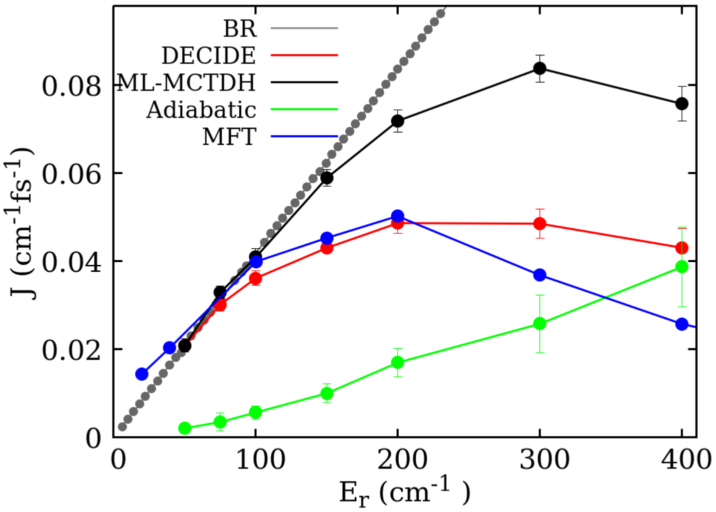

Figure 3.2: Steady-state heat current as a function of the bath reorganization energy, E_r, obtained using DECIDE and adiabatic dynamics with 10^7 trajectories. The simulation parameters used are $T_L = 60$ K, $T_R = 120$ K, $\omega_c = 400$ cm^{-1}, $\omega_m = 2000$ cm^{-1}, $N_L = N_R = 100$, and $\Delta = 300$ cm^{-1}. For comparison, the numerically exact ML-MCTDH results [41], along with the approximate BR [41] and MFT [58] results are shown.

cm^{-1}. As in the lower bath temperature case, we see that DECIDE captures nonadiabatic effects that are neglected by MFT and that nonadiabatic effects are important across a wide range of subsystem-bath coupling strengths.

The effect of the energy difference between the two spin states, Δ, on the steady-state heat current is shown in Fig. 3.4 for the case of $T_L = 100$ K, $T_R = 150$ K, and $E_r = 100$ cm^{-1}. As Δ is increased, we see that the BR, MFT, and DECIDE results exhibit turnovers, while the adiabatic dynamics result does not. This turnover occurs due to the resonant character of the heat transport, viz., the steady-state heat current increases initially with increasing Δ up to a certain value of Δ at which there is the maximal number of in-resonance bath modes; after which, the steady-state heat current decreases due to a reduction in the number of in-resonance bath modes [44]. Despite exhibiting turnovers, the BR, MFT, and DECIDE

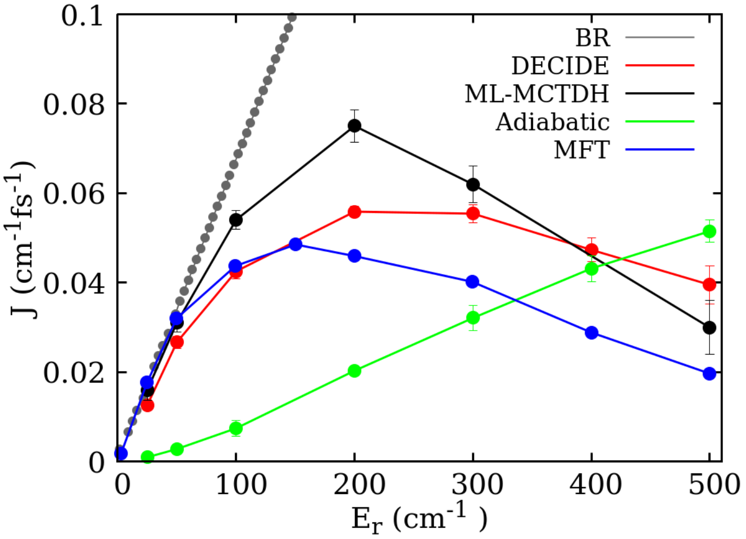

Figure 3.3: Steady-state heat current as a function of the bath reorganization energy, E_r, obtained using DECIDE and adiabatic dynamics with 10^7 trajectories. The simulation parameters used are $T_L = 100$ K, $T_R = 150$ K, $\omega_c = 400$ cm^{-1}, $\omega_m = 2000$ cm^{-1}, $N_L = N_R = 100$, and $\Delta = 300$ cm^{-1}. For comparison, the numerically exact ML-MCTDH results [41], along with the approximate BR [41] and MFT [58] results are shown.

results have substantial quantitative differences. Overall, BR theory exhibits the largest deviations from the exact results (compared to MFT and DECIDE) over the entire range of Δ values. MFT and DECIDE perform similarly up to $\Delta = 200$ cm^{-1}. MFT predicts the turnover to occur at $\Delta \approx 200$ cm^{-1}, while DECIDE predicts it to occur at $\Delta \approx 300$ cm^{-1}, in excellent agreement with the turnover point given by ML-MCTDH. Beyond $\Delta \approx 400$ cm^{-1}, we see that DECIDE yields results that are in very close agreement with the exact ones, while MFT yields significantly smaller values, viz., we find absolute differences of 0.004, 0.003, and 0.003 cm^{-1} fs^{-1} for DECIDE and 0.019, 0.004, and 0.002 cm^{-1} fs^{-1} for MFT at $\Delta = 500$ cm^{-1}, $\Delta = 800$ cm^{-1}, and $\Delta = 1000$ cm^{-1}, respectively. Interestingly, adiabatic dynamics yields very good agreement with the exact results starting at $\Delta = 800$ cm^{-1}. This is consistent with the adiabatic approximation, which is expected to improve in the slow-bath limit, i.e., $\omega_c \ll \Delta$.

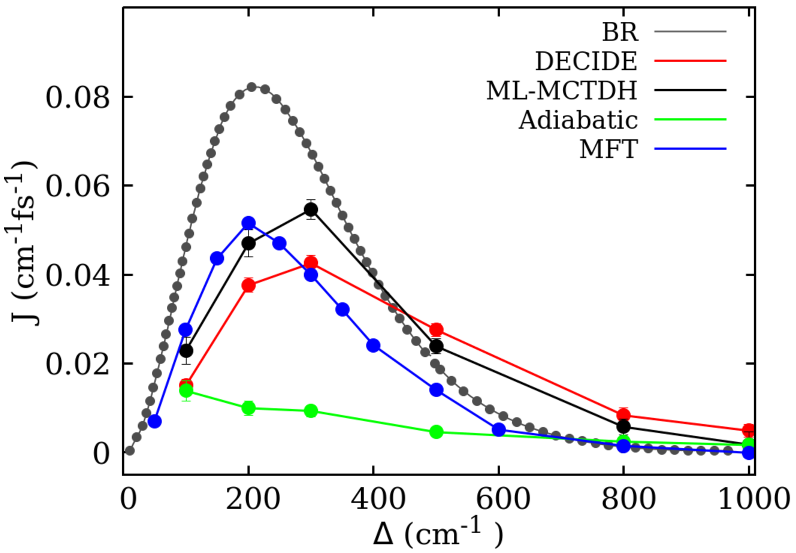

Figure 3.4: Steady-state heat current as a function of the tunneling frequency of the two-level spin system, Δ, obtained using DECIDE and adiabatic dynamics with 10^7 trajectories. The simulation parameters used are $T_L = 100$ K, $T_R = 150$ K, $\omega_c = 400$ cm^{-1}, $\omega_m = 2000$ cm^{-1}, $N_L = N_R = 100$, and $E_r = 100$ cm^{-1}. For comparison, the numerically exact ML-MCTDH results [41], along with the approximate BR [41] and MFT [58] results are shown.

3.5 Summary

In this work, we investigated the ability of the DECIDE method for calculating steady-state heat currents in the nonequilibrium spin-boson model. This was accomplished by contrasting our results with those of the numerically exact ML-MCTDH method. In the $\omega_c > \Delta$ limit, DECIDE was found to be capable of capturing the expected turnover in the steady-state heat current as a function of the bath reorganization energy for both lower and higher bath temperatures, with good to excellent quantitative agreement across the range of reorganization energies considered. Overall, the agreement was better in the case of the higher bath temperatures. Moreover, DECIDE was found to be capable of capturing the expected turnover in the steady-state heat current as a function of the tunneling frequency for the bath temperatures considered.

We also made comparisons between the DECIDE results and those of other mixed quantum-classical methods, namely mean-field theory and adiabatic dynamics. In the fast-bath limit, adiabatic dynamics is not capable of qualitatively capturing the expected trends in the steady-state heat current with respect to the reorganization energy and tunneling frequency, regardless of the bath temperatures. This observation underscores the fact that nonadiabatic effects play an important role in the heat transfer dynamics across a wide range of parameter regimes. On the other hand, mean field theory is capable of capturing the expected trends for the parameter regimes considered; overall, however, it did not yield as accurate steady-state heat currents as DECIDE, nor did it exactly predict the turnover points as in the case of DECIDE. Our findings hold promise for DECIDE simulations of nonequilibrium heat transport in more realistic systems, for which fully quantum mechanical approaches are not computationally feasible.

Chapter 4

Quantum Bath Effects on Nonequilibrium Heat Transport in Model Molecular Junctions

4.1 Introduction

During the last two decades, great efforts have been devoted to modelling heat transfer at the nanoscale [89–96, 130, 131]. As a result, a number of applications have been proposed, including thermal diodes[21, 97–106], thermal logic gates [110, 132], thermal transistors [21, 107–109], quantum heat engines [132, 133] and quantum absorption refrigerators [134, 135]. Optimizing the heat currents in these nanophononic devices represents a formidable challenge for both theory and experiment. From a theoretical standpoint, the non-equilibrium spin boson (NESB) model has become a prototype for the study of quantum heat transport [44, 112, 136]. This model, which consists of a two-level spin coupled to two harmonic oscillator baths at different temperatures, has been shown to capture several phenomenological features of molecular junctions. A large number of quantum methods have been used to simulate the heat transport dynamics of this model, including Redfield theory [44], mean field theory [58], the noninteracting-blip approximation [112, 116], the nonequilibrium polaron-transformed Redfield equation [63], methods based on the nonequilibrium Green's function [117, 118], perturbative approaches [137], nonequilibrium variational polaron theory [138], extended hierarchy equation of motion [139], quasi-adiabatic propagator path integral [42–44], influence functional path integral [120], Monte Carlo [48], and multilayer multiconfiguration time-dependent Hartree (ML-MCTDH) [40, 41]. Recently, we also applied a novel mixed quantum-classical dynamics method, known as DECIDE [85] (which stands for "Deterministic Evolution of Coordinates with Initial Decoupled Equations"), to the NESB model, and obtained qualitative to semi-quantitative agreement with the exact results over a wide parameter regime [51].

When simulating heat transport through a molecular junction, one of the main quantities of interest is the steady-state heat current. This heat current is often calculated by averaging over initial conditions that are sampled from thermal distributions of the bath positions and momenta. In previous studies of the NESB model, it has been calculated by averaging over *quantum* thermal distributions of the positions and momenta of the bath harmonic oscillators. Beyond the NESB model, the use of quantum bath distributions for calculating heat transport properties in more complex systems has been rather limited [140, 141]. Such systems are typically studied using classical molecular dynamics, with the initial bath conditions sampled from *classical* thermal distributions. Due to its versatility and relatively low computational cost, this approach has enabled the calculation of thermal properties in a wide variety of nanoscale systems at higher temperatures, including graphene [142], fullerene derivatives [143], phononic-like membranes [144], multilayer MoS_2 [145], amorphous polymers [146], nanofluids [147], two-dimensional polyaniline structures [148], and metal-organic frameworks [149]. At low temperatures, it is expected that quantum bath distribution effects on the heat currents will be significant; however, it is unclear how these effects are influenced by other bath parameters and the system-bath coupling strength over a wide range of temperatures.

In the present chapter, we set out to investigate the importance of quantizing the initial thermal bath distributions in calculating time-dependent heats and heat currents across a wide range of bath parameter regimes of the NESB model, viz., bath temperatures, bath temperature gaps, bath reorganization energies, and bath cutoff frequencies. This is done by contrasting the results of mixed quantum-classical dynamics simulations starting from both quantum and classical bath distributions. Our findings shed light on the parameter regimes in which quantum bath sampling is deemed important and, indirectly, on ways of engineering thermal reservoirs to maximize/minimize heat currents through molecular junctions.

This chapter is organized as follows. In Sec. 4.2, we present the statistical expressions used to calculate the heat current starting from both quantum and classical thermal bath distributions. The simulation details, results, and summary are provided in Sections 4.3, 4.4 and 4.5, respectively.

4.2 Heat current from quantum and classical distributions

The average amount of energy flowing from the vth bath to the spin within a time t defines the time-dependent heat, i.e.,[54]

$$\begin{aligned} \langle Q_v(t)\rangle &= \langle \hat{H}_B^v(t) - \hat{H}_B^v(0)\rangle \\ &= \sum_{\alpha\alpha'} \int d\boldsymbol{X}(0)\rho_W^{\alpha'\alpha}(0)\left[\hat{H}_B^v(t) - \hat{H}_B^v(0)\right]^{\alpha\alpha'}, \end{aligned} \tag{4.1}$$

where $\hat{H}_B^v = \frac{1}{2}\sum_{j=1}^{N_v}\left(P_{j,v}^2 + \omega_{j,v}^2 R_{j,v}^2\right)$ is the Hamiltonian of the vth bath, $\rho_W^{\alpha'\alpha}$ is a partially Wigner-transformed density matrix element corresponding to the composite system, $\{|\alpha\rangle\}$ denotes a complete set of basis states that span the Hilbert space of the two-level spin subsystem, and $\boldsymbol{X} = (\boldsymbol{R}, \boldsymbol{P})$ denotes the set of positions and momenta of the baths. It follows that the time-dependent heat current $\langle J_v(t)\rangle$ of the vth bath is given by

$$\langle J_v(t)\rangle \;=\; \frac{d}{dt}\langle Q_v(t)\rangle. \tag{4.2}$$

In the long-time limit, the composite system reaches a steady state at which $|\langle J_L(\infty)\rangle| = |\langle J_R(\infty)\rangle| = J$, thereby defining the steady-state heat current. Equivalently, one may express the steady-state heat current as

$$J = \lim_{t\to\infty}\frac{1}{2}\left[\langle J_L(t)\rangle - \langle J_R(t)\rangle\right] \equiv \lim_{t\to\infty} J(t), \tag{4.3}$$

where $J(t) = \frac{1}{2}\left[\langle J_L(t)\rangle - \langle J_R(t)\rangle\right]$, i.e., the average of the absolute values of the left and right bath heat currents (this can be understood by noting that that the steady-state heat currents of the left and right baths are expected to be positive and negative, respectively, because T_L will always be chosen to be less than T_R).

As is commonly done, the initial state of the system is taken to be the product state $\hat{\rho}_W(0) = \hat{\rho}_S(0)\rho_{B,W}(0)$, where $\hat{\rho}_S(0) = |+\rangle\langle+|$ ($|+\rangle$ is the spin-up state of $\hat{\sigma}_z$) and $\rho_{B,W}(0) = \prod_v \rho_{B,W}^v(0)$ with

$$\begin{aligned}\rho_{B,W}^v(0) \;&=\; \prod_{j=1}^{N_v}\frac{\tanh(\hbar\beta_v\omega_{j,v}/2)}{\pi}\exp\left[-\frac{2\tanh(\hbar\beta_v\omega_{j,v}/2)}{\hbar\omega_{j,v}}\left(\frac{P_{j,v}^2}{2} + \frac{\omega_{j,v}^2 R_{j,v}^2}{2}\right)\right]\\ &\equiv\; \rho_{B,q}^v(0),\end{aligned} \tag{4.4}$$

the partially Wigner-transformed canonical distribution of the vth bath. This distribution accounts for the quantum equilibrium structure of the collection of harmonic oscillators. From this expression, one can recover the classical Boltzmann distribution by taking the high temperature limit $\lim_{\beta\to 0}\rho^{v}_{B,W}(0)$:

$$\rho^{v}_{B,cl}(0) \quad = \quad \prod_{j=1}^{N_v} \frac{\beta_v \omega_{j,v}\hbar}{2\pi} \exp\left[-\beta_v\left(\frac{P^2_{j,v}}{2}+\frac{\omega^2_{j,v}R^2_{j,v}}{2}\right)\right]. \tag{4.5}$$

The fully quantum and classical bath distributions (in Eqs. 4.4 and 4.5, respectively) may be related according to the following convolution equation [150],

$$\rho^{v}_{B,q}(X) = \int dX^{'} g(X^{'} - X)\rho^{v}_{B,cl}(X^{'}), \tag{4.6}$$

where the quantum dispersion function, $g(X)$, is given by

$$g(X) = \prod_{j=1}^{N_v} \frac{\beta_v \omega_{j,v}}{2\pi(u''_{j,v}-1)} \exp\left[-\frac{\beta_v}{u''_{j,v}-1}\left(\frac{P^2_{j,v}}{2}+\frac{\omega^2_{j,v}R^2_{j,v}}{2}\right)\right], \tag{4.7}$$

with $u''_{j,v} = u_{j,v}\coth u_{j,v}$ and $u_{j,v} = \beta_v\hbar\omega_{j,v}/2$. From this expression, one sees that the classical distribution is broadened by g to generate the quantum distribution. This is illustrated in Fig. 4.1, where we show representative classical and quantum distributions for a single harmonic oscillator from 60 K to 360 K. At 60 K, 120 K, and 240 K, we see that the classical distributions are markedly narrower than their corresponding quantum ones, i.e., the classical positions and momenta span a smaller range of values. At 360 K, the distributions are more similar, as expected at high temperatures, but non-negligible differences in their widths still exist. It should be noted that, over the temperature range considered, the quantum distribution changes less than the classical one. As will be shown later, these differences in the distributions significantly impact the heat transport dynamics of the NESB model.

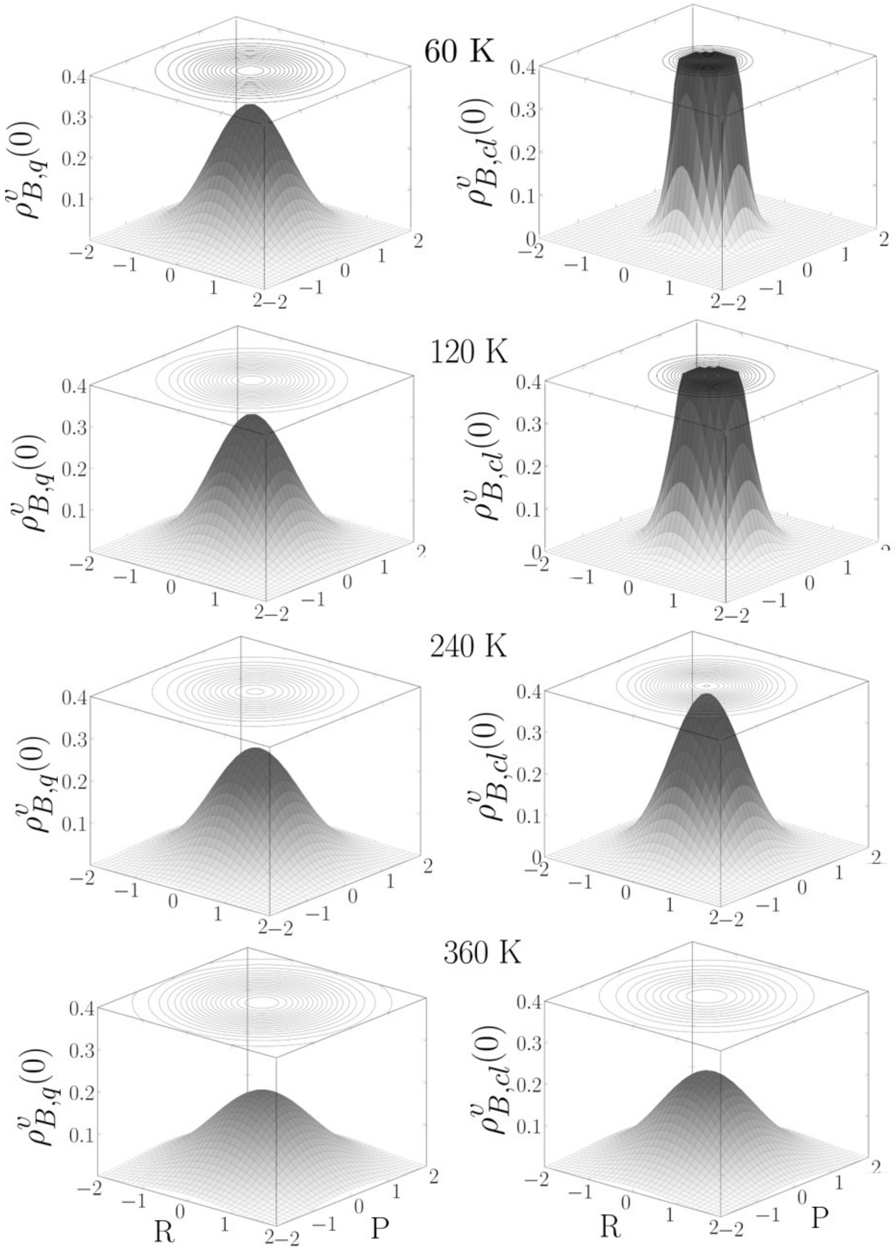

Figure 4.1: Representative quantum (left panels) and classical (right panels) initial probability distributions for one harmonic oscillator from 60 K to 360 K, obtained with Eqs. 4.4 and 4.5, respectively. The value of ω was set to 1 in both cases.

4.3 Simulation details

Given the previous success in applying the DECIDE method to the NESB model [51], we use it herein to simulate the dynamics of the time-dependent heat. The DECIDE method evolves the spin and bath coordinates using different approximations to the quantum-classical Liouville equation [80, 123–125]. The details of the DECIDE equations of motion and their solution for the NESB model are given in Ref. [51]. Based on Eq. 3.1, the heat transferred from the vth bath to the subsystem is obtained by calculating the matrix elements of the time-dependent bath coordinates using DECIDE and performing an average over an ensemble of trajectories [whose bath initial conditions are sampled either from $\rho^v_{B,q}(\boldsymbol{X}(0))$ in Eq. 4.4 or $\rho^v_{B,cl}(\boldsymbol{X}(0))$ in Eq. 4.5] according to

$$\begin{aligned}\langle Q_v(t)\rangle &= \int d\boldsymbol{X}(0)\rho^v_B(\boldsymbol{X}(0))\sum_{j=1}^{N_v}\left[\frac{(P^2_{j,v}(t))^{++}-P^2_{j,v}(0)}{2}\right.\\ &\left.+\omega^2_{j,v}\frac{(R^2_{j,v}(t))^{++}-R^2_{j,v}(0)}{2}\right],\end{aligned}\tag{4.8}$$

where $\rho^v_B(\boldsymbol{X}(0)) = \rho^v_{B,q}(\boldsymbol{X}(0))$ or $\rho^v_{B,cl}(\boldsymbol{X}(0))$, and $\left(P^2_{j,v}(t)\right)^{\alpha\alpha'} = \sum_\beta P^{\alpha\beta}_{j,v}(t)P^{\beta\alpha'}_{j,v}(t)$, for example. In the above equation, we have used the subsystem basis consisting of the eigenstates of $\hat{\sigma}_z$, i.e., $\{|\alpha/\beta\rangle\} = \{|+\rangle, |-\rangle\}$. According to DECIDE [85], the time dependence of the matrix elements $R^{++}_{j,v}(t)$ and $P^{++}_{j,v}(t)$ is obtained by integrating a set of $L^2(L^2-1+2N)$ (where L is the dimensionality of the spin subsystem and N is the total number of bath oscillators) coupled first-order differential equations for the matrix elements of the spin and bath coordinates, viz., with $L = 2$ and $N = N_L + N_R$, the

$4 \times [3 + 2(N_L + N_R)]$ equations are [51]:

$$
\begin{aligned}
\dot{\sigma}_x^{\alpha\alpha'}(t) &= -\frac{1}{\hbar}\sum_v \sum_{j=1}^{N_v} C_{j,v}[R_{j,v}(t)\hat{\sigma}_y(t) + \hat{\sigma}_y(t)R_{j,v}(t)]^{\alpha\alpha'}, \\
\dot{\sigma}_y^{\alpha\alpha'}(t) &= -2\Delta\sigma_z^{\alpha\alpha'}(t) + \frac{1}{\hbar}\sum_v \sum_{j=1}^{N_v} C_{j,v}[R_{j,v}(t)\hat{\sigma}_x(t) \\
&\quad + \hat{\sigma}_x(t)R_{j,v}(t)]^{\alpha\alpha'}, \\
\dot{\sigma}_z^{\alpha\alpha'}(t) &= 2\Delta\sigma_y^{\alpha\alpha'}(t), \\
\dot{R}_{j,v}^{\alpha\alpha'}(t) &= P_{j,v}^{\alpha\alpha'}(t), \\
\dot{P}_{j,v}^{\alpha\alpha'}(t) &= -\omega_{j,v}^2 R_{j,v}^{\alpha\alpha'}(t) - C_{j,v}\sigma_z^{\alpha\alpha'}(t). \qquad (4.9)
\end{aligned}
$$

The time-dependent heat current of the vth bath, $\langle J_v(t)\rangle$, is then calculated according to Eq. 4.2. Converged results are obtained with ensembles of 10^7 trajectories, $N_L = N_R = 100$, and $\omega_{m,L} = \omega_{m,R} = 2000$ cm^{-1}. A time step of Δt = 0.265 fs is used for integrating the equations of motion.

To calculate the steady-state heat current, J, we average all the values of $J(t)$ for $t > t^*$, where t^* is the time after which $J(t)$ remains essentially constant (based on our results, we chose $t^* = 250$ fs). To calculate the error bars in the steady-state heat current, we group the time-dependent heat current values for $t > t^*$ into time-ordered sets of width 20 fs, then calculate the average heat current for each group, and finally calculate the standard deviation of the group averages.

4.4 Results and discussion

In Fig. 4.2, we show the time-dependent heats and heat currents of the left and right baths, calculated using classical and quantum bath sampling (the results of these sampling methods will be referred to as "classical" and "quantum", respectively, from hereon), for the parameter set $T_L = 60$ K, $T_R = 120$ K, $\omega_c = 400$ cm^{-1}, $E_r = 400$ cm^{-1}, and $\Delta = 300$ cm^{-1}. As can be seen in the top panel of Fig. 4.2, the classical time-dependent heats of the left and right baths are larger by ≈ 200 cm^{-1} than their corresponding quantum ones, after the initial transient period. This difference can be attributed to a combination of two related factors. Firstly, the additional average over the quantum dispersion of the bath position and momentum variables (see Eq. 4.6) leads to a reduction in the quantum heats compared to the classical ones. Secondly, the differences in the widths of the left and right bath distributions in the quantum and classical cases creates different effective thermal gradients. More specifically, the more dissimilar widths of the classical left and right bath distributions (see Fig. 4.3) leads to higher heat transfer. In the middle panel of Fig. 4.2, we see that the quantum and classical time-dependent heat currents of the left and right baths exhibit the same oscillatory behaviour, but the magnitudes of the fluctuations are different, viz., the classical result has larger steady-state fluctuations than the quantum one (see inset). This difference can be attributed to the additional averaging over the quantum dispersion function (see Eq. 4.6) in the quantum case, which dampens the fluctuations. To reduce the magnitude of the statistical fluctuations in the left/right bath heat currents at steady state, we next calculated the average time-dependent heat current, $J(t) = \frac{1}{2}\left[\langle J_L(t)\rangle - \langle J_R(t)\rangle\right]$. As can be seen in the bottom panel of Fig. 4.2, both the quantum and classical results are positive and have smaller fluctuations than their respective left/right bath heat currents, with the classical result being larger and having smaller fluctuations than the quantum one. The observation that the classical steady-state heat current is larger than the quantum one is consistent with the larger slopes observed in the classical heat curves and is a consequence of the narrower and more dissimilar classical distributions of the left and right baths compared to their quantum counterparts. Interestingly, despite the larger steady-state fluctuations in the classical left/right bath heat current, we see that it is possible for the averaging process to reduce their magnitude beyond that of the quantum result.

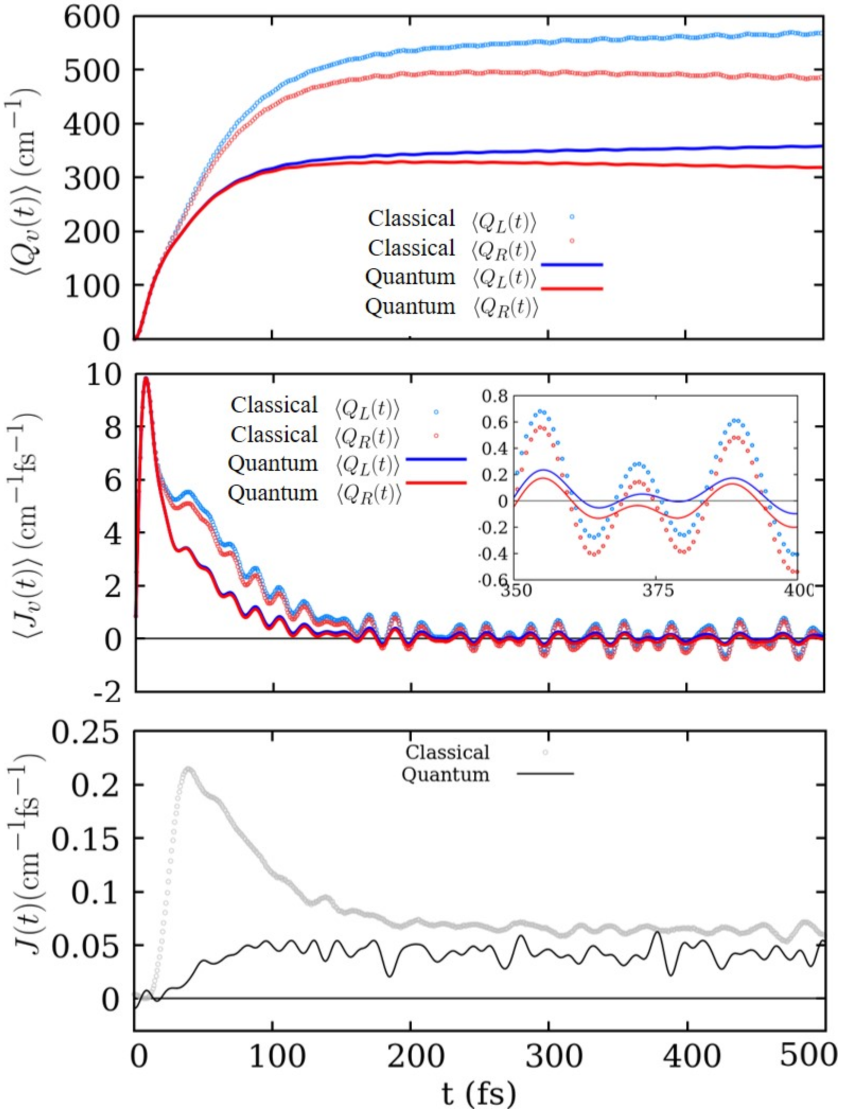

Figure 4.2: Quantum and classical time-dependent heats of the left and right baths (top panel), their corresponding heat currents (middle panel), and the average of the absolute values of the left and right bath heat currents (bottom panel). The results were obtained using the DECIDE method with 10^7 trajectories. The following parameter set was used: $T_L = 60$ K and $T_R = 120$ K, $\omega_c = 400$ cm^{-1}, $E_r = 400$ cm^{-1}, $\Delta = 300$ cm^{-1}.

In Fig. 4.3, we plot the classical and quantum steady state heat currents as a function of the bath reorganization energy (i.e., a measure of the spin-bath coupling strength) for different values of T_L and T_R with $T_R - T_L = 60$ K. The values of the remaining parameters are $\omega_c = 400$ cm^{-1} and $\Delta = 300$ cm^{-1}. As a reference, we also show the numerically exact results (obtained with the ML-MCTDH approach) available for the temperatures $T_L =$ 60 K and $T_R = 120$ K [41]. For the most part, the quantum and classical steady state heat currents exhibit substantial differences across the considered ranges of reorganization energies (viz., 50 cm^{-1} $< E_r <$ 400 cm^{-1}) and temperatures (viz., 60 K$< T_L <$ 360 K and 120 K$< T_R <$ 420 K), with the differences decreasing with increasing temperature and decreasing coupling strength, as expected. In all cases, the classical steady-state heat currents are larger than the quantum ones for the reason discussed earlier. As the bath temperatures are increased, the maximum steady-state heat current (observed in each panel) decreases monotonically in the classical case and increases to a plateau in the quantum case. In both cases, the expected turnover behaviour [128, 129] is captured, with the turnover taking place over approximately the same range of E_r values; however, the slopes of the rise and fall in the classical case are larger than in the quantum case. For example, for the lowest temperature pair, the ratios of the slopes (classical/quantum) are ∼3.5 and ∼18 for the rise and fall, respectively; for the highest temperature pair, the ratios decrease to ∼1.6 and ∼3.3 for rise and fall, respectively.

In Fig. 4.4, we present the steady-state heat current as a function of the temperature gap, $\Delta T = T_R - T_L$, between the heat baths, for three fixed values of the left-bath temperature, viz., $T_L = 120$ K, $T_L = 240$ K, and $T_L = 360$ K. The values of the remaining parameters are $\omega_c = 400$ cm^{-1}, $E_r = 100$ cm^{-1}, and $\Delta = 300$ cm^{-1}. First, as T_L increases for a given value of ΔT, one observes that the classical and quantum steady-state heat currents become increasingly similar, as expected. However, even at relatively high left/right bath

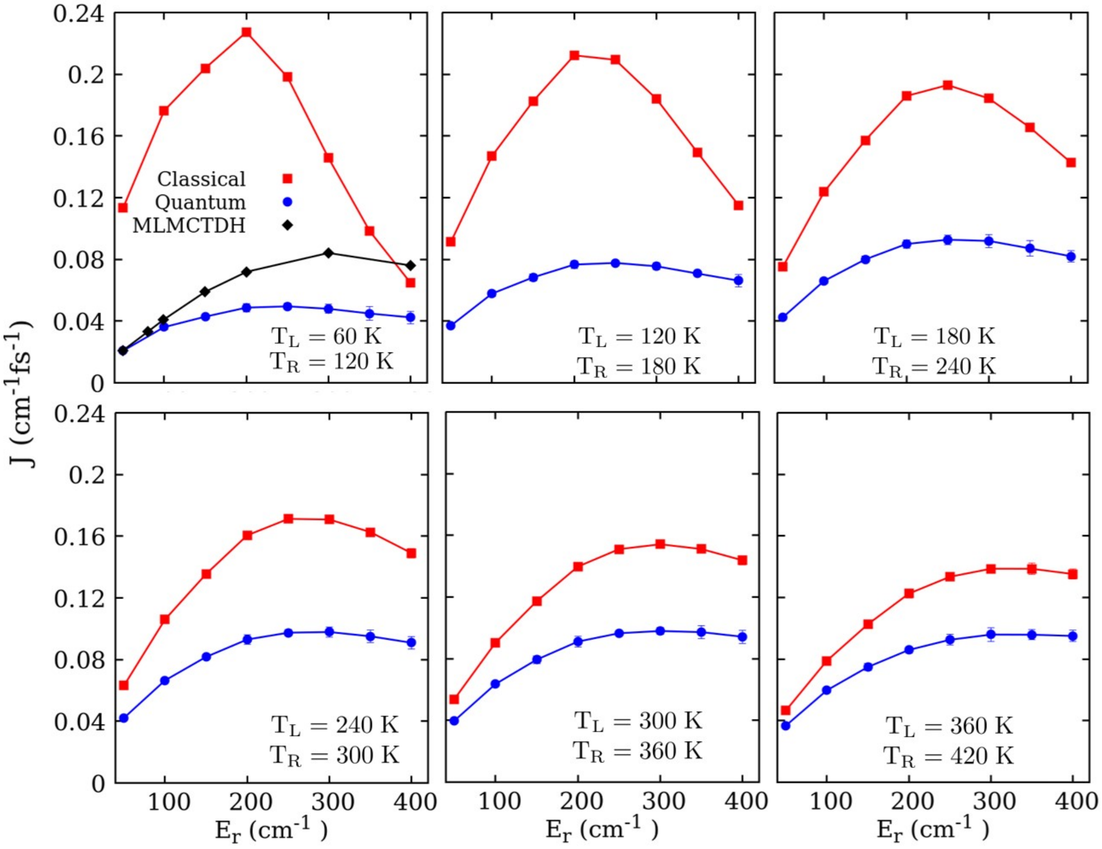

Figure 4.3: Steady-state heat current as a function of the bath reorganization energy, E_r, for different bath temperatures. The results were obtained using the DECIDE method with 10^7 trajectories. In all cases, $\omega_c = 400$ cm^{-1}, $\Delta = 300$ cm^{-1}, and $T_R - T_L = 60$ K. As a reference, numerically exact results are shown for the case of $T_L = 60$ K and $T_R = 120$ K [41].

temperatures (e.g., $T_L = 360$ K and $T_R = 480$ K), there is still a small but significant difference (viz., 0.04 cm^{-1}fs^{-1}) between them. Second, both the classical and quantum steady-state heat currents exhibit an increasing linear trend with increasing ΔT. This is simply due to the fact that the thermodynamic force for heat transfer increases with larger differences between the initial distributions of the left and right baths. Moreover, at small ΔT values, the classical and quantum results are in very close agreement, but as

ΔT increases the difference between them grows monotonically. Finally, as T_L increases, there is an overall decrease in the classical steady-state heat current (across the range of ΔT values), viz., the slope of the linear trend decreases by $\sim 45\%$; on the other hand, the quantum steady state heat current only exhibits a slight overall decrease in going from $T_L = 240$ K to 360 K. This difference underscores the sensitivity of the heat transport calculations to the classical bath sampling.

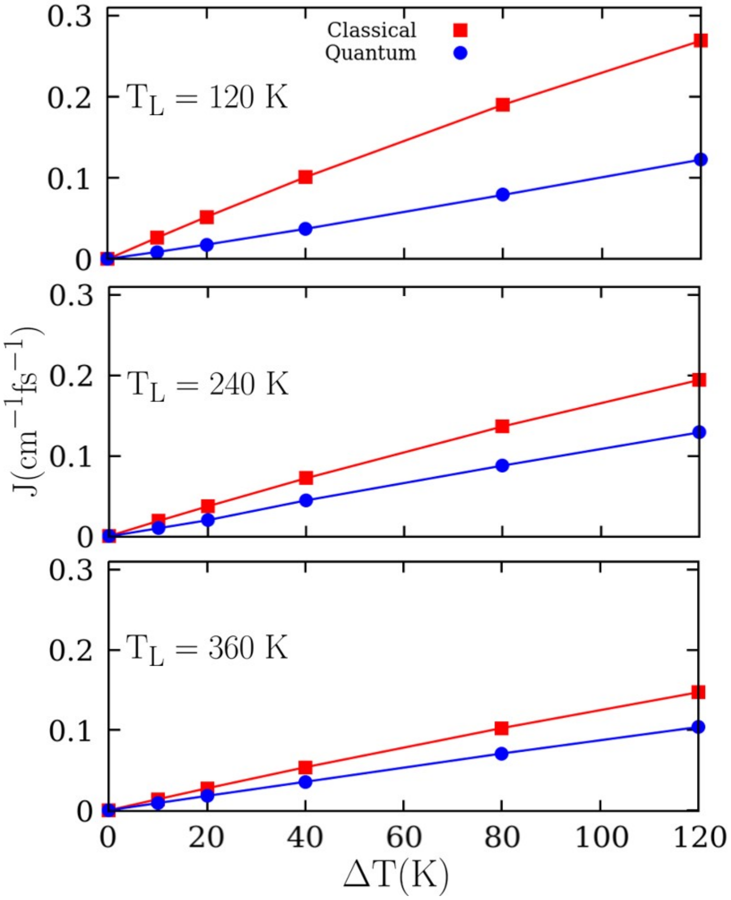

Figure 4.4: Steady-state heat current as a function of the temperature gap between the heat baths. The results were obtained using the DECIDE method with 10^7 trajectories. In all cases, $\omega_c = 400$ cm^{-1}, $E_r = 100$ cm^{-1}, and $\Delta = 300$ cm^{-1}.

In Fig. 4.5, we show the classical and quantum steady-state heat currents as a function of the bath reorganization energy, E_r, for the following cutoff frequencies of the bath spectral density: $\omega_c = 100\ \mathrm{cm}^{-1}, 200\ \mathrm{cm}^{-1}, 400\ \mathrm{cm}^{-1}, 600\ \mathrm{cm}^{-1}$, and $1200\ \mathrm{cm}^{-1}$. The values of the remaining parameters are $\Delta = 300\ \mathrm{cm}^{-1}$, $T_L = 60$ K, and $T_R = 120$ K. As a reference, we also show the numerically exact results (obtained with the ML-MCTDH approach) for the case of $\omega_c = 400\ \mathrm{cm}^{-1}$. (NB: To observe the turnovers in the $\omega_c = 100\ \mathrm{cm}^{-1}$ and $\omega_c = 200\ \mathrm{cm}^{-1}$ cases, see Fig. 4.2 where the steady-state heat currents are plotted over a larger range of bath reorganization energies.) Several notable similarities/differences between the classical and quantum results are observed. First, for all the cutoff frequencies considered, the classical results are higher than the quantum ones across the entire range of E_r values (except for the $\{\omega_c = 1200\ \mathrm{cm}^{-1}, E_r = 400\ \mathrm{cm}^{-1}\}$ case). The overall trend in the classical and quantum results as a function of E_r is similar (apart from a few differences in the turnover points), with the smallest differences between them observed for small E_r values in the case of $\omega_c \leq 200\ \mathrm{cm}^{-1}$ and larger E_r values in the case of $\omega_c \geq 400\ \mathrm{cm}^{-1}$. Second, the differences between the classical and quantum results remain relatively small (over the range of E_r values considered) for $\omega_c = 100\ \mathrm{cm}^{-1}$, but can become relatively large for the remaining ω_c values. Third, as ω_c increases from low values (where the bath is off-resonance with the subsystem) to intermediate values (where the bath is nearly resonant with the subsystem) to high values (where the bath is again off-resonance with the subsystem), we see that the maxima in the classical and quantum steady-state heat currents occur at $\{\omega_c = 400\ \mathrm{cm}^{-1}, E_r = 200\ \mathrm{cm}^{-1}\}$ and $\{\omega_c = 200\ \mathrm{cm}^{-1}, E_r = 500\ \mathrm{cm}^{-1}\}$, respectively. In general, the largest differences between the classical and quantum results occur when $\omega_c \geq 200\ \mathrm{cm}^{-1}$ (i.e., ω_c is close to or exceeds Δ) and E_r takes on intermediate values. In this regime, there are bath modes in resonance with the subsystem and the friction induced by the coupling to the bath is not yet high enough to impede the heat transfer. At low E_r values, the differences between the classical and quantum results are either negligible or relatively small because the bath sampling has a lower impact when the spin-bath coupling is weak. In contrast, the differences observed at high E_r values (when $\omega_c \geq 400$ cm^{-1}) are small because the heat transfer is highly friction-limited, i.e., the heat transfer is saturated to the point that it becomes independent of the initial bath sampling method. Similar results are obtained when the tunneling frequency is varied and ω_c is kept constant (see Fig. 4.4).

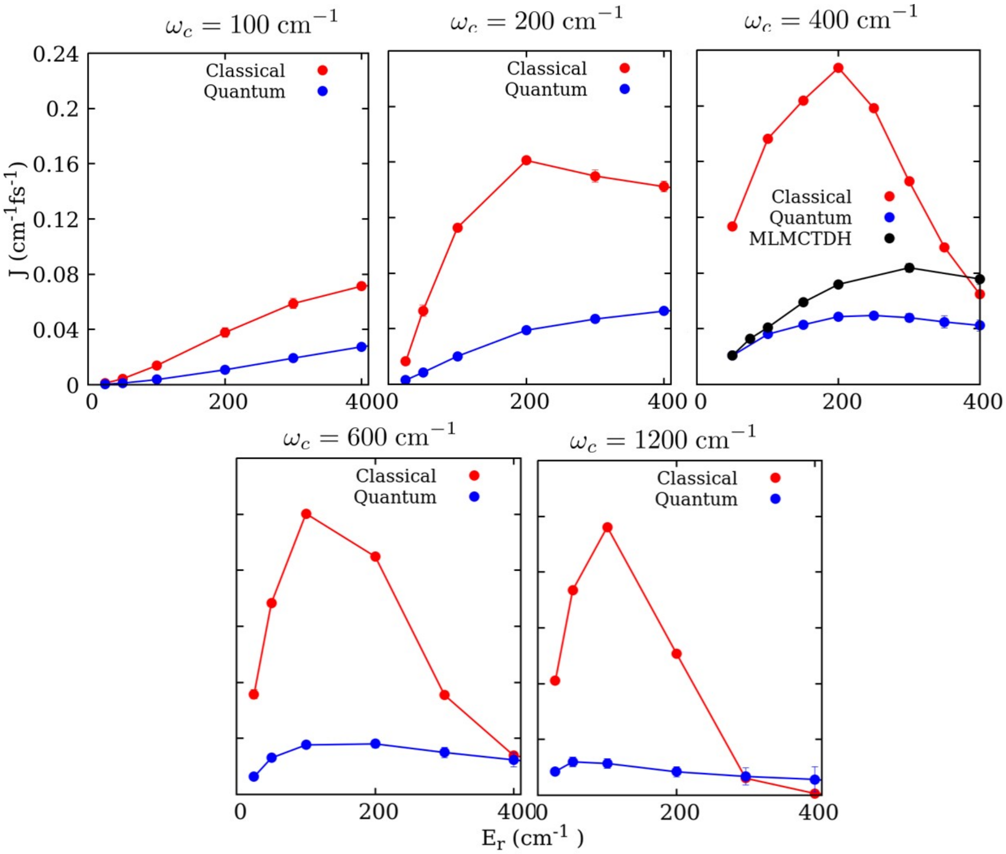

Figure 4.5: Steady-state heat current as a function of the bath reorganization energy, E_r, for different cutoff frequencies, ω_c. The results were obtained using the DECIDE method with 10^7 trajectories. In all cases, $\Delta = 300$ cm^{-1}, $T_L = 60$ K, and $T_R = 120$ K.

Finally, we analyze the fluctuations in the classical and quantum steady-state heat currents in terms of the steady-state fluctuation theorem (SSFT),[151, 152] which provides a rigorous constraint on the heat current fluctuations and generalizes the second law of thermodynamics to the nanoscale. For heat exchange between two baths at equilibrium, the SSFT may be approximately expressed as [153]

$$\lim_{t\to\infty} \frac{1}{t} \ln \frac{P_t(Q(t))}{P_t(-Q(t))} = \frac{\Delta\beta Q}{t}, \tag{4.10}$$

where $\Delta\beta = \beta_L - \beta_R$ and $P_t(Q(t))$ is the probability distribution of the net heat transfer $Q(t)$ from the hot (right) bath to the cold (left) bath by time t. Previously, it was found that the SSFT holds for the NESB model in the Markovian regime [116]. For our analysis, we check the validity of SSFT using a relatively weak coupling strength (viz., $E_r = 100\ \text{cm}^{-1}$), $\Delta = 300\ \text{cm}^{-1} < \omega_c = 400\ \text{cm}^{-1}$, $T_L = 60$ K, and $T_R = 120$ K. In the left panel of Fig. 4.6, we plot the classical and quantum probability distributions, $P_t(Q(t))$, at $t = 500$ fs, generated from ensembles of 10^7 trajectories. As can be seen, the width of $P_t(Q(t))$ is larger when the initial bath coordinates for each trajectory are sampled from the quantum bath distribution, compared to the classical case. This appears to be a result of the fact that the quantum bath distribution is broader than the classical one (see Eqs. 4.6 and 4.7). In the right panel of Fig. 4.6, we plot $\ln[P_t(Q(t))/P_t(-Q(t))]$ vs. $Q(t)$ at $t = 500$ fs, generated by both classical and quantum bath sampling, and compare the results to $\Delta\beta Q$ vs. Q. As can be seen, the quantum result is linear and shows a maximum absolute deviation of 0.06 from $\Delta\beta Q$, while the classical result is nonlinear and deviates greatly from $\Delta\beta Q$ (viz., 0.74 at $400\ \text{cm}^{-1}$). In particular, the classical result is higher than the quantum one, meaning that there is a relatively larger disparity between the probability of a net heat transfer of Q from the hot bath to the cold bath [i.e., $P_t(Q(t))$] and that from the cold bath to the hot bath [i.e., $P_t(-Q(t))$]. Thus, at least for the parameter set considered, we find that quantum bath sampling is required to ensure the validity of the SSFT.

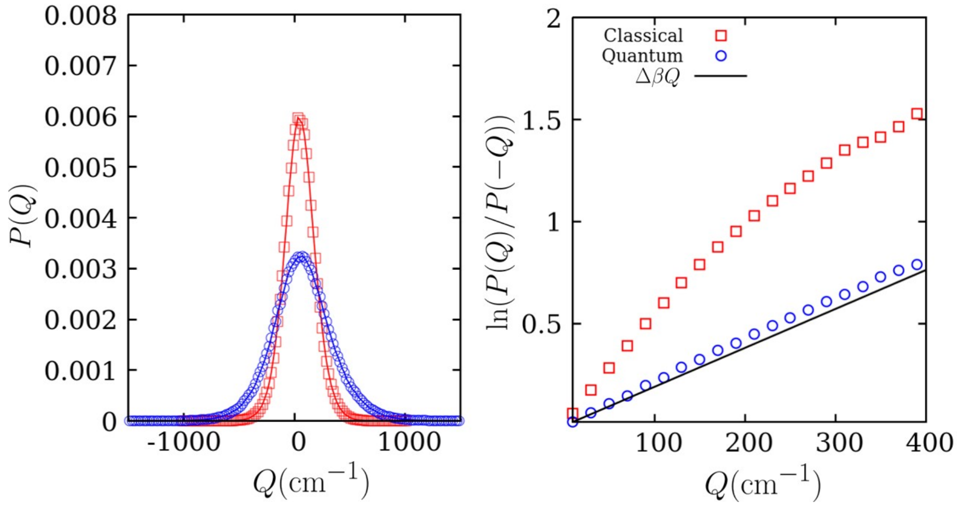

Figure 4.6: Plot of the heat transfer probability, $P_t(Q(t))$, at $t = 500$ fs (left panel). Check of the validity of the SSFT based on Eq. 4.10 (right panel). The results were obtained using the DECIDE method with 10^7 trajectories and the following parameter set: $\omega_c = 400$ cm^{-1}, $E_r = 100$ cm^{-1}, $\Delta = 300$ cm^{-1}, $T_L = 60$ K, $T_R = 120$ K.

4.5 Summary

In this work, we studied the effect of quantum bath sampling on the heat transfer dynamics in the NESB model. For this purpose, we sampled the initial positions and momenta of the bath oscillators from both quantum and classical thermal distributions and compared the results for the steady-state heat currents. In general, at a given temperature, the classical distribution is narrower than the quantum one. Moreover, for the model studied, the differences in the widths of the classical distributions for the hot and cold baths are larger than the corresponding quantum ones over a wide range of temperatures. Together, these differences in the initial equilibrium structures led to pronounced differences in the magnitudes of the steady-state heat current and, to a lesser extent, trends as a function of the various model parameters. In particular, the classical steady-state heat currents were observed to be $\sim 1.3 - 4.5$ times higher for a broad range of parameter regimes considered.

A sharper turn-over in the steady-state heat current (as a function of subsystem-bath coupling) was observed in the classical case, with the turn-over point sometimes occurring at lower values of the coupling than in the quantum case. Finally, we found that the SSFT holds in the Markovian regime only when quantum bath sampling is used. Together, these findings underscore the importance of performing quantum sampling of the bath coordinates across a wide range of bath temperatures, reorganization energies, and cutoff frequencies for calculations of time-dependent and steady-state heat currents in thermal molecular junctions. Our study also sheds light on the possibility of optimizing the steady-state heat current by engineering the initial equilibrium structures of the thermal baths.

Chapter 5

Ultrafast Topologically-protected Vibrational Energy Transfer in a Dimer Chain

5.1 Introduction

Molecular material-based technologies have attracted the attention of various research communities due to their many appealing factors such as production cost, chemical versatility, and environmental friendliness. Organic material-based optoelectronics[154, 155] such as light-emitting diodes and photovoltaics, molecular electronics devices [156] such as molecular wires, and quantum computing architectures[157–159] for encoding quantum information into molecules are a few prominent examples. Underlying this wide array of technologies is the common challenge of engineering the highly efficient transfer of energy [160, 161], charge [162, 163], or quantum information [158, 159] across complex molecular structures. For instance, the excitonic research community has been studying ultrafast excitonic dynamics in natural light harvesting complexes [164] in order to understand how energy transfers so efficiently through the highly disordered energy landscapes commonly encountered in biological settings[165–167]. The knowledge acquired from these studies has already led to the design of optoelectronics devices[168–170]. Similarly, studies of quantum transport through molecular junctions and quantum state transfer (i.e., quantum information transfer) mediated by vibrons [158, 159] have also been carried out in order to improve the functionality of molecular electronics and molecule-based quantum computers, respectively.

In this chapter, we focus on excitation energy transfer in molecular systems. Recently, Yuen-Zhou et al. [171] proposed to use topologically protected edge states [172, 173] as efficient transport channels to direct Frenkel exciton migration in highly disordered molecular systems for energy harvesting applications. The symmetry-protected topological constraint increases the transport efficiency by greatly suppressing the possibility of disorder-induced backscattering. However, this proposal requires the application of an external magnetic field and advanced structural engineering to realize the desired topological phases for the excitons. This motivated us to search for a simpler way (in terms of experimental considerations) to realize topologically-protected excitation energy transfer in molecular systems, which could be eventually adopted in actual devices.

Different from the strategy adopted in Ref. [171], we seek to generate topologically protected edge states in molecular assemblies through minimal modifications. To this end, we focus on quasi one-dimensional assemblies, for which a harmonic description of the vibrations is adequate [131], as the basis for our investigation. For example, recent theoretical studies have suggested the possibility of ultrafast long-range vibrational energy transfer [174] and electric-field induced topological phases [175] in α-helical and double-stranded helical structures. Such results, coupled with continuing advances in organic materials synthesis, indicate that simple quasi one-dimensional organic structures may serve as potential platforms for ultrafast topologically-protected excitation energy transfer.

In this work, we investigate energy transfer along one-dimensional molecular chains with dimerized units, and explain how the transfer could primarily be mediated via topologically protected edge modes[73, 173]. Our dynamical simulations reveal that long-range vibrational energy transfer takes place across a wide range of parameter regimes for the model considered. In particular, the integrity of the long-range transfer is not compromised by coupling to the phonons arising from displacements along the backbone of the chain. In fact, the rate of the long-range energy transfer is enhanced by three orders of magnitude due to this coupling.

To carry out our dynamical simulations, we adopt the well-established quantum-classical Liouville equation (QCLE) formalism [83, 176, 177]. In mixed quantum-classical methods, the total system is partitioned into a quantum subsystem and a classical environment in order to reduce computational costs. For the model considered in this work, the high-frequency excitations on the dimer chain are treated quantum mechanically, while the low-frequency lattice displacements of the chain are treated classically. It should be noted that the QCLE yields *exact* quantum dynamics for a subset of models (including the one studied in this work) in which the environment is composed of harmonic oscillators that are bilinearly coupled to each other and linearly coupled (with respect to the environment's coordinates) to a finite set of quantum subsystem degrees of freedom (DOF). Hence, the QCLE approach is expected to provide highly reliable predictions of quantum phenomena associated with all the topological phases in our model. However, to reduce computational costs and focus on qualitative trends, we employ an adiabatic approximation to the solution of the QCLE, which restricts the evolution of the classical DOF to the potential energy surfaces (PESs) that they are initialized on. Although nonadiabatic effects could be non-negligible for this model, we found previously that the adiabatic approximation allows for a very good qualitative (if not semi-quantitative) description of the dynamics for a closely related model with similar parameters to that considered in this work.[70]

The outline of this chapter is as follows: In Sec. 5.2, we describe the model of a dimerized chain coupled to acoustic phonons. In Sec. 5.3, we provide the details of how our simulations are performed. In Sec. 5.4, we present our simulation results, which demonstrate the robustness and ultrafast nature of the long-range energy transfer mediated by the coupling to the phonon environment. Finally, the conclusions of this study are given in Sec. 5.5.

5.2 Dimerized chain coupled to acoustic phonons

We study the energy transfer along a one-dimensional dimerized chain of quantized (high-frequency) modes coupled to a set of acoustic phonons corresponding to the (low-frequency) lattice displacements of the chain (see Fig. 6.1 for a schematic representation). Since we are concerned with the quantum dynamics of this system in the high-temperature limit, the acoustic phonons can be adequately modelled as classical vibrations.

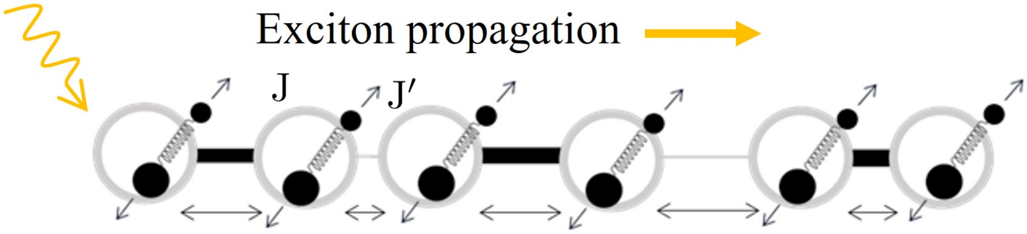

Figure 5.1: Schematic representation of the dimerized chain (with $N = 6$) coupled to acoustic phonons generated by lattice vibrations (denoted by double-headed arrows).

The Hamiltonian of this dimerized chain of quantized modes coupled to a set of classical acoustic phonons (chosen to be the normal modes of a chain of bilinearly coupled harmonic oscillators) is given by

$$H = H_q + \sum_{m=1}^{N} H_{mm}(R) \left|\phi_m\right\rangle \left\langle\phi_m\right| , \tag{5.1}$$

where H_0 found in H_q (see Eq. (1.6)) now takes the following form

$$H_0 = \sum_m \frac{P_m^2}{2M} + \sum_m \left[E_{m0} + (1-\delta_{m,1})\frac{W}{2}(R_m - R_{m-1})^2 + w_{m0}(R) \right], \tag{5.2}$$

and $H_{mm}(R) = w_{m1}(R) - w_{m0}(R)$. The coupling term $w_{m\nu}(R)$ is given by

$$w_{m\nu}(R) = (1-\delta_{m,1})\frac{\chi}{2}(R_m - R_{m-1})\langle \chi_{m\nu}|q_m^2|\chi_{m\nu}\rangle. \tag{5.3}$$

In the above equations, each harmonic oscillator is described by a position R_m, momentum P_m, and force constant W, $\delta_{m,1}$ is the Kronecker delta function, and a uniform coupling strength χ is adopted.

The matrix elements of $q_m q_{m-1}$ in Eq. 5.1 are all given by

$$\langle \phi_m|q_m q_{m-1}|\phi_{m-1}\rangle = \langle \chi_0|q|\chi_1\rangle^2. \tag{5.4}$$

The values of the various matrix elements of q_m and q_m^2 are taken from Table 2 in Ref. [69], while the values of the parameters $E_{m1} - E_{m0}$, J, W, and M are taken from Table 1 in Ref. [69] and are given by 1660 cm^{-1}, 7.8 cm^{-1}, 13 N/m, and 87 m_p, respectively. The values of χ considered in this study are 5, 25, and 62 pN.

Simply looking at the Hamiltonian in Eq. 5.1, it is not evident whether the non-trivial topological phases can be preserved once the classical acoustic phonons are coupled to the dimerized quantum chain. One important observation is that the classical DOF provide an effective on-site potential that modifies the diagonal matrix elements of the Hamiltonian. In principle, the sublattice symmetry is broken and the topological phases could change. A major focus of our study is to investigate the robustness of the topological edge states upon coupling to the vibrational DOF. A high robustness is crucial for long-range energy transfer via these edge modes in practical applications.

5.3 Simulation details

In all of our simulations, the quantum subsystem of high-frequency oscillators and classical environment of low-frequency lattice displacements are assumed to be uncorrelated initially, yielding a factorized initial density operator:

$$\hat{\rho}\left(0\right) = \hat{\rho}_q\left(0\right)\rho_e\left(X\right), \tag{5.5}$$

where $\hat{\rho}_q(0)$ and $\rho_e(X)$ are the initial densities of the quantum subsystem and classical environment, respectively. Because we are interested in the population dynamics following a vibrational excitation of the first quantized mode in the chain, the initial density matrix of the quantum subsystem (represented in the subsystem basis of singly excited states) is given by

$$\hat{\rho}_q(0) = \begin{pmatrix} 1 & 0 & \cdots & 0 \\ 0 & 0 & \cdots & 0 \\ \vdots & \vdots & \ddots & 0 \\ 0 & 0 & \cdots & 0 \end{pmatrix}. \tag{5.6}$$

Since our simulations are performed in the adiabatic basis, the initial state of the quantum subsystem is sampled for each trajectory by first expressing $\hat{\rho}_q(0)$ in the adiabatic basis (see details of the transformation and sampling in Appendix A of Ref. [70]). A set of initial values for the positions/momenta of the classical oscillators for each trajectory is obtained by sampling from a Boltzmann distribution corresponding to a collection of uncoupled harmonic oscillators at thermal equilibrium at 300 K:

$$\rho_e(X) \approx \frac{1}{Z}\prod_{j=1}^{N} \exp\left[-\beta\left\{\frac{P_j^2}{2} + \frac{1}{2}W^2R_j^2\right\}\right], \tag{5.7}$$

where $Z = \int dRdP \exp\left[-\frac{\beta}{2}\sum_j(P_j^2 + W^2R_j^2)\right]$ is the partition function. Starting from these initial values, the correct thermal equilibrium distribution at 300 K (in the absence of a vibrational excitation) is achieved by equilibrating the coupled harmonic oscillators for 2 ps using the ground-state Hamiltonian found in Eq. 5.2 with a Nosé-Hoover thermostat and a time step of 0.25 fs. (In Ref. [70], we checked the ergodicity of the Nosé-Hoover thermostat by comparing our adiabatic dynamics results to those generated with a Nosé-Hoover chain thermostat and found good quantitative agreement between them.)

Following the sampling of the initial quantum state and positions/momenta of the classical DOF, microcanonical trajectories of length 150 fs are generated using the short-time sequential propagation algorithm[84] in the absence of nonadiabatic transitions (i.e., adiabatic dynamics), with a time step of 1 fs. To correct for the majority of arbitrary sign flips in the eigenvectors upon numerical diagonalization of the Hamiltonian matrix at each time step of a trajectory, we use the sign-correction procedure outlined in Ref. [70]. (N.B.: This procedure not only corrects eigenvector signs within a trajectory, but also establishes sign consistency across an ensemble of trajectories.) Finally, the time-dependent populations of the high-frequency modes along the chain are calculated based on an ensemble of 10^7 trajectories according to Eq. 2.15 with $\hat{A} = |\phi_m\rangle\langle\phi_m|$.

5.4 Results and discussion

We first demonstrate through a series of numerical simulations that the chosen model can indeed facilitate long-range population transfer (LRPT) via the topological edge modes, even in the presence of lattice distortions. Importantly, the LRPT proceeds at a much faster rate in the presence of the phonons.

To isolate the effect of coupling the dimerized quantum chain to the phonons on the LRPT, we begin by considering a static dimer chain. As briefly summarized in Sec. 1.4, the topological edge states can only arise in a perfect dimer chain with an even number of quantum oscillators and the hopping parameters satisfying the relation $H > H_c$. In Figs. 1 and 2a, we present results that confirm that the onset of LRPT can be controlled by modifying the parameter H for a dimerized quantum chain composed of six high-frequency oscillators. With the understanding that we only consider the single-excitation manifold of the dimerized quantum chain, we will refer to the high-frequency quantum oscillators as sites in the following discussion.

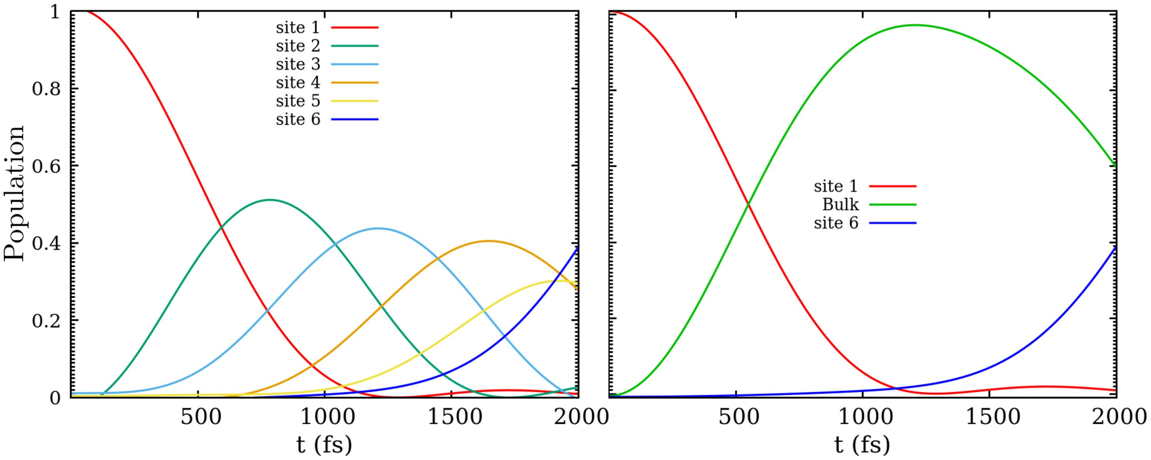

Figure 5.2: Population dynamics for a six-site static dimer chain with $H = 1$, i.e., $J = J'$. (a) Population on each site. (b) Population on boundary sites and in bulk.

Figure 5.2 shows the singly excited state populations plotted versus time for the static dimer chain when $H = 1$. In the left panel, it is clearly shown that a wave packet (initially on site 1) spreads across the chain by sequentially exciting the next oscillator in the 1D chain. In the right panel, we adopt an alternative representation of the dynamics by summing the populations on the interior sites (in this case, sites 2 through 5) and designating this sum as the bulk contribution. (N.B.: In the subsequent plots, we solely use this representation.) The right panel conveys the same message that the excitation has to propagate through the bulk of the chain before reaching the other end. This picture of sequential population transfer is precisely what one expects from quantum dynamics in a 1D chain, viz., the ballistic propagation commonly observed in perfect 1D chains without any static or dynamic sources of disorder.

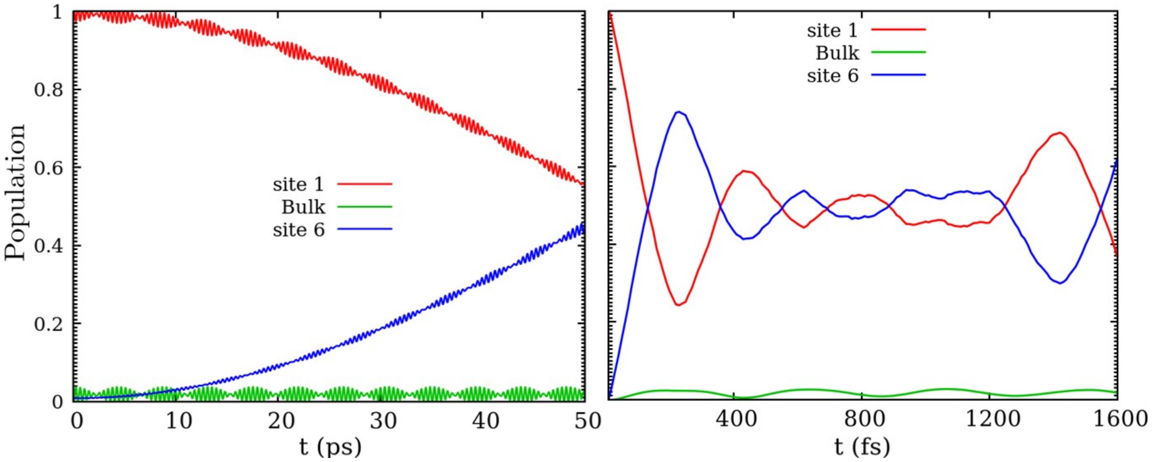

Figure 5.3: Population dynamics for a six-site dimer chain with $H = 10$. (a) Static dimer chain. (b) Dimer chain coupled to acoustic phonons with $\chi = 5$ pN.

We next consider a six-site dimer chain with $H = 10$. In the left panel of Fig. 5.3, we see that the wave packet directly transfers from one end to the other, effectively skipping over the bulk sites, on a timescale of tens of picoseconds. This transfer mechanism is a signature of the presence of topological edge states. As mentioned in Sec. 1.4, the edge states are not strictly confined to the ends of a finite-sized dimer chain, but become increasingly confined as the chain length increases. Thus, it is encouraging to observe that such a direct LRPT is also possible in short chains. In the case of longer dimer chains, the critical parameter H_c becomes smaller, implying that one could achieve a similar quality of LRPT without requiring such a large value of H (as in the present example of a six-site dimer chain). To rationalize the slow timescale of the LRPT, we recall that the idealized LRPT rate is characterized by the energy gap between the two edge states (i.e., 2Δ) in the effective two-level model presented in Sec. 1.4. In the topologically non-trivial phase, the two edge states become nearly degenerate and, therefore, the LRPT will be slow.

From this point onward, we consider the dimerized quantum chain coupled to the lattice displacements. The population dynamics in a six-site chain with $\chi = 5$ pN is shown in the right panel of Fig. 5.3. In comparison to the left panel, the LRPT now proceeds three orders of magnitude faster (from ~ 50 ps down to ~ 100 fs). More surprisingly, the coupling to the acoustic phonons (arising from the lattice displacements) does not compromise the robustness of the LRPT in this case. However, it is expected that, as the interaction between the dimer chain and the acoustic phonons increases, the once isolated manifold of edge states will mix with the eigenstates predominantly confined to the bulk. This is due to the fact that these states are coupled to the same set of lattice vibrations.

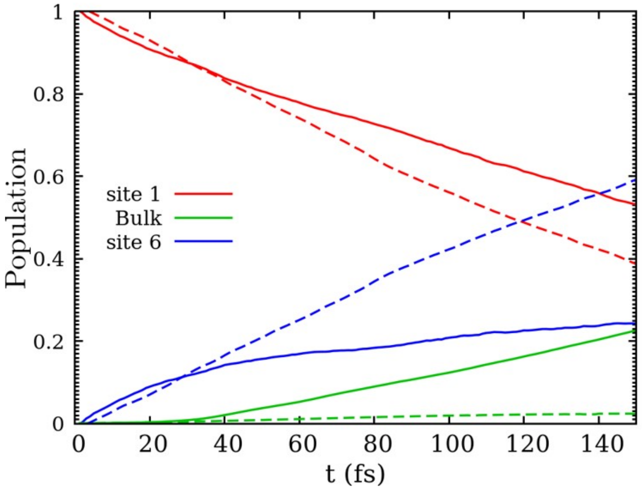

Figure 5.4: Population dynamics for a six-site dimer chain ($\chi = 25$ pN and $H = 10$) with static disorder in the excited state energies of each site. The solid and dashed lines refer to the results with and without disorder, respectively.

It is not uncommon for a natural or fabricated chain to have a structure that deviates from an idealized structure with identical units characterized by uniform parameters. Thus, we now investigate the robustness of LRPT against inhomogeneity in the quantum oscillators across the chain. This inhomogeneity is introduced into our simulations through a statistical variation of the energies of the quantum oscillators' first excited states. More specifically, we sample independent values of energy fluctuations from a Gaussian distribution (whose standard deviation is taken to be 15% of the inter-dimer hopping parameter J') and add them to each E_{m1} at the beginning of each trajectory. As such a static inhomogeneity breaks the sublattice symmetry, the topological edge states are expected to lose their desired spatial profile of being predominantly localized on the two boundary sites. Indeed, Fig. 5.4 shows that, in the presence of static disorder (solid lines), more population leaks into the bulk of the chain than in the absence of static disorder (dashed lines). Nevertheless, as seen, the LRPT is partially preserved in the presence of the weak disorder, i.e., when J' is much larger than the fluctuations of E_{m1}. It should be noted that these results were generated with a larger value of the coupling between the quantum and classical subsystems, viz., $\chi = 25$ pN. While a stronger coupling is expected to compromise the integrity of the topological edge states (by amplifying the dynamical noise due to the interaction with the classical phonons), we find them to be remarkably stable in the absence of the disorder for this value of the coupling.

We next investigate the effect of increasing the coupling strength between the quantum and classical subsystems from $\chi = 5$ pN to $\chi = 62$ pN in the six-site dimer chain for different values of H in greater detail. According to Fig. 5.5, the population leakage into the bulk is significant even when $H = 12$. However, the mechanism of LRPT is preserved even in this strong-coupling limit. For instance, one sees that the population inside the bulk always decreases and the population on the end site always rises faster with increasing H. In the

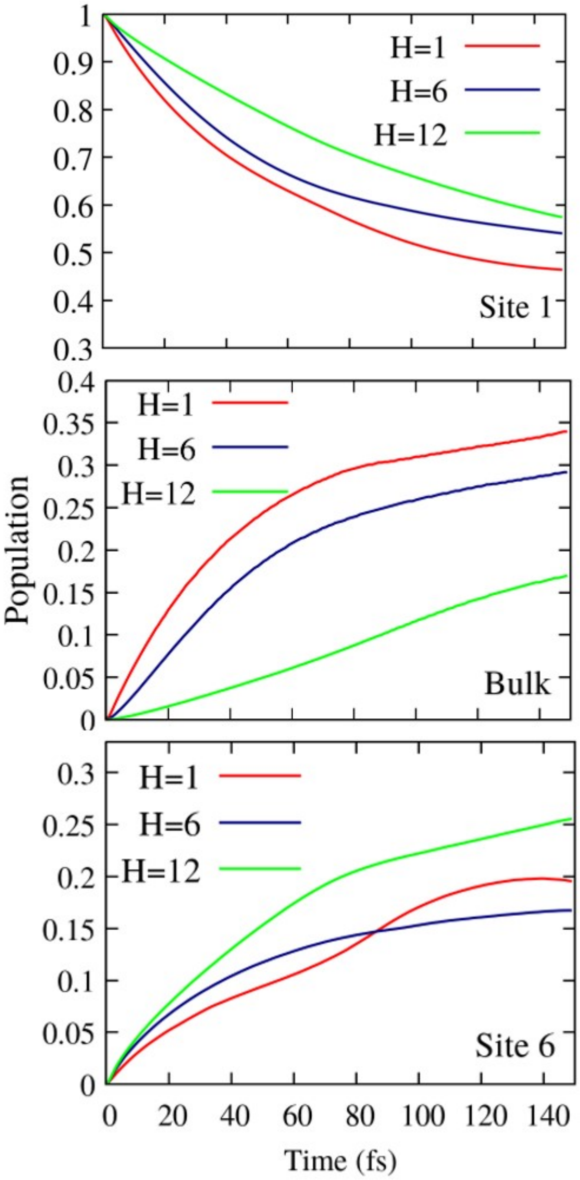

Figure 5.5: Population dynamics for a six-site dimer chain with $\chi = 62$ pN and different values of H. (Left): Site-1 population. (Center): Bulk population. (Right): Site-6 population.

subsequent simulations, we use this stronger coupling to investigate the robustness of the LRPT under various conditions.

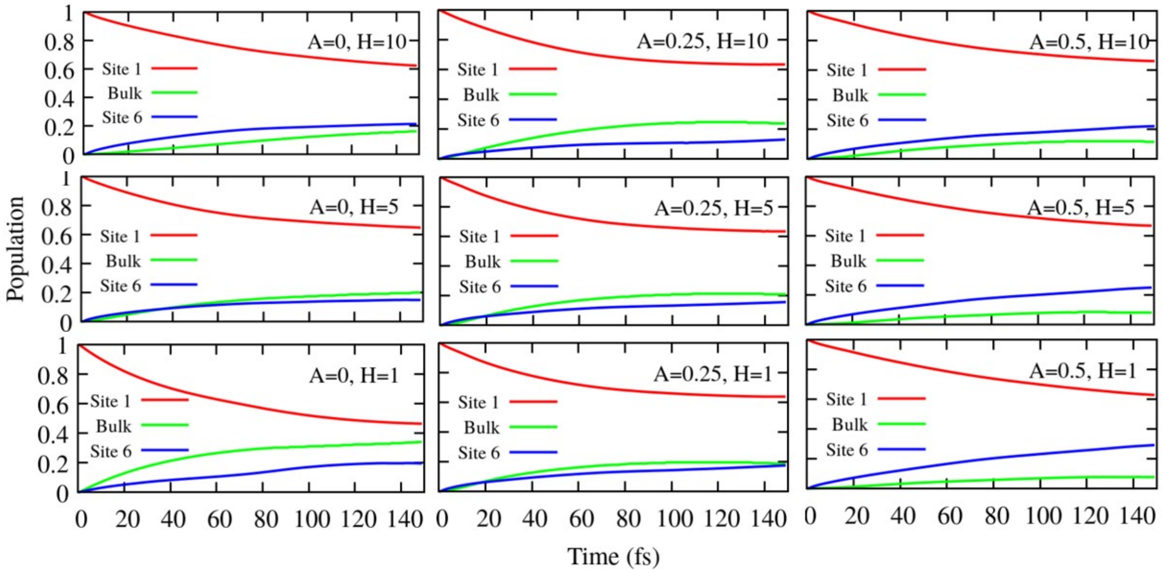

Figure 5.6: Population dynamics for a six-site dimer chain with $\chi = 62$ pN and different values of A (in Å) and H.

So far, we have considered LRPT as a quantum dynamical phenomena involving topological edge states that only arises when $H > H_c$, as illustrated in Figs. 5.2 and 5.3. However, there may be alternative mechanisms that generate LRPT even when $H < H_c$. In fact, one of the authors has previously proposed such a mechanism in a 1D chain without dimerization (i.e., $J = J'$). This mechanism emerges when there are lattice distortions at the two ends of the chain, which in turn cause a shift in the vibrational frequencies of the two boundary quantum oscillators. Indeed, there is no issue in designing a system that supports the co-existence of both mechanisms to drive the LRPT, as shown in Fig. 5.6. This figure provides a comprehensive view on how the population dynamics changes as a function of both H and an energy shift ($\frac{\chi}{2}A\langle\chi_{m\nu}|q_m^2|\chi_{m\nu}\rangle$, where A is the length of the distortion) to the two boundary quantum oscillators. Along the vertical axis of Fig. 5.6, H is varied from $H = 1$ (corresponding to the topologically trivial phase) to $H = 10$ (corresponding to the topologically non-trivial phase), while along the horizontal axis, A is varied from

$A = 0$ Å to $A = 0.5$ Å, i.e., shifting the frequencies of the two boundary quantum oscillators out of resonance with those of the interior oscillators. When there is no energy shift, the LRPT is solely driven by the topological edge states (see leftmost column of Fig. 5.6), while as A is increased with $H = 1$ (see bottom row of Fig. 5.6), the alternative mechanism (involving the asymmetric oscillators at the boundaries) solely drives the LRPT. When there is an interplay between the two mechanisms (see remaining panels of Fig. 5.6), we observe two trends: (i) as one increases H for a fixed A, the effectiveness of the LRPT is slightly compromised, and (ii) as one increases A for a fixed H, the effectiveness of the LRPT can be significantly improved.

Another question of interest is the dependence of the LRPT on the length (i.e., number of quantum oscillators, N) of the dimerized quantum chains. As described in Sec. 1.4, the topological edge states are strictly absent in a static (imperfectly) dimerized chain with an odd number of sites, even if $H > H_c$. Thus, we now investigate the population transfer as a function of N in the case where the dimer chain is coupled to the acoustic phonons (with $\chi = 62$ pN and $H = 10$). The results presented in Fig. 5.7 clearly demonstrate that the edge-state-driven LRPT is absent in the odd-length chains. For all even-length chains considered, the edge-state-driven LRPT not only enables significant population transfer across the chain but it also occurs at a fast rate. Furthermore, as one increases the length of the even-length chains from $N = 4$ to $N = 10$, the efficiency of the LRPT decreases due to an increased population leakage into the bulk. This is likely due to the fact that, as the chain length increases, the overall coupling between the dimer chain and the acoustic phonons also increases (e.g., for a four-site chain, the coupling is 4χ, while for a ten-site chain the coupling is 10χ). As a result, the dimer chain becomes more heavily influenced by the phonons, which in turn affects its ability to support the topological edge modes.

So far, we have demonstrated the robustness of the edge-state transport mechanism in

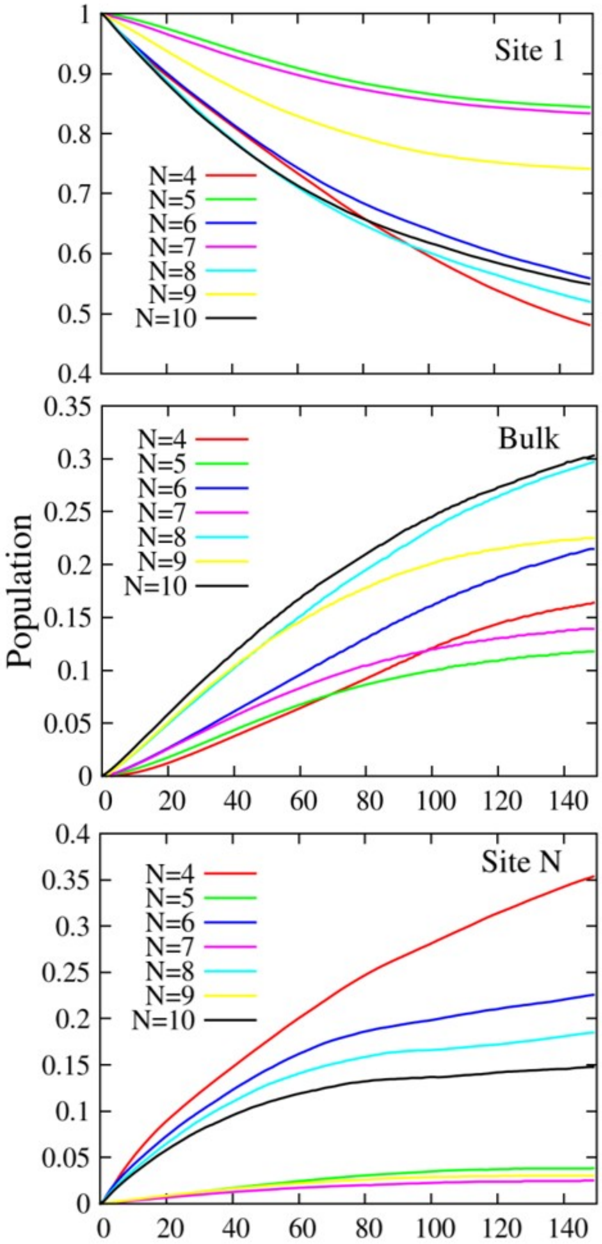

Figure 5.7: Population dynamics for dimer chains of various lengths N with $\chi = 62$ pN and $H = 10$. (Left): Site-1 population. (Center): Bulk population. (Right): Site-N population.

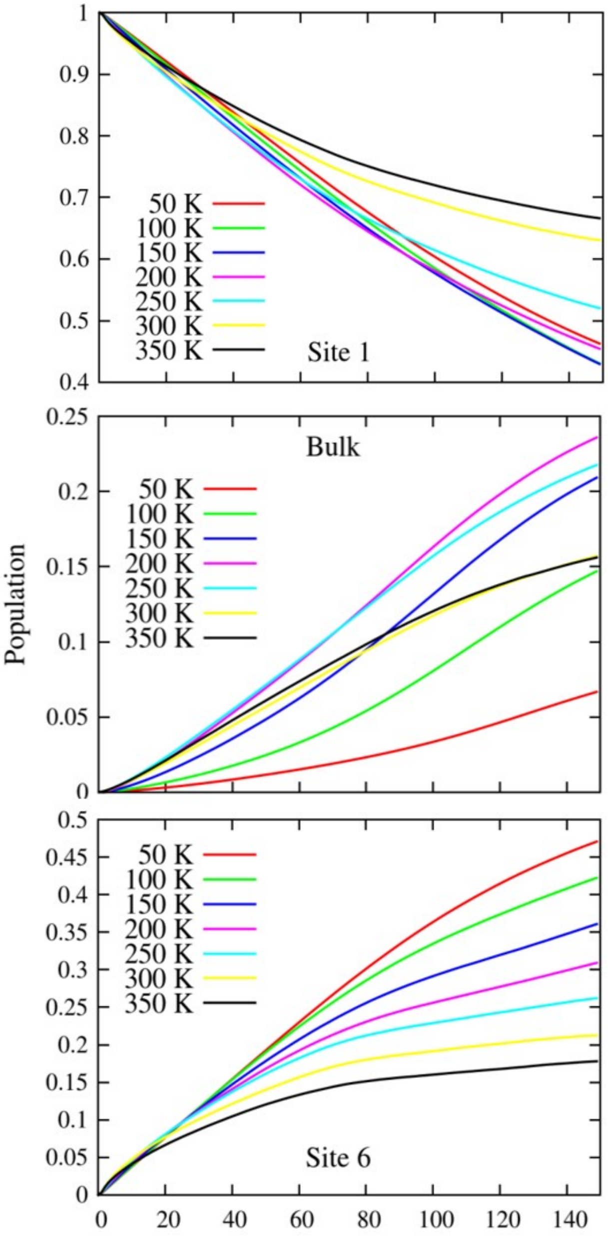

Figure 5.8: Population dynamics in a six-site dimer chain with $\chi = 62$ pN and $H = 10$ for different temperatures of the classical acoustic phonon bath. (Left): Site-1 population. (Center): Bulk population. (Right): Site-6 population.

the dimer chain coupled to an acoustic phonon bath at room temperature (300 K). Now, we investigate how the transfer rate is affected by the bath temperature. On the one hand, a low-temperature environment provides a favourable condition for sustaining the quantum coherence needed to realize the edge states. On the other hand, the phonon excitations are significantly reduced at low temperatures. Since the ultrafast population transfer is only made possible by the coupling to the phonons, it is not immediately obvious how LRPT will be affected by a temperature change. In Fig. 5.8, we present population results for a wide range of bath temperatures, from 50 K to 300 K. It is reassuring to observe that the LRPT remains effective over this entire temperature range, with the LRPT being faster and suffering less leakage to the bulk in the lower temperature regime. Interestingly, as shown in the middle panel of Fig. 5.8, there is a turnover (as function of temperature) in the population leakage to the bulk, which occurs at 200 K.

Further investigation is required to determine whether the nonlinear temperature dependence of the population leakage to the bulk is an artifact of our adiabatic dynamics simulations, which neglect nonadiabatic transitions in the trajectories. Since nonadiabatic transitions are expected to occur more frequently in the high temperature regime where the classical phonons have higher momenta, it is important to get a sense of the magnitude of the nonadiabatic effects in our results. To this end, we performed a nonadiabatic dynamics simulation of the six-site dimer chain coupled to a classical acoustic phonon bath at 300 K. (The algorithmic details of how to perform this simulation, including the Monte Carlo sampling of the nonadiabatic transitions, adjustment of the bath momenta, and the computation of the expectation value are given in Appendix B of Ref. [70].) From Fig. 5.9, we clearly observe the qualitative similarities between the adiabatic and nonadiabatic results, which were generated using 10^7 and 10^9 trajectories, respectively. Quantitatively speaking, the LRPT is seen to be more effective when one uses the more accurate nonadiabatic dynamics, as reflected by the reduction in the bulk population in the middle panel of Fig. 5.9. This reduction validates the existence of the turnover in the population leakage to the bulk shown in the middle panel of Fig. 5.8. The nonadiabatic transitions, induced by the motions of the acoustic phonons, also slow down the depletion of the population on site 1. Finally, the nearly quantitative agreement between the adiabatic and nonadiabatic results for the short-time population transfer on site 6 (see right panel of Fig. 5.9) strongly suggests that the LRPT is primarily captured by the adiabatic dynamics. The role of the nonadiabatic transitions is mainly to suppress the spurious leakage of population into the bulk. Overall, these results confirm that our adiabatic simulations offer a reliable qualitative (and even semi-quantitative) picture of the transfer dynamics.

5.5 Summary

In this work, we studied the vibrational population transfer induced by a quantum excitation that is initially localized on one end of a one-dimensional model of a dimerized quantum chain at 300 K. Our goal was to investigate the possibility of engineering a robust, efficient, ultrafast, and long-range energy transfer mechanism via topologically protected edge states in a molecule. To this end, we performed adiabatic dynamics simulations based on the QCLE approach, which were shown to provide reliable qualitative results of the quantum population transfer dynamics for this model. We found that the nonadiabatic corrections mainly suppress the artificial population leakage (resulting from the adiabatic approximation) into the bulk of the chain.

In contrast to the energy transfer dynamics in a static dimerized chain, a vibrational excitation does not necessarily move sequentially from one site to the next when the static constraint is lifted. When the high-frequency modes couple to the low-frequency lattice displacements along the backbone of the chain and the chain is in its topologically non-trivial

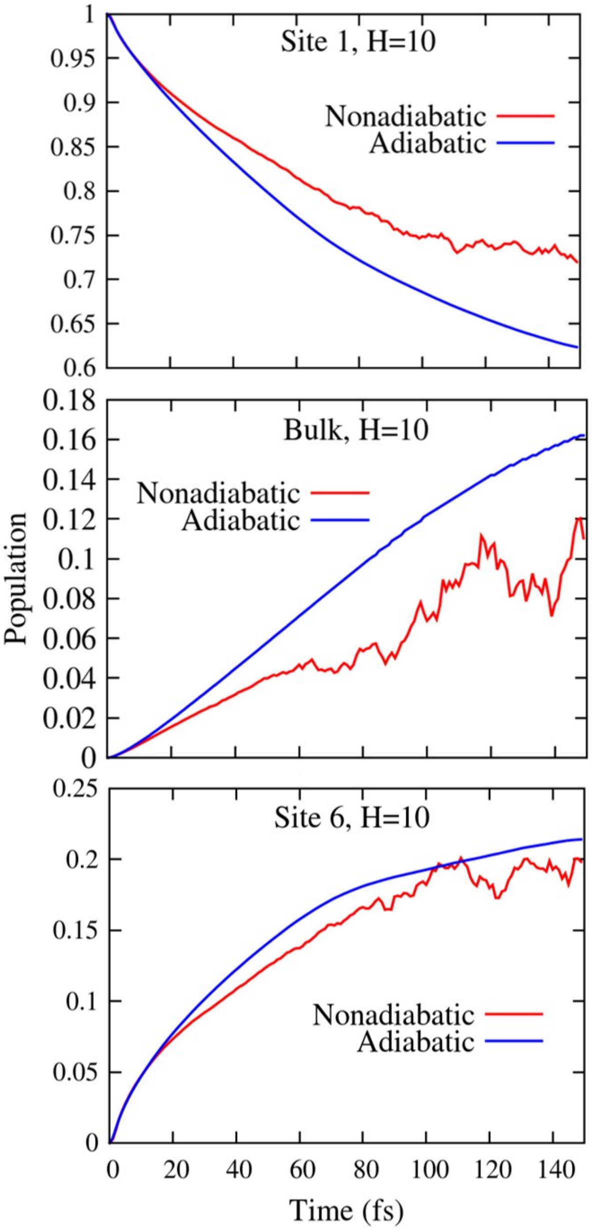

Figure 5.9: Nonadiabatic population dynamics for a six-site dimer chain coupled to a classical acoustic phonon bath at 300 K, with $\chi = 62$ pN and $H = 10$. (Left): Site-1 population. (Center): Bulk population. (Right): Site-6 population.

phase (i.e., $H > H_c$), the transfer primarily involves the population of the edge states $|e^{\pm}\rangle \approx \frac{1}{\sqrt{2}}(|1\rangle + |N\rangle)$. Moreover, the vibrations of the lattice, which are inevitable at finite temperatures, are found to accelerate the transfer rate, instead of decelerating it or localizing the population. A nonlinear dependence of the LRPT on the temperature was observed, suggesting the existence of an optimal temperature range over which the LRPT is most effective. This an important consideration in the design of molecular devices that must operate within a specific temperature range. Finally, we found that the LRPT is robust against weak static disorder, which is a highly desirable trait due to the near impossibility of fabricating a perfectly homogeneous organic structure.

In summary, our findings suggest the possibility that a quasi one-dimensional dimerized molecule may be used as a platform for building devices that are capable of robust, efficient, ultrafast, and long-range vibrational energy transfer via a topologically-protected transfer mechanism. These findings will hopefully stimulate work towards synthesizing polymers with the desired structure and testing their energy transfer properties. So far, our computations have been restricted to relatively short chains and time scales; however, one of the authors has recently proposed a novel approach for accurately simulating QCLE dynamics at high temperatures at a fraction of the computational cost of the existing QCLE-based surface-hopping methods.[85] Thus, it is our desire to investigate the long-time dynamics of more realistic systems using this approach, and thereby gain a more detailed understanding of the quantum dynamical features of topologically-protected energy transfer in this class of materials.

Chapter 6

Vibrational Energy Transfer in a Dimer Chain Coupled to Thermal Reservoirs

6.1 Introduction

The study of excitation energy transfer in molecular and nanoscale materials has become very popular during the last decades due to their potential technological applications [154–158, 158, 159, 159]. Some prominent systems that have been studied include artificial light-harvesting antenna complexes [178–180], photocatalytic nano-composites [181–183], enhanced photoluminescent films [184], sensing and signalling devices [185], etc. In addition, advances in organic and inorganic synthesis have led to the creation of novel architectures with exceptional energy transfer properties [186]. For example, well-defined dendritic polymers have been experimentally and theoretically studied, showing a step-wise energy transfer from the periphery units towards the center with high photochemical stability

[187, 188]. More recently, metal organic frameworks have been explored as new platforms for long-range energy transfer [189, 190]. For example, it has been observed that collapsing a MOF thin film from a 3D to 2D framework can enhance the directional excitonic energy transport [191]. At the same time, the study of heat transport in molecular architectures has received a great deal of attention due to its numerous applications in molecular electronics and nanophononics. These applications include thermal diodes [21, 97–106], thermal logic gates [110, 132], thermal transistors [21, 107–109], quantum heat engines [132, 133] and quantum absorption refrigerators [134, 135].

One of the main challenges in developing such technologies is the optimization of the energy transfer through the complex molecular structure under the influence of a thermal environment. Recently, we demonstrated the possibility of achieving ultrafast, long-range vibrational exciton transfer in a model chain molecule coupled to a set of acoustic phonons [53]. In the present study, we coupling the ends of this chain to thermal baths (each consisting of a set of harmonic oscillators) at different temperatures. This work aims to understand to what extent the nature and rate of the vibrational exciton transfer is affected by the presence of a temperature gradient across the molecule. First, we consider a static chain in which the sites of the model chain are fixed in space. Next, we consider a chain coupled to acoustic phonons in which the sites are allowed to oscillate.

This chapter is organized as follows. In Sec. 6.2, we present the model Hamiltonian. In Sec. 6.3, we provide the simulation details. Finally, the results and conclusions are given in Secs. 6.4 and 6.5, respectively.

6.2 Model Hamiltonian

In Section 1.4 we presented the static version of the dimerized chain model. Next, in Section 5.2 we coupled the chain sites to a set of acoustic phonons, giving rise to the non-static version of the model. In the present chapter, we study the exciton transfer dynamics of both the static and non-static chains whose end sites are coupled to thermal baths at different temperatures (see Fig. 6.1 for a schematic representation).

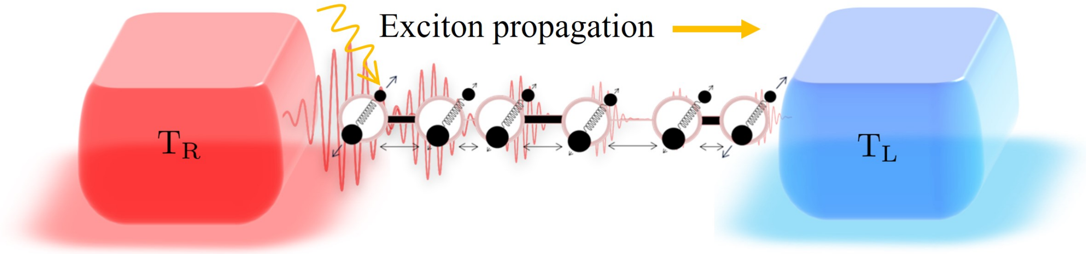

Figure 6.1: Schematic representation of the dimerized chain coupled to two thermal reservoirs at different temperatures T_L and T_R. The red oscillatory curves depict the heat flow down the chain due to the thermal gradient.

We consider the transport of a vibrational exciton along a one-dimensional (1D) dimerized chain of N vibrational quantum modes (also referred to as sites below) whose end modes are coupled to two thermal baths at different temperatures (T_L and T_R with $T_L < T_R$) each consisting of N_μ harmonic oscillators. Additionally, the chain is coupled to a set of N acoustic phonons (corresponding to displacements of the 1D lattice), modelled as classical vibrations. The Hamiltonian of this system is given by

$$H = H_0|0\rangle\langle 0| + \sum_{m,n=1}^{N} H^0_{mn}|\phi_m\rangle\langle\phi_n| + \sum_{m=1}^{N} H_{mm}(R)\,|\phi_m\rangle\,\langle\phi_m|\,, \tag{6.1}$$

where $|\phi_m\rangle = |\chi_{m1}\rangle\prod_{n\neq m}|\chi_{n0}\rangle$ is the m^{th} singly excited state and $|0\rangle = \prod_m|\chi_{m0}\rangle$ is the ground state of a chain. The ground state matrix element is given by

$$\begin{aligned} H_0 \;\; &= \;\; \sum_j \frac{P_j^2}{2M} + \frac{1}{2M'}\sum_{\mu=L,R}\sum_{j=1}^{N_\mu}(P'^2_{j,\mu} + \omega^2_{j,\mu}R'^2_{j,\mu}) + \\ & \quad\;\; \sum_m \left[E_{m0} + (1-\delta_{m,1})\frac{W}{2}(R_m - R_{m-1})^2 + w_{m0}(R)\right], \end{aligned} \tag{6.2}$$

where R_j and P_j are the position and momentum, respectively, of the j^{th} lattice displacement and W is the force constant governing the harmonic motion of the lattice displacement. The primed variables $R'_{j,\mu}$ and $P'_{j,\mu}$ are the position and momentum, respectively, of the j^{th} harmonic oscillator with frequency $\omega_{j,\mu}$ in the μ^{th} bath. The matrix elements for the singly-excited manifold are given by

$$\begin{aligned} H^0_{mn} &= \delta_{m,n}\left[H_0 + E_{m1} - E_{m0}\right] \\ &\quad - J_{mn}\left[\delta_{m-1,n}\langle\phi_m|q_m q_{m-1}|\phi_{m-1}\rangle + \delta_{m,n-1}\langle\phi_n|q_n q_{n-1}|\phi_{n-1}\rangle\right], \end{aligned} \tag{6.3}$$

where $E_{m1} - E_{m0}$ is the energy gap between the ground and first excited states for each site, q_m is the position associated with each site, and the coupling matrix $\mathbf{J}$ is a tridiagonal symmetric matrix with the super-diagonal elements given by alternating parameters J and J' that govern the strength of the transition dipole moment coupling between neighbouring sites (see Sec. 1.4 for a more detailed discussion). The coupling Hamiltonian matrix elements are given by $H_{mm}(R) = w_{m1}(R) - w_{m0}(R)$, where $w_{m\nu}(R)$ takes the following form

$$\begin{aligned} w_{m\nu}(R) &= (1-\delta_{m,1})\frac{\chi}{2}(R_m - R_{m-1})\langle\chi_{m\nu}|q_m^2|\chi_{m\nu}\rangle \\ &\quad + \delta_{m,1}\sum_{j=1}^{N_L} C_{j,L}R'_{j,L}\langle\chi_{m\nu}|q_m^2|\chi_{m\nu}\rangle + \\ &\quad \delta_{m,N}\sum_{j=1}^{N_R} C_{j,R}R'_{j,R}\langle\chi_{m\nu}|q_m^2|\chi_{m\nu}\rangle, \end{aligned} \tag{6.4}$$

with χ and $C_{j,\mu}$ the constants that govern the coupling strength between the quantum modes and the lattice displacements and thermal baths, respectively. The coupling between the subsystem and μ^{th} thermal bath is characterized by an Ohmic spectral density with an exponential cutoff, viz., $I_\mu(\omega) = \frac{\xi_\mu}{2}\pi\omega e^{-\omega/\omega_{c,\mu}}$ with ξ_μ the Kondo parameter characterizing the system-bath coupling strength and $\omega_{c,\mu}$ the cutoff frequency. For this spectral density, the bath reorganization energy, $E_{r,\mu}$, is related to the system-bath coupling strength by $E_{r,\mu} = \xi_\mu \omega_{c,\mu}/2$. The Ohmic spectral density is implemented according to the following discretization scheme [61, 62]

$$C_{j,\mu} \;=\; \sqrt{\xi_\mu \hbar \omega_{0,\mu}}\omega_{j,\mu}, \quad \omega_{j,\mu} = -\omega_{c,\mu} \ln\left(1 - j\frac{\omega_{0,\mu}}{\omega_{c,\mu}}\right), \tag{6.5}$$

where $\omega_{0,\mu} = \omega_{c,\mu}(1 - e^{-\omega_{m,\mu}/\omega_{c,\mu}})/N_\mu$, $\omega_{m,\mu}$ is the maximum frequency of the μ^{th} heat bath, and j runs from 1 to N_μ. In this work, $\omega_{m,L} = \omega_{m,R} = \omega_m$, $\omega_{c,L} = \omega_{c,R} = \omega_c$, and $\xi_L = \xi_R = \xi$ (or, equivalently, $E_{r,L} = E_{r,R} = E_r$). Finally, the matrix elements of $q_m q_{m-1}$ are all given by $\langle \phi_m | q_m q_{m-1} | \phi_{m-1} \rangle = \langle \chi_0 | q | \chi_1 \rangle^2$. The values of the various matrix elements of q_m and q_m^2 are taken from Table 2 in Ref. [69], while the values of the parameters $E_{m1} - E_{m0}$, J, W, and M are taken from Table 1 in Ref. [69] and are given by 1660 cm^{-1}, 7.8 cm^{-1}, 13 N/m, and 87 m_p, respectively. The value of χ used in this study is 5 pN.

6.3 Simulation details

The quantum vibrational modes and classical lattice displacements/thermal baths are assumed to be uncorrelated initially, such that

$$\hat{\rho}\,(0) = \hat{\rho}_q\,(0)\,\rho_e\,(X)\,, \tag{6.6}$$

where $\hat{\rho}_q(0)$ and $\rho_e(X)$ are the initial densities of the quantum subsystem and classical environment, respectively. The initial density matrix of the quantum vibrational modes (represented in the subsystem basis of singly excited states), corresponding to the first quantized mode in the chain being vibrationally excited, is given by

$$\hat{\rho}_q(0) = \begin{pmatrix} 1 & 0 & \cdots & 0 \\ 0 & 0 & \cdots & 0 \\ \vdots & \vdots & \ddots & 0 \\ 0 & 0 & \cdots & 0 \end{pmatrix}. \tag{6.7}$$

The initial state of the quantum subsystem is sampled for each trajectory by first expressing $\hat{\rho}_q(0)$ in the adiabatic basis (see details of the transformation and sampling in Appendix A of Ref. [70]).

For each trajectory, the initial values of the positions/momenta of the lattice displacements and thermal baths are sampled. For the lattice displacements, the sampling is done from a Boltzmann distribution corresponding to a collection of uncoupled harmonic oscillators at thermal equilibrium at 300 K. Starting from these initial values, the correct thermal equilibrium distribution at 300 K (in the absence of a vibrational excitation) is achieved by equilibrating the coupled harmonic oscillators for 2.5 ps using the ground-state Hamiltonian in Eq. 5.2 with a Nosé-Hoover thermostat and a time step of 2 fs. For the thermal bath oscillators, the initial values of the coordinates are sampled from Eq. (3.4). Following the sampling of the initial quantum state (with $N = 6$) and positions/momenta of the classical degrees of freedom (with $N = 6$ and $N_\mu = 1000$), microcanonical trajectories of length 150 fs are generated using the short-time sequential propagation algorithm[84] in the absence of nonadiabatic transitions (i.e., adiabatic dynamics), with a time step of 2 fs. To correct for the majority of arbitrary sign flips in the eigenvectors upon numerical diagonalization of the Hamiltonian matrix at each time step of a trajectory, we use the sign-correction procedure outlined in Ref. [70]. Finally, the time-dependent populations of the quantum modes along the chain are calculated based on an ensemble of 10^8 trajectories according to Eq. 2.15 with $\hat{A} = |\phi_m\rangle\langle\phi_m|$.

6.4 Results and discussion

We start with the case of the static chain coupled to the thermal baths at temperatures $T_L = 350$ K and $T_R = 250$ K. In Fig. 6.2, we show the time-dependent populations of the quantum vibrational modes for different system-bath coupling strengths. The results in the left and right panels are generated using cutoff frequencies $\omega_c = 400$ cm^{-1} and 100 cm^{-1}, respectively. In both cases, we observe that the population transfer from site 1 to site 6 increases with increasing coupling strength, with a negligible change to the bulk site populations. The results corresponding to $\xi = 0.1 \times 10^{-8}$, $\xi = 0.5 \times 10^{-8}$, and $\xi = 1.0 \times 10^{-8}$ are essentially the same as the case where no baths are coupled; however, notable changes appear when the coupling strength is increased to 5.0×10^{-8} and beyond. When $\omega_c = 400$ cm^{-1}, the population transfer from site 1 to site 6 increases up to ~ 0.4 (for the largest system-bath coupling) and exhibits substantial fluctuations. That being said, this behaviour may not be entirely correct, since the adiabatic approximation is expected to deteriorate when the bath frequencies increase. When $\omega_c = 100$ cm^{-1}, the population transfer from site 1 to site 6 increases up to ~ 0.13 (for the largest system-bath coupling), and exhibits smaller fluctuations than in the higher ω_c case. Overall, these results show that the coupling to baths promotes the population transfer.

To study the effect of the bath temperature gap on the population transfer in the static chain, we vary the temperature of one bath while the other is kept constant at 300 K. Since we are using adiabatic dynamics, we focus on a low bath cutoff frequency case, $\omega_c = 100$ cm^{-1}, and intermediate coupling strength, $\xi = 5.0 \times 10^{-8}$, to ensure that the dynamics is within the adiabatic regime. Overall, Fig. 6.3 shows that, despite some quantitative differences, the temperature gradient does not have a pronounced effect on

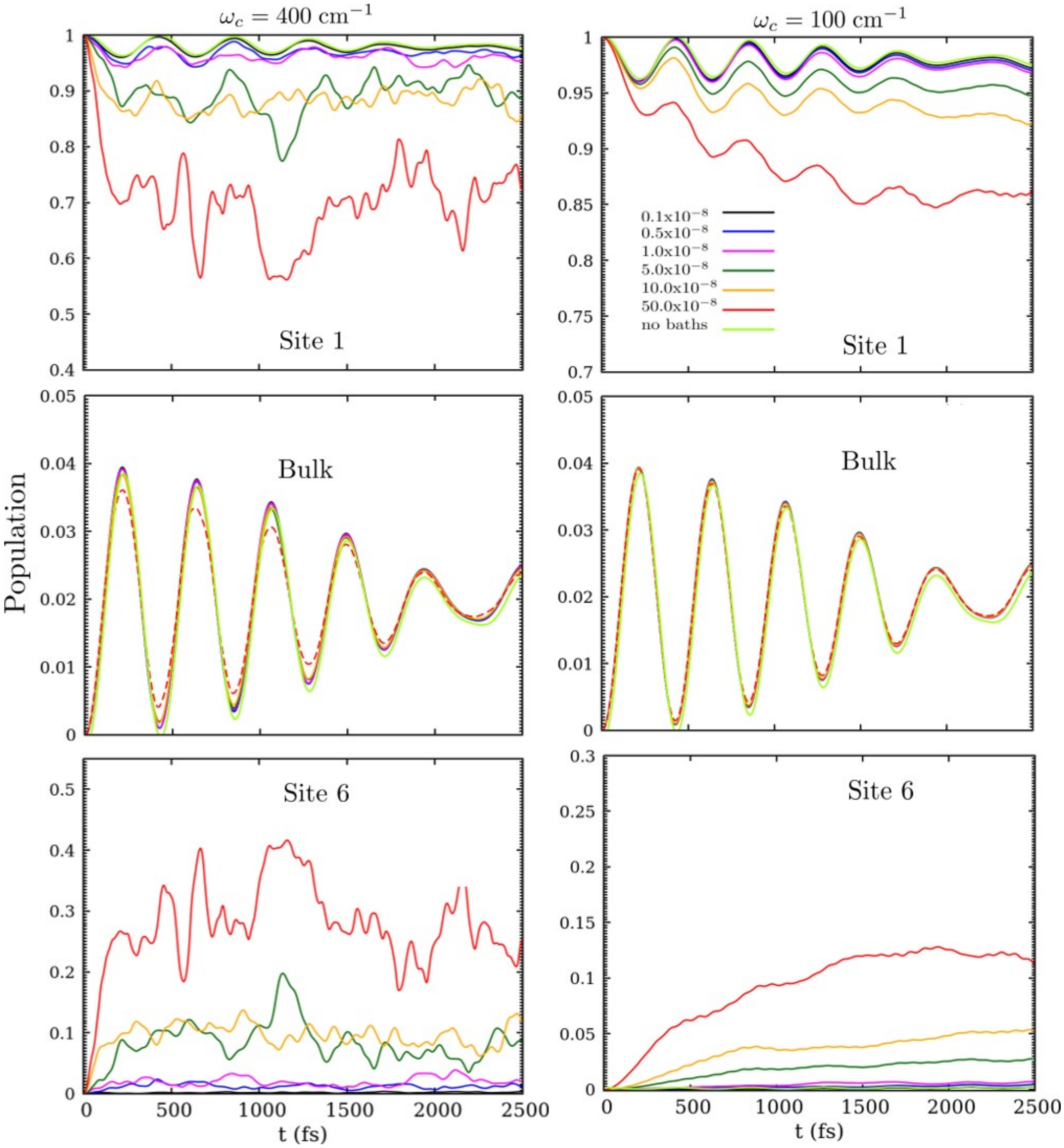

Figure 6.2: Site population dynamics in the static six-site dimer chain with $\omega_c = 100$ cm^{-1} (right panels) and $\omega_c = 400$ cm^{-1} (left panels) for different system-bath coupling strengths. In all cases, $T_L = 350$ K and $T_R = 250$ K. *Top panels*: site 1 population, *center panels*: bulk population, *bottom panels*: site 6 population.

the population transfer from site 1 to site 6 regardless of the direction of the gradient, i.e., $T_L > T_R$ or $T_R > T_L$. Therefore, although one may expect that a larger temperature gap would have a pronounced effect on the population transfer, we see that this is not the case under the particular conditions considered.

We now turn to the non-static chain, which includes both the coupling between the quantum modes and the acoustic phonons and the coupling to the thermal baths at temperatures T_L = 350 K and T_R = 250 K. In Fig. 6.4, we show the time-dependent populations of the quantum vibrational modes for different system-bath coupling strengths and a site-phonon coupling of χ =5 pN, with the results in the left and right panels generated using cutoff frequencies, ω_c, of 400 cm^{-1} and 100 cm^{-1}, respectively. [In this case, we considered much larger system-bath couplings (on the order of 10^4 times larger) because no changes in the time-dependent site populations were observed for the smaller couplings.] When ω_c = 400 cm^{-1}, we do not observe any clear trend with increasing system-bath coupling, in contrast to the static chain case. Also, the site-1 and site-6 populations are very noisy, in contrast to the rather smooth oscillatory behaviour observed in the no-bath case; that being said, their mean behaviours do not differ substantially from the no-bath case. When ω_c = 100 cm^{-1}, we observe a pronounced dampening of the site-1 and site-6 populations with increasing system-bath coupling strength, but no substantial differences in the mean populations at the longer times. Overall, in the case of the non-static chain coupled to the thermal baths, one observes large changes in the fluctuations of the populations and only minor changes in their averages, compared to the no-bath case.

We finally study the effect of the bath temperature gap on the population transfer in the non-static chain, varying the temperature of one bath while the other is kept constant at 300 K (with $\omega_c = 100$ cm^{-1} and $\xi = 5.0 \times 10^{-4}$). As in the case of the static chain, Fig. 6.5 shows that, despite some quantitative differences, the temperature gradient does not have a

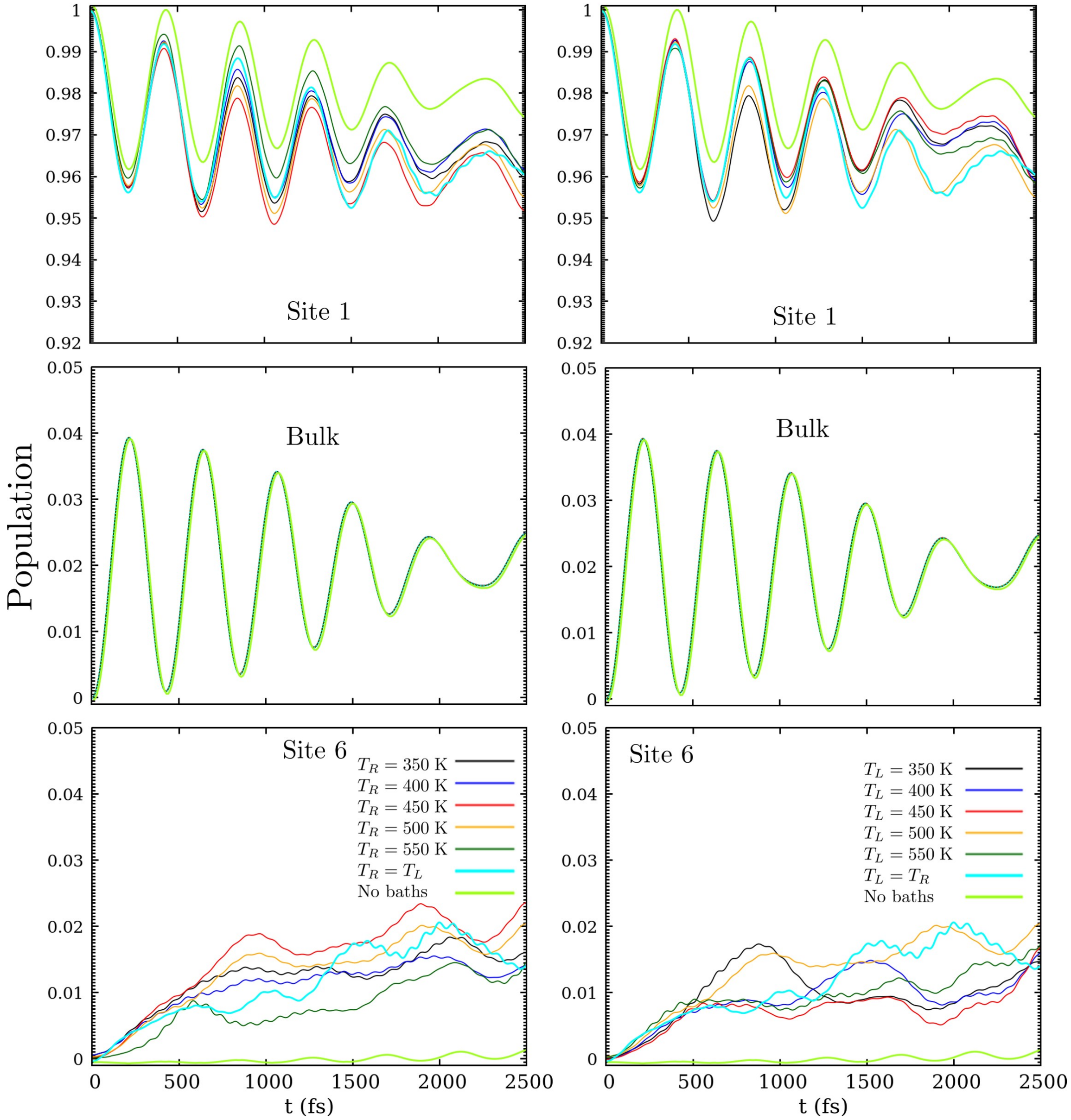

Figure 6.3: Site population dynamics in the static six-site dimer chain with $\omega_c = 100$ cm^{-1} and $\xi = 5.0 \times 10^{-8}$ for different temperature gaps. In the left and right panels, T_L and T_R are kept constant, respectively. *Top panels*: site 1 population, *center panels*: bulk population, *bottom panels*: site 6 population.

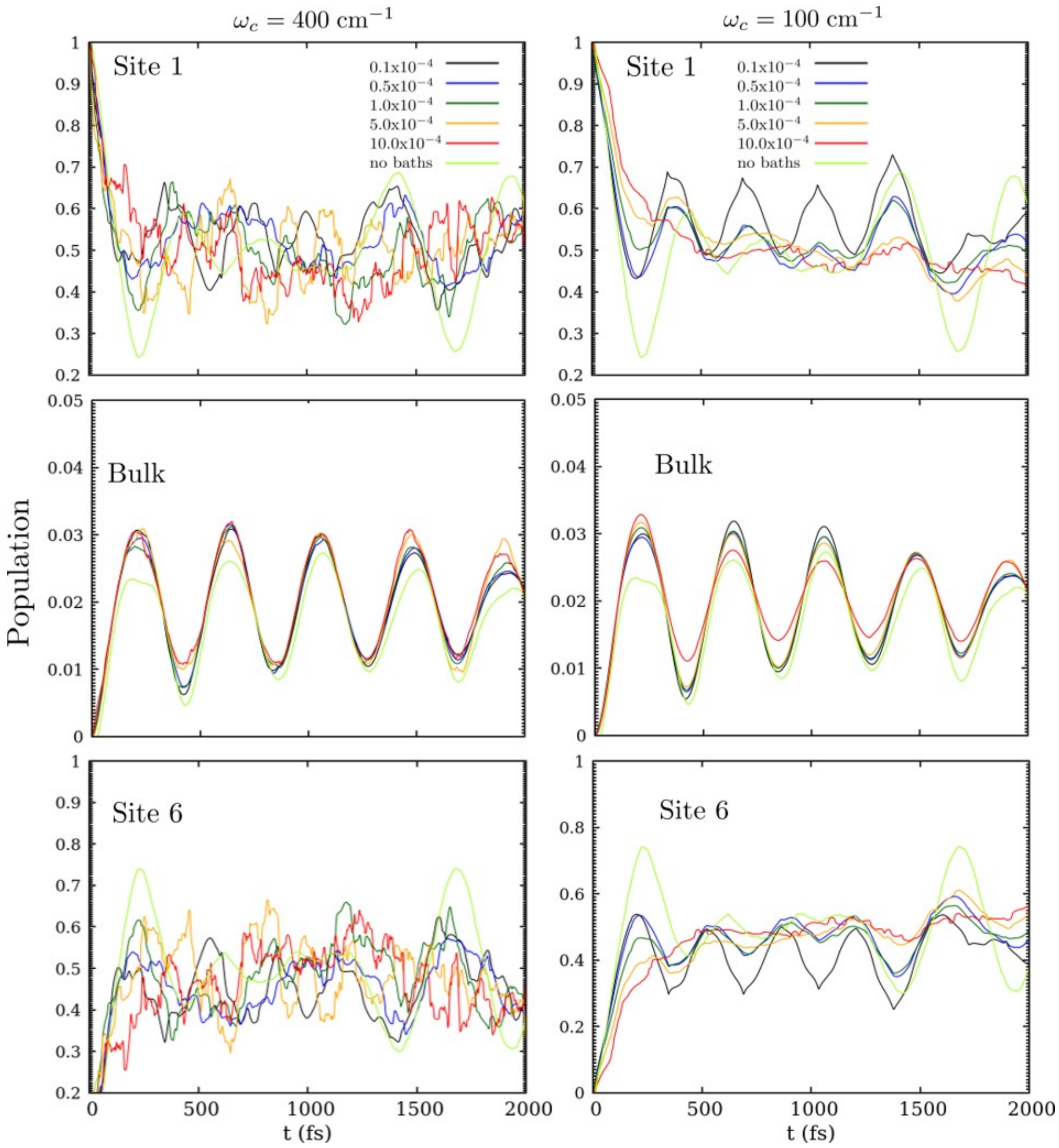

Figure 6.4: Site population dynamics in the non-static six-site dimer chain with $\omega_c = 100$ cm^{-1} (right panels) and $\omega_c = 400$ cm^{-1} (left panels) for different system-bath coupling strengths. In all cases, $T_L = 250$ K and $T_R = 350$ K. *Top panels*: site 1 population, *center panels*: bulk population, *bottom panels*: site 6 population.

pronounced effect on the population transfer from site 1 to site 6 regardless of the direction of the gradient. Moreover, on average, the population transferred does not differ too much from the no-bath case, viz., ~ 0.5. Based on the above results, we see that coupling the end sites to the baths (at least for the form of the coupling that we adopted) merely tames the population fluctuations regardless of the magnitude and direction of the thermal gradient. In contrast to the static chain where the population transfer was enhanced, in this case it remains approximately the same compared to the no-bath case. Thus, the coupling to the lattice displacements both increases the population transfer [53] and dampens the population fluctuations (through energy exchange between the bath and lattice modes).

6.5 Summary

In this work, we studied vibrational exciton transport in a one-dimensional model of a dimerized chain of quantum modes under the influence of a thermal gradient. Our goal was to investigate how and to what extent a thermal gradient affects the edge states and, in turn, the energy transport. To this end, we performed adiabatic dynamics simulations on static and non-static versions of the chain. In the case of the static chain, we showed that it is possible to increase the vibrational population transfer by a selecting a sufficiently large system-bath coupling strength. For the parameter sets considered, our results showed that increasing the thermal gradient does not have a significant effect on the population transfer. In the case of the non-static chain, we also found that the edge states are maintained when the end sites are coupled to thermal baths. Overall, our results reveal that the long-range population transfer is robust against the noise induced by the thermal baths. These findings suggest the possibility of engineering new devices capable of efficient exciton transfer through a junction molecule in the presence of thermal noise.

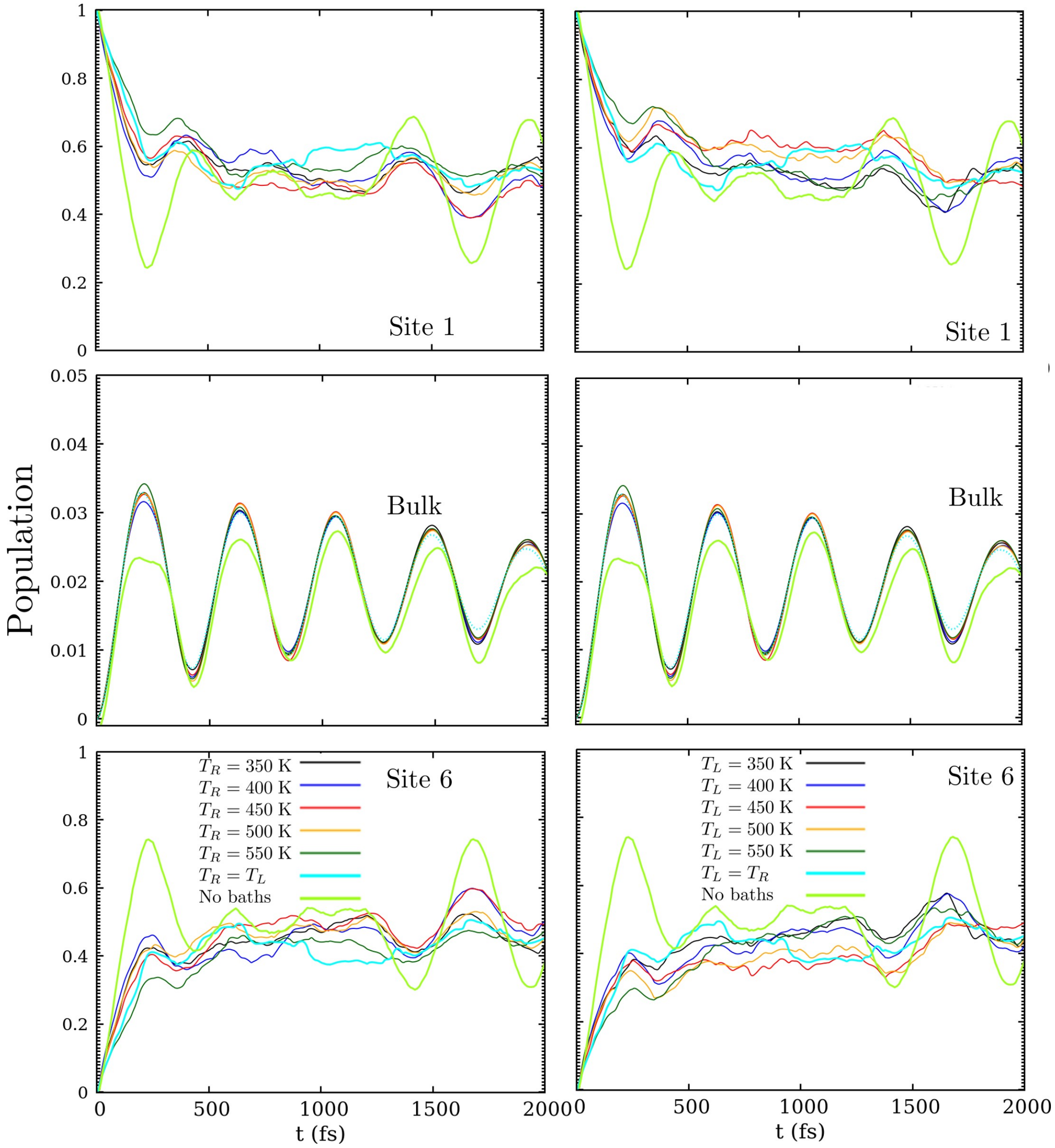

Figure 6.5: Site population dynamics in the static six-site dimer chain with $\omega_c = 100$ cm^{-1} and $\xi = 5.0 \times 10^{-4}$ for different temperature gaps. In the left and right panels, T_L and T_R are kept constant, respectively. *Top panels*: site 1 population, *center panels*: bulk population, *bottom panels*: site 6 population.

Chapter 7

Conclusions and Future Work

7.1 Summary

The study of energy transfer processes at the nanoscale poses a remarkable challenge as it may involve simulating the dynamics of open quantum systems. A commonly studied architecture in this field is the molecular junction, which may be treated as an open quantum system (because the junction molecule is connected to leads/baths, constituting the environment). Depending on the nature of the molecular junction, a number of theoretical methodologies have been used to study quantum transport through the molecule, e.g., ML-MCTDH, NEGF methods, noninteracting-blip approximation, nonequilibrium polaron-transformed Redfield equation, path-integral based methods, Monte Carlo, etc. Some of these methods are even numerically exact or yield very accurate results in certain regimes, but their application to complex, realistic systems is limited due to their high computational costs. To overcome this issue, in this thesis, we demonstrated the utility of several mixed-quantum classical approaches based on approximate solutions of the QCLE for studying energy transport in open quantum systems.

In Chapter 3, we showed that the DECIDE method offers a relatively cheap and accurate way of simulating quantum heat transport by calculating steady-state heat currents in the NESB model for a wide range of parameter regimes and comparing our results with those of the numerically exact ML-MCTDH method. In particular, we tested the ability of DECIDE to reproduce the turnovers in the steady-state heat current with respect to i) the tunneling frequency of the spin subsystem and ii) the bath reorganization energy (which provides a measure of the coupling strength between the spin and the thermal baths). DECIDE was not only capable of capturing these turnovers, but was also capable of predicting the maxima at which the turnovers occur. In addition, we compared the results of DECIDE (a nonadiabatic dynamical method) with those obtained with adiabatic dynamics to study the importance of nonadiabatic effects in quantum heat transport. Adiabatic dynamics was not capable of capturing the turnovers in the steady-state heat current and showed drastic deviations with the exact results, especially in the fast-bath limit. These observations led us to the conclusion that nonadiabatic effects are very important over a wide range of the parameter regimes.

In Chapter 4, we investigated the differences between sampling the initial bath coordinates from quantum and classical distributions in trajectory-based mixed quantum-classical simulations of heat currents in thermal molecular junctions. This was done within the context of the NESB model, by sampling the initial positions and momenta of the harmonic bath oscillators from both quantum and classical distributions and comparing the resulting steady-state heat currents. Over a wide range of temperatures, the classical distribution is narrower than the quantum one. As a result, the difference in the widths of the classical distributions corresponding to the hot and cold baths are larger than their quantum counterparts. These width differences were found to yield pronounced differences in the magnitudes of the steady state heat currents (the classical ones being $\sim 1.3 - 4.5$

times higher than the quantum ones for most of the parameter regimes considered). In addition, sharper turnovers in the steady-state heat currents were observed in the case of the classical bath sampling. Finally, we checked the validity of the SSFT, which provides a rigorous constraint on the heat current fluctuations and generalizes the second law of thermodynamics to the nanoscale. We found that, in the Markovian regime, the SSFT is satisfied only when quantum bath sampling is used. Overall, our findings (i) underscore the importance of quantum bath sampling (across a wide range of parameter regimes) when simulating heat transfer dynamics in thermal molecular junctions, even at high temperatures where a classical description may be considered sufficient, and ii) suggest the possibility of optimizing steady-state heat currents in molecular junctions by engineering the initial equilibrium structures of the thermal baths.

In Chapter 5, we used adiabatic mixed-quantum classical dynamics to study excitonic energy transfer in a dimer chain model. To monitor the energy transfer across the chain, we focused on the time-dependent population of the first vibrational excited state of the chain. In the case of the static chain (i.e., the chain decoupled from the lattice displacements), we found that long-range population transfer (LRPT) occurs with ~ 50 % of the population transferring from site 1 to site 6 in ~ 50 ps. On the other hand, in the case of the non-static chain (i.e., the chain coupled to the lattice displacements), the LRPT proceeds at a much faster rate with ~ 75 % of the population transferring in ~ 200 fs. Moreover, we found a nonlinear dependence of the LRPT on temperature, suggesting the existence of a critical temperature at which the population transfer reaches a maximum. Because of the disorder commonly encountered in molecular architectures, we studied the effect of introducing weak static disorder into the chain and found that the LRPT is only slightly affected. Overall, we showed that the LRTP in this dimer chain is highly robust, suggesting the possibility that a quasi one-dimensional dimerized structure may be used as a platform for devices that are capable of robust, efficient, ultrafast, and long-range excitonic energy transfer.

In Chapter 6, we applied adiabatic mixed-quantum classical dynamics to study excitonic energy transfer in a model dimer chain whose end sites are coupled to thermal baths at different temperatures. For the parameter regimes considered, we found that the LRPT in the static chain increases significantly when a sufficiently strong site-bath coupling is used compared to the no-bath case. Moreover, this enhancement is not affected neither by the temperature gap nor by the direction of the thermal gradient. As for the non-static chain, we found that the edge states involved in the LRPT are preserved even for the largest temperature gaps considered. For both the static and non-static chains, very little population is leaked to the bulk sites, showing that the presence of a thermal gradient does not affect the LRPT process. Altogether, these findings indicate that, in principle, one could achieve ultrafast LRPT, even when a nanoscale device is coupled to thermal environments.

7.2 Future work

In Chapters 4 and 5, we computed first moments of the heat (i.e., average heat transferred) and heat currents in the NESB model. Higher moments, like the second moment (variance) or third moment (skew), contain information about higher order correlations of the transferred heat. Thus, it would be worthwhile to calculate the variance of the heat and heat current fluctuations in the NESB model for a wide range of parameter regimes.

In Chapters 5 and 6, we performed adiabatic dynamics to study the population transfer dynamics in the SSH chain coupled to various classical environments. Although nonadiabatic effects were deemed to be rather minor under the conditions investigated, it would be worthwhile to apply the DECIDE method to chains for which nonadiabatic effects are expected to play a larger role, viz., chains that are more strongly coupled to their classical environments and/or have smaller frequency scale separations between the quantum and classical DOF. Such a study would shed light on the nature and rate of the energy/population transfer in more strongly nonadiabatic regimes. Additionally, instead of coupling the harmonic oscillator baths only to the end sites of the quantum chain, one could consider the effects of also coupling the baths to the lattice modes of the end sites.

In Chapter 6, we focused on a specific topological class of the model chain i.e., the case where the critical parameter $H_c = (1 - 1/(N+1))^{-1/2}$. Thus, it would be worthwhile to explore other topological scenarios and analyze the effects of thermal gradients on the excitation energy transfer.

Bibliography

[1] Bondarenko, A. S.; Knoester, J.; Jansen, T. L. *Chem. Phys.* **2020**, *529*, 110478.

[2] Shibl, M. F.; Schulze, J.; Al-Marri, M. J.; Kühn, O. *J. Phys. B.* **2017**, *50*, 184001.

[3] Häse, F.; Kreisbeck, C.; Aspuru-Guzik, A. *Chem. Sci.* **2017**, *8*, 8419–8426.

[4] Lambrev, P. H.; Akhtar, P.; Tan, H.-S. *Biochim. Biophys. Acta.* **2020**, *1861*, 148050.

[5] Thilagam, A. *J. Math. Chem.* **2015**, *53*, 466–494.

[6] Thoss, M.; Evers, F. *J. Chem. Phys.* **2018**, *148*, 030901.

[7] Xiang, D.; Wang, X.; Jia, C.; Lee, T.; Guo, X. *Chem. Rev.* **2016**, *116*, 4318–4440.

[8] McCreery, R. L.; Bergren, A. J. *Adv. Mater.* **2009**, *21*, 4303–4322.

[9] Akhlaghi, H.; Roohi, E.; Stefanov, S. *Int. J. Therm. Sci.* **2012**, *59*, 111–125.

[10] Hosseini, S. M. *Appl. Math. Model.* **2018**, *57*, 21–36.

[11] Mosso, N.; Sadeghi, H.; Gemma, A.; Sangtarash, S.; Drechsler, U.; Lambert, C.; Gotsmann, B. *Nano Lett.* **2019**, *19*, 7614–7622.

[12] Liu, X.; Zhang, G.; Zhang, Y.-W. *J. Phys. Chem. C* **2014**, *118*, 12541–12547.

[13] Xu, Y.; Chen, X.; Wang, J.-S.; Gu, B.-L.; Duan, W. *Phys. Rev. B* **2010**, *81*, 195425.

[14] Luo, T.; Lloyd, J. R. *Adv. Funct. Mater.* **2012**, *22*, 2495–2502.

[15] Dinpajooh, M.; Nitzan, A. *J. Chem. Phys.* **2020**, *153*, 164903.

[16] Rubtsova, N. I.; Qasim, L. N.; Kurnosov, A. A.; Burin, A. L.; Rubtsov, I. V. *Acc. Chem. Res.* **2015**, *48*, 2547–2555.

[17] Meier, T.; Menges, F.; Nirmalraj, P.; Hölscher, H.; Riel, H.; Gotsmann, B. *Phys. Rev. Lett.* **2014**, *113*, 060801.

[18] Bello, M.; Creffield, C. E.; Platero, G. *Sci. Rep.* **2016**, *6*, 1–9.

[19] Harriman, A. *ChemComm.* **2015**, *51*, 11745–11756.

[20] Davydov, A. S. *J. Theor. Biol.* **1973**, *38*, 559–569.

[21] Li, N.; Ren, J.; Wang, L.; Zhang, G.; Hänggi, P.; Li, B. *Rev. Mod. Phys.* **2012**, *84*, 1045.

[22] Mora-Barzaga, G.; Miranda, E.; Bringa, E. *J. Appl. Phys.* **2020**, *127*, 224303.

[23] Wang, Z. *Mater. Today Commun.* **2020**, *22*, 100822.

[24] Jolfaei, N. A.; Jolfaei, N. A.; Hekmatifar, M.; Piranfar, A.; Toghraie, D.; Sabetvand, R.; Rostami, S. *Comput. Methods Programs Biomed.* **2020**, *185*, 105169.

[25] Dong, H.; Fan, Z.; Shi, L.; Harju, A.; Ala-Nissila, T. *Phys. Rev. B* **2018**, *97*, 094305.

[26] Hu, S.; Zhang, Z.; Jiang, P.; Chen, J.; Volz, S.; Nomura, M.; Li, B. *J. Phys. Chem. Lett.* **2018**, *9*, 3959–3968.

[27] Pei, Q.-X.; Zhang, Y.-W.; Sha, Z.-D.; Shenoy, V. B. *J. Appl. Phys.* **2013**, *114*, 033526.

[28] Li, X.; Maute, K.; Dunn, M. L.; Yang, R. *Phys. Rev. B* **2010**, *81*, 245318.

[29] Gu, H.; Wang, H. *Comput. Mater. Sci.* **2018**, *144*, 133–138.

[30] Sun, Y.; Zhou, Y.; Han, J.; Hu, M.; Xu, B.; Liu, W. *J. Appl. Phys.* **2020**, *127*, 045106.

[31] Termentzidis, K.; Isaiev, M.; Salnikova, A.; Belabbas, I.; Lacroix, D.; Kioseoglou, J. *Phys. Chem. Chem. Phys.* **2018**, *20*, 5159–5172.

[32] Zhang, Z.; Xie, Y.; Peng, Q.; Chen, Y. *Solid State Commun.* **2015**, *213-214*, 31–36.

[33] Gill, S. P. *Nonequilibrium Molecular Dynamics and Multiscale Modeling of Heat Conduction in Solids*; Springer, 2010; pp 85–134.

[34] Kaviany, M. *Heat Transfer Physics*, 2nd ed.; Cambridge University Press, 2014.

[35] Das, S. G.; Dhar, A. *Eur. Phys. J. B* **2012**, *85*, 1–8.

[36] Sadasivam, S.; Che, Y.; Huang, Z.; Chen, L.; Kumar, S.; Fisher, T. S. *Annu. Rev. Heat Transf.* **2014**, *17*.

[37] Jin, J.; Zheng, X.; Yan, Y. *J. Chem. Phys.* **2008**, *128*, 234703.

[38] Zheng, X.; Jin, J.; Welack, S.; Luo, M.; Yan, Y. *J. Chem. Phys.* **2009**, *130*, 164708.

[39] Tanimura, Y. *J. Chem. Phys.* **2020**, *153*, 020901.

[40] Yang, C.-H.; Wang, H. *Entropy* **2020**, *22*, 1099.

[41] Velizhanin, K. A.; Wang, H.; Thoss, M. *Chem. Phys. Lett.* **2008**, *460*, 325–330.

[42] Makri, N.; Makarov, D. E. *J. Chem. Phys.* **1995**, *102*, 4611–4618.

[43] Makri, N.; Makarov, D. E. *J. Chem. Phys.* **1995**, *102*, 4600–4610.

[44] Boudjada, N.; Segal, D. *J. Phys. Chem. A* **2014**, *118*, 11323–11336.

[45] Redfield, A. G. *IBM J. Res. Dev.* **1957**, *1*, 19–31.

[46] Nakajima, S. *Prog. Theor. Phys.* **1958**, *20*, 948–959.

[47] Zwanzig, R. *J. Chem. Phys.* **1960**, *33*, 1338–1341.

[48] Saito, K.; Kato, T. *Phys. Rev. Lett.* **2013**, *111*, 214301.

[49] Werner, P.; Oka, T.; Millis, A. J. *Phys. Rev. B* **2009**, *79*, 035320.

[50] Schiró, M.; Fabrizio, M. *Phys. Rev. B* **2009**, *79*, 153302.

[51] Carpio-Martínez, P.; Hanna, G. *J. Chem. Phys.* **2019**, *151*, 074112.

[52] Carpio-Martínez, P.; Hanna, G. *J. Chem. Phys.* **2021**, *154*, 094108.

[53] Hsieh, C.-Y.; Carpio-Martinez, P.; Hanna, G. *Chem. Phys.* **2018**, *515*, 315–322.

[54] Liu, J.; Hsieh, C.-Y.; Segal, D.; Hanna, G. *J. Chem. Phys.* **2018**, *149*, 224104.

[55] Liu, J.; Gomez, V. A. M.; Hanna, G. AIP Conf. Proc. 2018; p 020012.

[56] Li, M.; Freedman, H.; Dell'Angelo, D.; Hanna, G. AIP Conf. Proc. 2017; p 030007.

[57] Freedman, H.; Hanna, G. *Chem. Phys.* **2016**, *477*, 74–87.

[58] Kelly, A. *J. Chem. Phys.* **2019**, *150*, 204107.

[59] Wigner, E. *Phys. Rev.* **1932**, *40*, 749–759.

[60] Weiss, U. *Quantum dissipative systems*; World Scientific, 2012; Vol. 13.

[61] Thompson, K.; Makri, N. *J. Chem. Phys.* **1999**, *110*, 1343–1353.

[62] Wang, H.; Thoss, M.; Miller, W. H. *J. Chem. Phys.* **2001**, *115*, 2979–2990.

[63] Wang, C.; Ren, J.; Cao, J. *Sci. Rep.* **2015**, *5*, 11787.

[64] Ren, J. *Phys. Rev. B* **2013**, *88*, 220406.

[65] Niskanen, A.; Nakamura, Y.; Pekola, J. P. *Phys. Rev. B* **2007**, *76*, 174523.

[66] Zhu, L.; Kirchner, S.; Si, Q.; Georges, A. *Phys. Rev. Lett.* **2004**, *93*, 267201.

[67] Pérez-González, B.; Bello, M.; Gómez-León, Á.; Platero, G. *arXiv preprint arXiv:1802.03973* **2018**,

[68] Asbóth, J. K.; Oroszlány, L.; Pályi, A. *A Short Course on Topological Insulators*; Springer, 2016; pp 1–22.

[69] Tsivlin, D. V.; May, V. **2007**, *338*, 150 – 159.

[70] Freedman, H.; Hanna, G. *Chem. Phys.* **2016**, *477*, 74 – 87.

[71] Monari, A.; Bendazzoli, G. L.; Evangelisti, S. *J. Chem. Phys.* **2008**, *129*, 134104.

[72] Bendazzoli, G. L.; Evangelisti, S. *Adv. Quantum Chem.* **2004**, *47*, 347–368.

[73] Bello, M.; Creffield, C.; Platero, G. *Sci. Rep.* **2016**, *6*, 22562.

[74] Shin, B. C. *Bull. Aust. Math. Soc.* **1997**, *55*, 249–254.

[75] Wang, B.; Zhao, C. *J. Appl. Phys* **2020**, *127*, 073106.

[76] Ke, S.; Wang, B.; Long, H.; Wang, K.; Lu, P. *Opt. express* **2017**, *25*, 11132–11143.

[77] Ge, L.; Wang, L.; Xiao, M.; Wen, W.; Chan, C. T.; Han, D. *Opt. express* **2015**, *23*, 21585–21595.

[78] Crespo-Otero, R.; Barbatti, M. *Chem. Rev.* **2018**, *118*, 7026–7068.

[79] Kapral, R. *J. Phys. Condens. Matter.* **2015**, *27*, 073201.

[80] Kapral, R.; Ciccotti, G. *J. Chem. Phys.* **1999**, *110*, 8919–8929.

[81] Wigner, E. *Phys. Rev.* **1932**, *40*, 749–759.

[82] Imre, K.; Özizmir, E.; Rosenbaum, M.; Zweifel, P. *J. Math. Phys.* **1967**, *8*, 1097–1108.

[83] Kapral, R.; Ciccotti, G. *J. Chem. Phys.* **1999**, *110*, 8919–8929.

[84] MacKernan, D.; Kapral, R.; Ciccotti, G. *J. Phys.: Condens. Matter* **2002**, *14*, 9069–9076.

[85] Liu, J.; Hanna, G. *J. Phys. Chem. Lett.* **2018**, *9*, 3928–3933.

[86] MacKernan, D.; Kapral, R.; Ciccotti, G. *J. Phys. Condens. Matter* **2002**, *14*, 9069.

[87] Hanna, G.; Kapral, R. *J. Chem. Phys.* **2005**, *122*, 244505.

[88] Mac Kernan, D.; Ciccotti, G.; Kapral, R. *J. Chem. Phys. B* **2008**, *112*, 424–432.

[89] Lepri, S.; Livi, R.; Politi, A. *Phys. Rep.* **2003**, *377*, 1–80.

[90] Casati, G. *Chaos* **2005**, *15*, 015120.

[91] Galperin, M.; Ratner, M. A.; Nitzan, A. *J. Phys. Condens. Matter* **2007**, *19*, 103201.

[92] Dhar, A. *Adv. Phys.* **2008**, *57*, 457–537.

[93] Li, B.; Lan, J.; Wang, L. *Phys. Rev. Lett.* **2005**, *95*, 104302.

[94] Zhang, G.; Li, B. *Nanoscale* **2010**, *2*, 1058–1068.

[95] Pop, E. *Nano. Res.* **2010**, *3*, 147–169.

[96] Dubi, Y.; Ventra, M. D. *Rev. Mod. Phys.* **2011**, *83*, 131.

[97] Segal, D.; Nitzan, A. *J. Chem. Phys.* **2005**, *122*, 194704.

[98] Segal, D. *Phys. Rev. Lett.* **2005**, *94*, 034301.

[99] Terraneo, M.; Peyrard, M.; Casati, G. *Phys. Rev. Lett.* **2002**, *88*, 094302.

[100] Li, B.; Wang, L.; Casati, G. *Phys. Rev. Lett.* **2004**, *93*, 184301.

[101] Segal, D. *Phys. Rev. B* **2006**, *73*, 205415.

[102] Wu, L.-A.; Segal, D. *Phys. Rev. Lett.* **2009**, *102*, 095503.

[103] Wu, L.-A.; Claire, X. Y.; Segal, D. *Phys. Rev. E* **2009**, *80*, 041103.

[104] Liu, H.; Wang, H.; Zhang, X. *Appl. Sci.* **2019**, *9*, 344.

[105] Fiorino, A.; Thompson, D.; Zhu, L.; Mittapally, R.; Biehs, S.-A.; Bezencenet, O.; El-Bondry, N.; Bansropun, S.; Ben-Abdallah, P.; Meyhofer, E.; Reddy, P. *ACS Nano* **2018**, *12*, 5774–5779.

[106] Martínez-Pérez, M. J.; Fornieri, A.; Giazotto, F. *Nat. Nanotechnol.* **2015**, *10*, 303.

[107] Segal, D.; Nitzan, A. *Phys. Rev. E* **2006**, *73*, 026109.

[108] Li, B.; Wang, L.; Casati, G. *Appl. Phys. Lett.* **2006**, *88*, 143501.

[109] Segal, D. *Phys. Rev. Lett.* **2008**, *101*, 260601.

[110] Wang, L.; Li, B. *Phys. Rev. Lett.* **2007**, *99*, 177208.

[111] Leggett, A. J.; Chakravarty, S.; Dorsey, A. T.; Fisher, M. P. A.; Garg, A.; Zwerger, W. *Rev. Mod. Phys.* **1987**, *59*, 1.

[112] Nicolin, L.; Segal, D. *J. Chem. Phys.* **2011**, *135*, 164106.

[113] Chen, T.; Wang, X.-B.; Ren, J. *Phys. Rev. B* **2013**, *87*, 144303.

[114] Segal, D.; Nitzan, A. *Phys. Rev. Lett.* **2005**, *94*, 034301.

[115] Liu, J.; Xu, H.; Li, B.; Wu, C. *Phys. Rev. E* **2017**, *96*, 012135.

[116] Nicolin, L.; Segal, D. *Phys. Rev. B* **2011**, *84*, 161414.

[117] Yang, Y. Y.; Wu, C.-Q. *EPL* **2014**, *107*, 30003.

[118] Velizhanin, K. A.; Thoss, M.; Wang, H. *J. Chem. Phys.* **2010**, *133*, 084503.

[119] Liu, J.; Xu, H.; Li, B.; Wu, C. *Phys. Rev. E* **2017**, *96*, 012135.

[120] Segal, D. *Phys. Rev. B* **2013**, *87*, 195436.

[121] Segal, D. *Phys. Rev. B* **2013**, *87*, 195436.

[122] Levitov, L. S.; Lee, H.-W.; Lesovik, G. B. *J. Math. Phys.* **1996**, *37*, 4845.

[123] Aleksandrov, I. V. *Z. Naturforsch A* **1981**, *36*, 902.

[124] Gerasimenko, V. I. *Theor. Math. Phys.* **1982**, *50*, 77.

[125] Zhang, W. Y.; Balescu, R. *J. Plasma Phys.* **1988**, *40*, 199.

[126] Dormand, J. R.; Prince, P. J. *J. Comp. Appl. Math.* **1980**, *6*, 19–26.

[127] Cuansing, E. C.; Wang, J.-S. *Phys. Rev. B* **2010**, *81*, 052302.

[128] Hanggi, P.; Talkner, P.; Borkovec, M. *Rev. Mod. Phys.* **1990**, *62*, 0.

[129] Pollak, E.; Schwartz, S. D. *Theoretical methods in condensed phase chemistry*; Springer Netherlands, 2002.

[130] Cui, L.; Miao, R.; Jiang, C.; Meyhofer, E.; Reddy, P. *J. Chem. Phys.* **2017**, *146*, 092201.

[131] Segal, D.; Agarwalla, B. K. *Annu. Rev. Phys. Chem.* **2016**, *67*, 185–209.

[132] Hamed, A.; Elzouka, M.; Ndao, S. *Int. J. Heat Mass Transf.* **2019**, *134*, 359–365.

[133] Kosloff, R.; Levy, A. *Annu. Rev. Phys. Chem.* **2014**, *65*, 365–393.

[134] Segal, D. *Phys. Rev. E* **2018**, *97*, 052145.

[135] Friedman, H. M.; Agarwalla, B. K.; Segal, D. *New J. Phys.* **2018**, *20*, 083026.

[136] Saryal, S.; Friedman, H. M.; Segal, D.; Agarwalla, B. K. *Phys. Rev. E* **2019**, *100*, 042101.

[137] Wu, W.; Zhu, W.-L. *Ann. Phys.* **2020**, 168203.

[138] Hsieh, C.; Liu, J.; Duan, C.; Cao, J. *J. Phys. Chem. C* **2019**, *123*, 17196–17204.

[139] Duan, C.; Hsieh, C.-Y.; Liu, J.; Wu, J.; Cao, J. *J. Phys. Chem. Lett* **2020**, *11*, 4080–4085.

[140] Wang, J.-S. *Phys. Rev. Lett.* **2007**, *99*, 160601.

[141] Barrat, J.-L.; Rodney, D. *J. Stat. Phys.* **2011**, *144*, 679–689.

[142] Zhang, J.; Xu, F.; Hong, Y.; Xiong, Q.; Pan, J. *RSC Adv.* **2015**, *5*, 89415–89426.

[143] Chen, L.; Wang, X.; Kumar, S. *Sci. Rep.* **2015**, *5*, 1–10.

[144] Verdier, M.; Lacroix, D.; Termentzidis, K. *Int. J. Heat Mass Transf.* **2017**, *114*, 550–558.

[145] Xu, K.; Gabourie, A. J.; Hashemi, A.; Fan, Z.; Wei, N.; Farimani, A. B.; Komsa, H.-P.; Krasheninnikov, A. V.; Pop, E.; Ala-Nissila, T. *Phys. Rev. B* **2019**, *99*, 054303.

[146] Zhang, T.; Luo, T. *J. Phys. Chem. B* **2016**, *120*, 803–812.

[147] Jabbari, F.; Rajabpour, A.; Saedodin, S. *Chem. Eng. Sci.* **2017**, *174*, 67–81.

[148] Hong, Y.; Zhang, J.; Zeng, X. C. *Nanoscale* **2018**, *10*, 4301–4310.

[149] Babaei, H.; McGaughey, A. J.; Wilmer, C. E. *Chem. Sci.* **2017**, *8*, 583–589.

[150] Hwang, H.; Rossky, P. J. *J. Chem. Phys* **2004**, *120*, 11380–11385.

[151] Evans, D. J.; Cohen, E. G. D.; Morriss, G. P. *Phys. Rev. Lett.* **1993**, *71*, 2401.

[152] Gallavotti, G.; Cohen, E. G. D. *Phys. Rev. Lett.* **1995**, *74*, 2694.

[153] Jarzynski, C.; Wójcik, D. K. *Phys. Rev. Lett.* **2004**, *92*, 230602.

[154] Hedley, G. J.; Ruseckas, A.; Samuel, I. D. *Chem. Rev.* **2016**, *117*, 796–837.

[155] Xu, R.-P.; Li, Y.-Q.; Tang, J.-X. *J. Mater. Chem. C* **2016**, *4*, 9116–9142.

[156] Ratner, M. *Nat. Nanotechnol.* **2013**, *8*, 378.

[157] Bose, S. *Phys. Rev. Lett.* **2003**, *91*, 207901.

[158] Pouthier, V. *J. Phys. Condens. Matter* **2012**, *24*, 445401.

[159] Pouthier, V. *Phys. Rev. B* **2012**, *85*, 214303.

[160] Pouthier, V. *J. Chem. Phys.* **2012**, *137*, 114702.

[161] Lin, Z.; Rubtsov, I. V. *Proc. Nat. Acad. Sci.* **2012**, *109*, 1413–1418.

[162] Nitzan, A.; Ratner, M. A. *Science* **2003**, *300*, 1384–1389.

[163] Joachim, C.; Ratner, M. A. *Proc. Natl. Acad. Sci. U.S.A* **2005**, *102*, 8801–8808.

[164] Lambert, N.; Chen, Y.-N.; Cheng, Y.-C.; Li, C.-M.; Chen, G.-Y.; Nori, F. *Nat. Phys.* **2013**, *9*, 10.

[165] Rebentrost, P.; Mohseni, M.; Kassal, I.; Lloyd, S.; Aspuru-Guzik, A. *New J. Phys.* **2009**, *11*, 033003.

[166] Plenio, M. B.; Huelga, S. F. *New J. Phys.* **2008**, *10*, 113019.

[167] Mohseni, M.; Rebentrost, P.; Lloyd, S.; Aspuru-Guzik, A. *J. Chem. Phys.* **2008**, *129*, 11B603.

[168] Scholes, G. D.; Fleming, G. R.; Chen, L. X.; Aspuru-Guzik, A.; Buchleitner, A.; Coker, D. F.; Engel, G. S.; Van Grondelle, R.; Ishizaki, A.; Jonas, D. M., et al. *Nature* **2017**, *543*, 647.

[169] Boulais, É.; Sawaya, N. P.; Veneziano, R.; Andreoni, A.; Banal, J. L.; Kondo, T.; Mandal, S.; Lin, S.; Schlau-Cohen, G. S.; Woodbury, N. W., et al. *Nat. Mater.* **2018**, *17*, 159.

[170] Banal, J. L.; Kondo, T.; Veneziano, R.; Bathe, M.; Schlau-Cohen, G. S. *J. Phys. Chem. Lett.* **2017**, *8*, 5827–5833.

[171] Yuen-Zhou, J.; Saikin, S. K.; Yao, N. Y.; Aspuru-Guzik, A. *Nat. Mater.* **2014**, *13*, 1026.

[172] Hasan, M. Z.; Kane, C. L. *Rev. Mod. Phys.* **2010**, *82*, 3045.

[173] Delplace, P.; Ullmo, D.; Montambaux, G. *Phys. Rev. B* **2011**, *84*, 195452.

[174] Freedman, H.; Hanna, G. *Chem. Phys.* **2016**, *477*, 74–87.

[175] Guo, A.-M.; Sun, Q.-F. *Phys. Rev. B* **2017**, *95*, 155411.

[176] Aleksandrov, I. V. *Z. Naturforsch.* **1981**, *36*, 902–908.

[177] Donoso, A.; Martens, C. C. *J. Phys. Chem. A* **1998**, *102*, 4291–4300.

[178] Yang, J.; Yoon, M.-C.; Yoo, H.; Kim, P.; Kim, D. *Chem. Soc. Rev.* **2012**, *41*, 4808–4826.

[179] Nakamura, Y.; Aratani, N.; Osuka, A. *Chem. Soc. Rev.* **2007**, *36*, 831–845.

[180] Nolden, O.; Fleck, N.; Lorenzo, E. R.; Wasielewski, M. R.; Schiemann, O.; Gilch, P.; Richert, S. *Chemistry (Weinheim an der Bergstrasse, Germany)* **2021**, *27*, 2683.

[181] Neubauer, A.; Grell, G.; Friedrich, A.; Bokarev, S. I.; Schwarzbach, P.; Gartner, F.; Surkus, A.-E.; Junge, H.; Beller, M.; Kuhn, O., et al. *J. Phys. Chem. Lett.* **2014**, *5*, 1355–1360.

[182] Cushing, S. K.; Li, J.; Meng, F.; Senty, T. R.; Suri, S.; Zhi, M.; Li, M.; Bristow, A. D.; Wu, N. *J. Am. Chem. Soc.* **2012**, *134*, 15033–15041.

[183] Kodaimati, M. S.; Lian, S.; Schatz, G. C.; Weiss, E. A. *Proc. Natl. Acad. Sci.* **2018**, *115*, 8290–8295.

[184] Mizuno, H.; Nasu, S.; Kitamura, K.; Aoki-Matsumoto, T.; Fujita, A.; Fujita, Y.; Hiromitsu, I. *Thin Solid Films* **2018**, *653*, 136–142.

[185] Atilgan, S.; Ozdemir, T.; Akkaya, E. U. *Org. Lett.* **2010**, *12*, 4792–4795.

[186] Zhang, X.; Wang, W.; Hu, Z.; Wang, G.; Uvdal, K. *Coord. Chem. Rev.* **2015**, *284*, 206–235.

[187] Weil, T.; Reuther, E.; Beer, C.; Müllen, K. *Chem. Eur. J.* **2004**, *10*, 1398–1414.

[188] Fernandez-Alberti, S.; Kleiman, V. D.; Tretiak, S.; Roitberg, A. E. *J. Phys. Chem. Lett.* **2010**, *1*, 2699–2704.

[189] So, M. C.; Wiederrecht, G. P.; Mondloch, J. E.; Hupp, J. T.; Farha, O. K. *Chem. Commun.* **2015**, *51*, 3501–3510.

[190] Sun, Q.; Yin, Z.; Wang, S.; Zhao, C.; Leng, J.; Tian, W.; Jin, S. *J. Phys. Chem. Lett.* **2020**, *11*, 9045–9050.

[191] Goswami, S.; Ma, L.; Martinson, A. B.; Wasielewski, M. R.; Farha, O. K.; Hupp, J. T. *ACS Appl. Mater. Interfaces* **2016**, *8*, 30863–30870.